SURFACE/INTERFACE MODIFICATION AND CHARACTERIZATION OF C-FACE EPITAXIAL GRAPHENE

A Thesis
Presented to
The Academic Faculty

by

Feng Wang

In Partial Fulfillment
of the Requirements for the Degree
Doctor of Philosophy in the
School of Physics

Georgia Institute of Technology
August 2015

Copyright © 2015 by Feng Wang

SURFACE/INTERFACE MODIFICATION AND CHARACTERIZATION OF C-FACE EPITAXIAL GRAPHENE

Approved by:

Professor Edward H. Conrad, Advisor
School of Physics
Georgia Institute of Technology

Professor Walter A. de Heer
School of Physics
Georgia Institute of Technology

Professor Phillip N. First
School of Physics
Georgia Institute of Technology

Professor Zhigang Jiang
School of Physics
Georgia Institute of Technology

Professor Faisal Alamgir
School of Materials Science and Engineering
Georgia Institute of Technology

Date Approved: April 28, 2015

ACKNOWLEDGEMENTS

At the very beginning, I would like to sincerely express my deepest gratitude to my advisor, Dr. Edward Conrad. I could never have imagined a better supervisor than he, who guided me throughout this exciting Ph.D. study. I also want to thank my Ph.D. committee members, Dr. Walter de Heer, Dr. Phillip First, Dr. Zhigang Jiang and Dr. Faisal Alamgir, for their valuable input.

I want to extend my great appreciation to other scientists for their significant help with my thesis work, including Dr. Claire Berger in Georgia Tech, Dr. Leonard Feldman in Rutgers University, Dr. Philip Cohen in University of Minnesota, Dr. Andrea Locatelli, Dr. Tevfik Menteş, and Dr. Alessandro Sala in Elettra Sincrotrone Trieste, Dr. Amina Taleb-Ibrahimi, Dr. Antonio Tejeda, Dr. Irene Palacio-Rodriguez, Dr. Yoshiyuki Ohtsubo, and Arlensui Celis in Synchrotron Soleil, Dr. Yuran Niu and Dr. Alexei Zakharov in MAXlab. I would also like thank my lab members of the whole wonderful graphene group and my collaborators, including Dr. Kristin Shepperd, Dr. Jeremy Hicks, Dr. Yike Hu, Dr. Jan Kunc, Dr. James Palmer, Dr. Ming Ruan, Dr. Rui Dong, Dr. Lei Ma, Dr. Britt Torrence, Dr. Sonam Sherpa, Dr. Gang Liu, Meredith Nevius, Matthew Conrad, Holly Tinkey, Katherine Jinkins, Baiqian Zhang, John Hankinson, Andrei Savu, Jean-Philippe Turmaud, Tien Hoang, Yuntao Li, Hsin-ju Wu, Can Xu, Sara Rothwell, and Ethan Torrey.

I want to thank my friends in Georgia Tech for their support during these years, including Dr. Wenlong Yu, Dr. Wenchao Jiang, Dr. Xunchi Chen, Dr. Si Zhou, Dr. Lede Xian, Feifei Qian, Xiaoyao Ma, Xiaofeng Meng, Shangguo Zhu, Xi Lv, Di Chen, and Yuxuan Jiang. I would also like to thank all my friends in China, United States, and other countries for being in my life.

Last but not least, I am especially grateful to my beloved wife, Dr. Xue Dong, for her steadfast support throughout my doctoral study. I wish to thank my great parents, Xiangchao Wang and Haiqin Xu, for their unconditional love and entirely support. Finally, I wish to thank my ten-month-old son, Fuhao Wang, for the enormous happiness he has brought to my family.

TABLE OF CONTENTS

ACKNOWLEDGEMENTS . . . . **iii**

LIST OF TABLES . . . . **vii**

LIST OF FIGURES . . . . **viii**

LIST OF SYMBOLS OR ABBREVIATIONS . . . . **xiv**

SUMMARY . . . . **xvi**

I INTRODUCTION **1**

1.1 Graphene 1

1.2 Graphene Band Structure 1

1.3 Graphene Growth Method 5

1.3.1 Exfoliated Graphene 5

1.3.2 Epitaxial Graphene on SiC 7

1.3.3 Reduced Graphene Oxide 9

1.3.4 Chemical Vapor Deposition Graphene 10

1.4 Thesis Outline 10

II EPITAXIAL GRAPHENE GROWTH AND CHARACTERIZATION METHOD **13**

2.1 Confinement-controlled Sublimation 13

2.1.1 Sample Preparation 13

2.1.2 Si-face Epitaxial Graphene 15

2.1.3 C-face Epitaxial Graphene 16

2.2 Graphene Characterization Methods 17

2.2.1 Angle-resolved Photoemission Spectroscopy 19

2.2.2 X-ray Photoelectron Spectroscopy 21

2.2.3 Spectroscopic Low-energy Electron Microscopy 21

III INTERACTION BETWEEN SILICON AND GRAPHENE . . . **24**

3.1 Silicon Intercalation Into Graphene-SiC Interface 24

3.1.1 Surface Characterization 26
3.1.2 Graphene Structure Model after Si Intercalation 35
3.2 Graphene-SiC Transformation on C-face Graphene 39
3.2.1 LEED Measurements of SiC Formed on C-face Graphene . . 39
3.2.2 XPS Analysis on SiC Formed on C-face Graphene 43
IV SEMICONDUCTING GRAPHENE GROWN FROM NITROGEN-SEEDED SIC 47
4.1 Semiconducting Graphene with Wide Band-gap Grown from Nitrogen-seeded SiC 47
4.1.1 N-graphene Growth 48
4.1.2 Band-gap Opening 55
4.1.3 Strain Analysis of N-graphene 61
4.2 Pattern Induced Ordering of Semiconducting Graphene Ribbons Grown from Nitrogen-seeded SiC 65
4.2.1 N-graphene Ribbon Structure 66
4.2.2 Electronic Structure of N-graphene Ribbons 74
V CONCLUSION 79
5.1 Summary 79
5.2 Future Outlook 80
APPENDIX A — NITROGEN SITE ASSIGNMENTS 81
APPENDIX B — Q-DEPENDENT BROADENING ANALYSIS . 83
REFERENCES 85

LIST OF TABLES

1 Fit parameters for each cycle. All coverages are in monolayers. 38

LIST OF FIGURES

1 Mother of all graphitic forms. Graphene is a two-dimensional building material for carbon materials of all other dimensionalities. It can be wrapped up into 0D buckyballs, rolled into 1D nanotubes, or stacked into 3D graphite. Taken from reference [5]. 2

2 (a) Graphene honeycomb lattice structure. a_1 and a_2 are unit vectors. Each unit cell is composed of two carbon atoms, red and blue, as shown in the yellow shade. (b)Corresponding brillouin zone. b_1 and b_2 are reciprocal unit vectors. Dirac cones are located at K and K' points. . 3

3 Graphene band structure calculated by Equation 5 with $t = 2.7eV$ and $t' = -0.1eV$. Figure on the right is the zoom in around the Dirac point. 4

4 Exfoliated graphene films. (a) Normal white light photograph of a multilayer graphene flake with thickness $\sim 3nm$ on an oxidized Si wafer. (b) Large graphene crystal prepared on an oxidized Si wafer. (c) AFM image of single layer graphene. (d) A single layer of graphite. Images are taken from references [2, 3, 6]. 6

5 (a) Band structure of doped epitaxial graphene along a line through the K point and perpendicular to the ΓM direction. (b) Band structure of same doped graphene but along the ΓK direction. (c) Scanning tunneling microscopy (STM) image of the epitaxial graphene surface. Inset is an atomically resolved region. Images are taken from references [1, 20]. 8

6 (a) Scanning electron microscopy (SEM) image of a reduced graphene oxide sheet. (b) Shiny and flexible graphene paper formed by controlled restacking of graphene sheets. Images are taken from references [21, 22]. 9

7 (a) Transmission electron microscopy (TEM) image of CVD graphene on Ni. Red dashed lines indicate the step-shaped edges. (b) SEM image of CVD graphene on Cu. (c) and (d) are the graphene growth mechanisms on Ni and Cu, respectively. Images are taken from references [26, 10, 27]. 11

8 (a) Schematic of the graphite crucible used in the CCS method. (b) Photograph of our graphite crucible. (c) Photograph of the entire annealing system, including a quartz tube and an induction heater. . 14

9 AFM images of epitaxial graphene grown on (a) Si-face SiC in UHV, (b) Si-face SiC by the CCS method, (c) C-face SiC by the CCS method. Images are taken from reference [116]. 14

10 (a) Schematic of the graphene-SiC $(6\sqrt{3}\times 6\sqrt{3})R30^{\circ}$ structure. The graphene lattice vector is rotated by 30° from SiC. Open circles are atoms in SiC and filled circles are carbon atoms of graphene. The shaded area shows high symmetry points between the graphene and SiC lattice. (b) LEED pattern of monolayer graphene grown on a 6H-SiC Si-face at 105 eV. (c) Band structure of monolayer Si-face graphene through the K-point and perpendicular to the ΓK direction. Images are taken from references [97, 74]. 15

11 (a) LEED image of three- to four-layer C-face graphene. Graphene spots, SiC spots, and the graphene ring are marked by arrows. (b) 200Å× 200ÅSTM image of a (4,5) supercell for C-face graphene with a relative rotation of 7.34°. (c) Band structure through two K-points of two closely rotated graphene sheets and perpendicular to the ΓK direction. The rotation angle between two graphene sheets is 4.2°. (d) Calculated band structure for isolated graphene (dots), Bernal-stacked graphene (dashed line), and the $R30/R2^{+}$ fault pair (solid line). The inset is the zoom-in at the K-point. Images are taken from references [37, 51]. 18

12 (a) Experimental setup of ARPES. Both polar angle θ and azimuth angle ϕ can be resolved. (b) Schematic of a photo-in electron-out process. Images are taken the ARPES entry in Wikipedia. 19

13 (a) Schematic of the experimental setup for LEEM [129]. (b) Typical LEEM image of a few-layer C-face epitaxial graphene. The starting voltage is 2.8 eV and the field of view (FOV) is 50 μm. (c) Typical XPEEM image of the same sample area. The photon energy is 133 eV and the starting voltage is 26 eV. 22

14 (a) 50μm×50μm LEEM bright field image of 6H C-face sample at -0.05 V. (b) LEEM reflectivity spectrum from the center dark region of (a). 25

15 Si 2p core-level spectra and fits from the two monolayer (ML) graphene region. Spectra are shown for before Si was deposited, after 1.4 ML of Si was deposited, and after Si was annealed at 1020 °C for 10 seconds. The insert shows an expanded view of the spectrum before Si deposition. The photon energy was $h\nu = 133$ eV. Solid lines are the fit peaks. 26

16 Si 2p intensity after 5 ML of Si has deposited (green open circles), after the film has been annealed for 20 sec at 1020°C (blue open circles), and after additional 10sec annealing at 1020 °C (red open circles). The small shift of peak following the second annealing may results from surface work function change. 28

17 (a) $\mu-$LEED image at 96 eV from the bi-layer graphene region in Figure 14, where the Si 2p data is taken in Figure 15 and Figure 16. The principle diffraction rods from two rotated graphene sheets are marked. The inset shows a blowup of the reconstruction pattern. The reciprocal lattice corresponds to a $(\sqrt{57}\times\sqrt{57})_G$R6.59° reconstruction. (b) Simulated LEED pattern from the same $(\sqrt{57}\times\sqrt{57})_G$R6.59° structure commensurated with SiC 30

18 Reconstruction lattice diagram of two graphene sheets (red and blue circles) $(\sqrt{57}\times\sqrt{57})_G$R6.59° and top layer of SiC (black dots) $(6\times6)_{SiC}$. SiC and the red graphene sheet is rotated by 6.59° and 13.17° from the blue graphene sheet respectively 32

19 C 1s spectra before Si intercalation (open circles) and after intercalation (pink dots). 32

20 LEED patterns from; (a) covered graphene region where Si was not deposited, and (b) from center graphene region where 7 ML of Si was deposited and annealed. Note that the weak, but visible, SiC (1×1) pattern in (a) is not visible in (b). Both images were made at 72 eV. 33

21 (a) Clean sample XPEEM image using the SiC-Si 2p peak at a kinetic energy of 25.8 eV with photon energy $h\nu = 133$ eV. The labels indicate the number of graphene layers determined by LEEM reflectivity and XPS spectra. (b) Intensity profile across the vertical bar in (a) from the clean sample (blue open circles) and after ∼7 ML of Si has been deposited and ∼6.3 ML intercalated into the interface (solid red line). 34

22 The Si 2p core-level spectrum after the 6.3 ML Si-intercalated sample was exposed to air at room temperature and subsequently heated to 1200°C in vacuum. 35

23 (a) Model of how an N_i monolayer Si film is redistributed after annealing. Some of the surface Si has formed a carbide bonded to the top graphene layer. (b) Schematic of the surface after 7 ML have been deposited and annealed. Note that the surface Si and surface carbide are treated as part of the total surface coverage. 36

24 LEED images of sample A after Si deposition and annealing at; (a) 1000 °C, (b) 1100 °C, and (c) 1200 °C for 1 minute. All LEED images were taken at 60 eV. 40

25 LEED images of sample B after Si deposition and annealing at; (a) 1100 °C, (b) 1200 °C, (c) 1300 °C, (d) 1400 °C for one minute. SiC $(2\times2)_{SiC}$ and $(3\times3)_{SiC}$ reconstruction patterns are marked in (b) and (c). All LEED images were taken at 60 eV. 42

26 C 1s core-level spectra and fits from (a) sample A before Si deposition and annealing, (b) sample A after Si deposition and annealing at 1200 °C, (c) sample B after Si deposition and annealing at 1400 °C. Open circles are acquired data and solid lines are the fits. Fitted peaks and background have been offset down to make figures more clear. The photon energy is 1486 eV. 44

27 Si 2p core-level spectra and fits from sample B (a) before Si deposition and annealing. (b) sample A after Si deposition and annealing at 1400 °C. Open circles are acquired data and solid lines are the fits. The photon energy is 1486 eV. 45

28 Nitrogen 1s core-level spectra after annealing at different temperatures on (a) C-face from 900 °C to 1565 °C and (b) Si-face from 900 °C to 1200 °C. The photon energy is 1486 eV. 49

29 N 1s and O 1s XPS intensity vs temperature for a SiC C-face nitrogen-seeded surface. 50

30 C 1s spectrum from clean multi-layer C-face graphene and 3-layer N-seeded graphene with $h\nu = 1486$ eV. 50

31 (a)-(c) XPS spectra from SiC C-face before and after growth of a 3-layer graphene film. (a) N 1s, (b) C 1s, and (c) Si 2p ($h\nu = 1486$ eV). A 1.3 eV shift after graphene forms is shown (dashed line). (d) and (e) XPS spectra for an 8-layer graphene film grown from the nitrogen-seeded C-face SiC using photon energies of 500, 600, and 900 eV. The intensities have been normalized to the graphene C 1s peak. (d) N 1s spectra at the same photon energies as (e). Insert shows the 2-component fit to the N 1s peak. The purple, red and blue bars in (d) mark the expected peak positions of pyrrolic, graphitic and pyridinic N-inclusions in graphene, respectively [69, 79]. (e) XPS of the C 1s spectrum for the same photon energies in (d). Insert in (e) shows the SiC portion of the C 1s XPS spectra. (f) The trend in photoelectron intensity versus photoelectron KE energy from an 8-layer graphene sample for the SiC-C 1s, graphene C 1s, and the two N 1s XPS peaks. Absolute intensities have been scaled by arbitrary factors to highlight the energy trend for each peak. 52

32 Schematics showing how graphene layers grow from nitrogen-seeded SiC. (a) Most of the nitrogen, N_S, is bonded to Si atoms (magenta) in carbons sites. The remaining interfacial nitrogen, N_P, is bonded to both the SiC carbon atoms (green) and the graphene, pinning it to the SiC. As the graphene grows and the SiC recedes, nitrogen remains at the SiC interface. (b) and (c) both show that the buckling amplitude in layers farther from the surface is reduced as strain is relieved. . . . 53

33 The ARPES band structure taken with $\hbar\omega = 36$ eV near the K-point of (a) clean 3-layer graphene (T=100K), (b) 3-layer graphene with a 0.2ML nitrogen SiC(000$\bar{1}$) surface (T=300K), and (c) 8-layer graphene from a 0.2ML nitrogen SiC(000$\bar{1}$) surface (T=300K). k_y is perpendicular to the ΓK direction. Note the different energy and momentum scales for (b) and (c) compared to (a). (d) Energy distribution curves through the Dirac point in (a), (b) and (c) show the 0.7 eV gap for 3-layer films that reduces to 0.45 eV for 8-layer films. Note that the apparent energy broadening observed near E_F in the nitrogen samples compared to the clean surface, is entirely resulting from the temperature difference between the two measurements that broadens the 300K Fermi-Dirac function. 55

34 (MDC made at BE=-1.5 eV from the Dirac cone in Figure 33(a). A double Gaussian peak fit (red line) is shown. 56

35 (a) $50 \times 50\text{nm}^2$ STM image of a 3-layer graphene film grown from a 0.2ML nitrogen-seeded C-face SiC (bias voltage, $V_B = 0.1$V). The image shows a pattern of folds. (b) A topographic image of a fold showing the graphene lattice ($V_B = 0.1$V). (c) A 10×10nm view of the graphene folds. (d) A magnified dI/dV images of folded graphene showing that the graphene is continuous over the folds and in the valleys. (e) A dI/dV image of a region in (c). The image shows that the tops of the folds are bright in the dI/dV image indicating a high density of states. 58

36 The Raman spectrum of a 3-layer graphene film with 7 at% nitrogen as determined by XPS and ellipsometry. The SiC background signal has been subtracted. 59

37 Insert shows a radial scan ($q_{\|} = (h{+}\Delta, k{+}\Delta, \ell)_{\mathrm{G}}$) through the graphene $(1, 1, \ell)_{\mathrm{G}}$ rod ($q_z = 2\pi\ell/c_{\mathrm{G}}$ for $\ell = 0.2$) for N-Gr graphene film. The pseudo-Voight fit (black) using a Lorentzian (blue) and Gaussian (red) is shown. The Lorentzian Half widths for the $(01)_{\mathrm{G}}$, $(11)_{\mathrm{G}}$, $(12)_{\mathrm{G}}$, and $(03)_{\mathrm{G}}$ rods are plotted as a function of their radial $q_{\|}$ values. Solid line shows a fit to the data using $\beta_s = \beta_o + Cn^2$ fit to the data where β_o and C are fit parameters. 62

38 (a) Schematic model of the buckled N-Gr caused by nitrogen pinning of the first graphene layer to the SiC. (b) Schematic of the N-Gr ribbons showing highly strained graphene above a nitrogen interface layer on the SiC. Nitrogen is shown in blue. (c) 10 μm FOV LEEM image of a N-Gr ribbon array next to a 2D N-Gr area ($E = 8.6$ eV). The ribbon width is $w = 500$ nm and the pitch is $p = 1$ μm. (d) LEEM reflectivity spectrum from different regions in the 2D area of the sample with different numbers of graphene layers. The curves are shifted vertically for clarity. (e) LEEM reflectivity curves from the N-Gr ribbons and the trenches between ribbons. (f) A histogram of the relative coverage of different graphene thicknesses in the 2D area (solid bars) and in the ribbons (hatched bars). 67

39 (a) C 1s XPS spectra from the N-Gr ribbons and the trenches ($h\nu = 600$ eV). The ribbon width is $w = 400$ nm and the pitch is $p = 1$ μm. (b) 6.5μm FOV XPEEM image using the graphene C 1s peak at a binding energy (BE) of BE=284.5 eV). Blue is from the trenches. (c) N 1s XPS spectra from N-Gr ribbons and etched trench bottoms ($h\nu = 600$ eV). Background has been subtracted for both N 1s spectra. (d) 6.5 μm Fov XPEEM image of the ribbons using the background subtracted N 1s peak for contrast (BE=397.5 eV). Blue is the N 1s intensity in the trenches. 70

40 (a) μ-LEED image from the 2D area showing that the primary graphene spots rotated 30° from the SiC $< 10\bar{1}0 >$ direction. Other rotated domain spots are clearly visible. $E = 40$ eV. (b) DF-LEEM using the graphene $(01)_{\mathrm{G}}$ spot for contrast. $E = 60$ eV. $w = 500$ nm. (c) Constant BE=-1.3 eV cut through the graphene BZ measured by μ-ARPES of a 5-layer N-Gr ribbon area. $\hbar\omega = 36$ eV. The bright Dirac cones are the normal cones from the primary 30° rotated graphene marked in (a). The faint cones are from graphene rotated at other commensurate angles. (d) DF-PEEM (BE=-0.3 eV) of the N-Gr ribbons using the Dirac cone (red circle) in (c) and a 1.5 μm contrast aperture (dashed circle in (b)). 73

41 $E(k)$ slices through the Dirac cone (red circle in Figure 40(c)) on (a) N-Gr ribbons and (c) on a representative area of the 2D N-Gr section. k_y is perpendicular to the $\Gamma - K$ direction. (b) and (d) are corresponding EDCs through the Dirac point of the ribbon and 2D area, respectively. The valance band maximum in (b) is marked by the dashed vertical line. (e) MDC's through the Dirac cones in (a) and (c) at $E - E_F = -1.5$ eV (yellow dashed lines in (a) and (c)). (f) $E(k)$ slices through a Dirac cone from a more ordered area of the 2D N-Gr section. (g) An EDC (red) through the Dirac point in (f) at $E - E_F = -1.5$ eV. A composite EDC (green dashed) is shown that is made from the EDC of the ribbon (b) and the EDC from the disordered 2D region in (d). 75

LIST OF SYMBOLS OR ABBREVIATIONS

2D Two-dimensional

AES Auger electron spectroscopy

AFM Atomic force microscopy

ARPES Angle-resolved photoemission spectroscopy

BOE Buffered oxide etch

BZ Brillouin zone

C-face The $(000\bar{1})$ face of hexagonal SiC

CCS Confinement-controlled sublimation

CVD Chemical vapor deposition

DF Dark field

DOS Density of states

EBL E-beam lithography

EDC Energy distribution curve

ESCA Electron spectroscopy for chemical analysis

FET Field-effect transistor

FOV Field of view

FWHM Full width at half maximum

HBE Higher binding energy

HF Hydrofluoric acid

HOPG Highly-ordered pyrolytic graphite

KE Kinetic energy

LEED Low-energy electron diffraction

LEEM Low energy electron microscopy

MDC Momentum distribution curve

MEM Mirror electron microscopy

ML Monolayer

μ-APRES Micro angle-resolved photoemission spectroscopy

μ-LEED Micro low energy electron diffraction

N-Gr Graphene grown from nitrogen-seeded SiC

PES Photoelectron spectroscopy

RIE Reactive-ion etching

RMS Root mean square

SEM Scanning electron microscopy

Si-face The (0001) face of hexagonal SiC

SiC Silicon carbide

SPELEEM Spectroscopic low energy electron microscopy

STM Scanning tunneling microscopy

SXRD Surface X-ray scattering

TEM Transmission electron microscopy

UHV Ultra-high vacuum

XPEEM X-ray photoemission electron microscopy

XPS X-ray photoelectron spectroscopy

SUMMARY

Graphene has been one of the most interesting and widely investigated materials in the past decade. Because of its high mobility, high current density, inherent strength, high temperature stability and other properties, scientists consider it a promising material candidate for the future all-carbon electronics. However, graphene still exhibits a number of problems such as an unknown interface structure and no sizable band gap. Therefore, the purpose of this thesis is to probe and solve these problems to make graphene suitable for electronics. The work focuses on high-quality C-face epitaxial graphene, which is grown on the $(000\bar{1})$ face (C-face) of hexagonal silicon carbide (SiC) using the confinement-controlled sublimation (CCS) method. C-face epitaxial graphene has much higher mobility compared to Si-face graphene, resulting from its special stacking order and interface structure, the latter of which is not fully understood. Thus, the first part of the work consists of a project, which is to investigate and modify the interface and the surface of C-face graphene by silicon deposition and annealing. Results of this project show that silicon can intercalate into the graphene-SiC interface and form SiC by bonding carbon atoms on the graphene surface. Another crucial problem of graphene is the absence of a band gap, which prevents graphene from becoming an ideal candidate for traditional digital logic devices. Therefore, the second project of this work is devoted to introducing a wide band gap into the graphene electronic structure by growing from a nitrogen-seeded SiC. After successful opening of a band gap, a pre-patterning method is applied to improve graphene thickness variations, orientational epitaxy, and the gapped electronic structure.

CHAPTER I

INTRODUCTION

1.1 Graphene

Carbon is one of the most important elements on our planet. With its unique diversity of organic compounds and the ability to form polymers, carbon is the chemical basis of all known life forms and organic chemistry. Because of its valency, carbon is able to form numerous allotropes. The most common carbon allotrope in our daily lives is graphite since it is the most stable form of carbon under standard conditions. The structural basis for graphite is a single layer hexagonal carbon structure called graphene. Besides graphite, graphene is also the structural basis for other carbon allotropes. For example, graphene can be wrapped up into zero-dimensional buckyballs and rolled into one-dimensional nanotubes as Figure 1 shows.

Since the initial experimental work was done by W. A. de Heer and later A. K. Geim [1, 2], graphene rapidly became one of the most studied materials in the last decade. As a single sheet of an sp^2-bonded honeycomb carbon lattice, graphene is the ideal two-dimensional (2D) material with exceptionally high crystal and electronic quality [4, 5].

In this chapter, basic knowledge of graphene including band structure and growth method will be introduced in detail.

1.2 Graphene Band Structure

One of the most superior properties of graphene is its linear electronic band structure at the corners of the hexagonal brillouin zone. Both electrons and holes act like massless Dirac fermions. The graphene band structure was calculated back in 1947

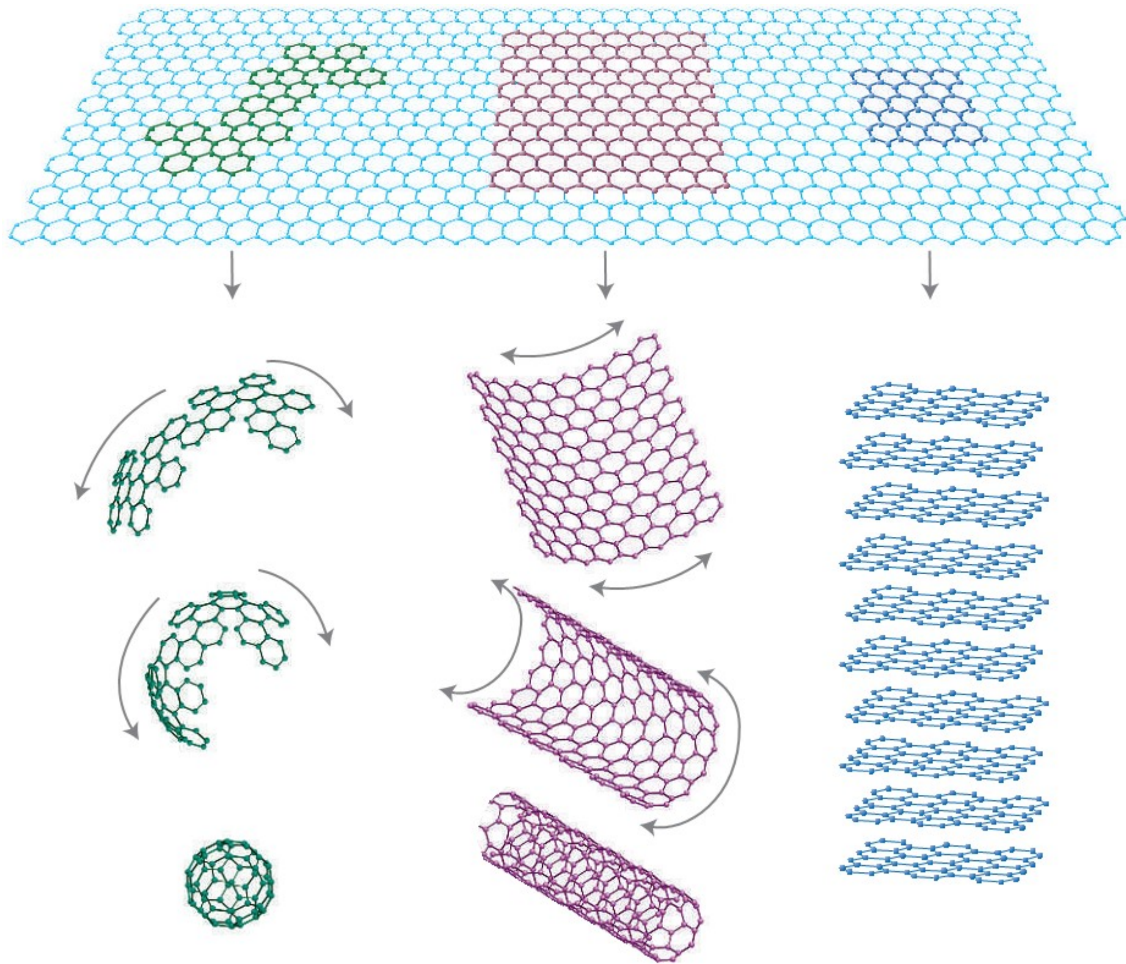

Figure 1: Mother of all graphitic forms. Graphene is a two-dimensional building material for carbon materials of all other dimensionalities. It can be wrapped up into 0D buckyballs, rolled into 1D nanotubes, or stacked into 3D graphite. Taken from reference [5].

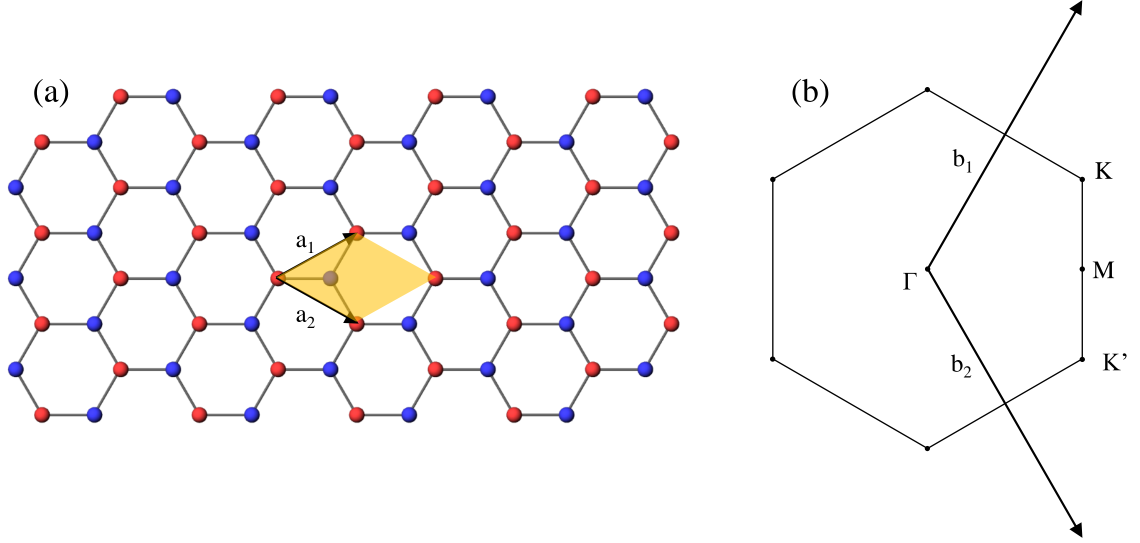

Figure 2: (a) Graphene honeycomb lattice structure. a_1 and a_2 are unit vectors. Each unit cell is composed of two carbon atoms, red and blue, as shown in the yellow shade. (b)Corresponding brillouin zone. b_1 and b_2 are reciprocal unit vectors. Dirac cones are located at K and K' points.

by P. R. Wallace using a tight-bonding model [7]. However, at that time, studies of graphene served as a basis for graphite research since graphite was an important material for nuclear reactors and there was no way to produce a single layer of graphite. In this section, we will start with the calculation of the graphene band structure.

Graphene is a two-dimensional honeycomb structure as Figure 2 shows. The unit cell is composed of two carbon atoms, A and B, as red and blue atoms. The lattice vectors a_1 and a_2 can be written as

$$\boldsymbol{a}_1 = \frac{3a}{2}\boldsymbol{i} + \frac{\sqrt{3}a}{2}\boldsymbol{j}, \qquad \boldsymbol{a}_2 = \frac{3a}{2}\boldsymbol{i} - \frac{\sqrt{3}a}{2}\boldsymbol{j}, \tag{1}$$

where a is the carbon-carbon bond length, which is 1.42Å. The corresponding reciprocal lattice vectors b_1 and b_2 are

$$\boldsymbol{b}_1 = \frac{2\pi}{3a}\boldsymbol{i} + \frac{2\sqrt{3}\pi}{3a}\boldsymbol{j}, \qquad \boldsymbol{b}_2 = \frac{2\pi}{3a}\boldsymbol{i} - \frac{2\sqrt{3}\pi}{3a}\boldsymbol{j}. \tag{2}$$

The corners of the brillouin zone, K and K', are of particular interest because of

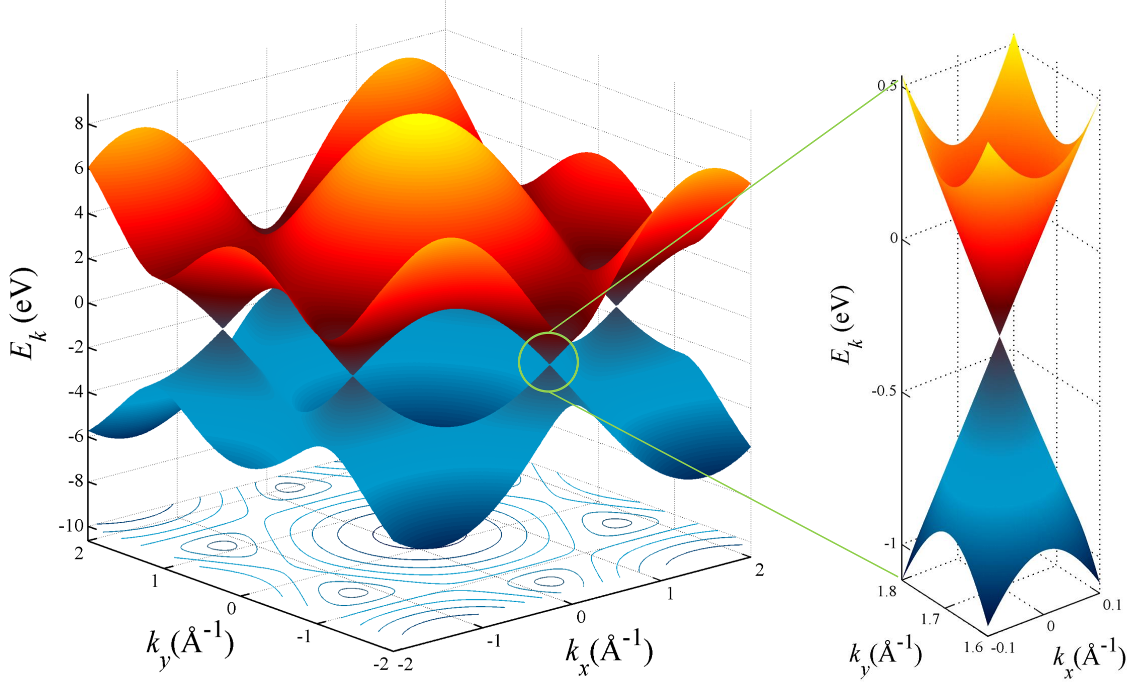

Figure 3: Graphene band structure calculated by Equation 5 with $t = 2.7eV$ and $t' = -0.1eV$. Figure on the right is the zoom in around the Dirac point.

the linear relation in the band structure, as mentioned earlier. The positions of these two points are given by

$$\boldsymbol{K} = \frac{2\pi}{3a}\boldsymbol{i} + \frac{2\pi}{3\sqrt{3}a}\boldsymbol{j}, \qquad \boldsymbol{K'} = \frac{2\pi}{3a}\boldsymbol{i} - \frac{2\pi}{3\sqrt{3}a}\boldsymbol{j}. \tag{3}$$

Assuming that electrons can hop to only the nearest and the next nearest neighbor atoms, an analytical energy band structure can be derived as

$$E_{\pm}(\mathbf{k}) = \pm t\sqrt{3 + f(\mathbf{k})} - t' f(\mathbf{k}), \tag{4}$$

$$f(\mathbf{k}) = 2\cos(\sqrt{3}k_y a) + 4\cos(\frac{\sqrt{3}}{2}k_y a)\cos(\frac{3}{2}k_x a), \tag{5}$$

where $t(\approx 2.7eV)$ is the nearest neighbor hopping energy, t' is the next nearest neighbor hopping energy, the plus sign is for the conduction band and the minus sign is for the valence band. From Equation 5, it is clear that if $t' = 0$, the spectrum will be symmetric around zero energy. Since we are primarily interested in the corners of

the brillouin zone, the dispersion can be expanded around the K point, including t' up to the second order in q/K by assuming that $\mathbf{k} = \mathbf{K} + \mathbf{q}$, while $|\mathbf{q}| \ll |\mathbf{K}|$. The energy near the K point becomes

$$E_{\pm}(\mathbf{q}) \simeq 3t' \pm v_F|\mathbf{q}| - (\frac{9t'a^2}{4} \pm \frac{3ta^2}{9} sin(3\theta_q))|\mathbf{q}|^2, \quad (6)$$

where $\mathbf{q}$ is the momentum with respect to the $\mathbf{K}$ point, and v_F is the Fermi velocity, given by $v_F = 3ta/2$. The Fermi velocity is about $10^6 m/s$. $\theta_q = arctan(\frac{q_x}{q_y})$ is the angle in the momentum space. This equation implies that t' only changes the energy position of the Dirac point, but it does not change the linear dispersion relationship up to the second order. It also indicates the threefold symmetry, which is the so-called trigonal warping [8].

1.3 Graphene Growth Method

During the past decade of graphene research, researchers have developed many growth techniques to produce graphene films. Currently they are fabricated using four main techniques: (1) mechanical exfoliated graphene by using scotch tape to repeatedly peel off small mesas of highly ordered pyrolytic graphite (HOPG) [2], (2) epitaxial graphene by annealing SiC to high temperatures such as $\sim 1600\,^{\circ}\mathrm{C}$ [1], (3) reduced graphene oxide by various reduction methods applied to graphene oxide, which is produced by the Hummers and Offeman method [9], and chemical vapor deposition (CVD) graphene by depositing hydrocarbons on metal substrates such as copper [10], nickel [11, 26], and ruthenium [12]. However, none of these method are flawless. In this section, a brief introduction of each method will be provided.

1.3.1 Exfoliated Graphene

The simplest way to produce graphene is called mechanical exfoliation, also referred as the "scotch tape method," developed in 2004. It quickly became popular because of its acceptable quality, low cost, and excellent ambipolar electric field effect. The

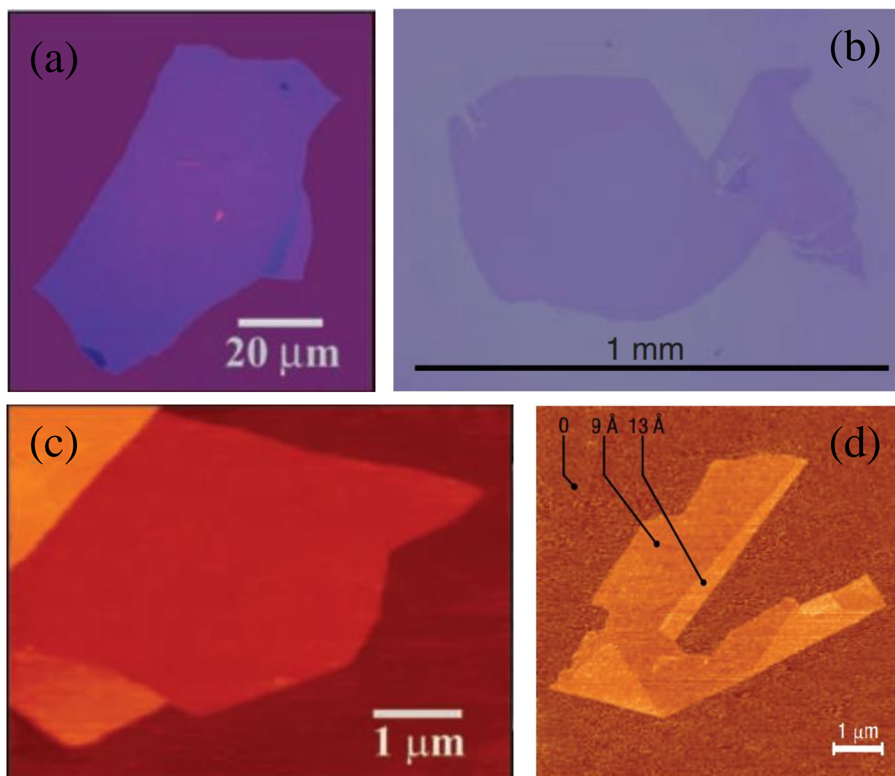

Figure 4: Exfoliated graphene films. (a) Normal white light photograph of a multilayer graphene flake with thickness $\sim 3nm$ on an oxidized Si wafer. (b) Large graphene crystal prepared on an oxidized Si wafer. (c) AFM image of single layer graphene. (d) A single layer of graphite. Images are taken from references [2, 3, 6].

exfoliation method also led the Nobel Prize in Physics for A. K. Geim and K. S. Novoselov for their "groundbreaking experiments regarding the two-dimensional material graphene." One success point of this method is that graphene becomes visible when it is placed onto silicon dioxide. The interference contrast makes thin graphene film stand out under an optical microscope as shown in Figure 4.

The starting material is the platelets of HOPG with 1 mm thickness. Various size mesas are prepared by dry etching in oxygen plasma. Then the surface is attached to a photoresist. After the sample is baked, the scotch tape is used to repeatedly peel flakes of graphite off the mesas, and dipped into acetone. Then a silicon wafer with 300nm silicon dioxide is applied to capture these thin flakes. Most of the thicker flakes can be removed afterward by ultrasound cleaning in propanol, leaving thin flakes that

can be detected by the optical microscope. A similar method can be also applied to other two-dimensional materials such as boron nitride [13] and molybdenum disulfide [14].

Exfoliated graphene has several disadvantages. First, the normal size of exfoliated graphene is usually around a few microns. Although as shown in Figure 4, exfoliated graphene can be as large as millimeter size, it is quite difficult to produce and the quality of it is in doubt. Second, it is time-consuming to peal off and look for an ideal single layer graphene flake. Finally, both the physical and electronic structures of exfoliated graphene are worse than those of epitaxial graphene [15, 16]. The surface roughness of exfoliated graphene is 10 times as high as that of epitaxial graphene when measured under atomic force microscope (AFM), and the Dirac cone can be barely seen under angle-resolved photoemission spectroscopy (ARPES). All these drawbacks make exfoliated graphene less promising for future electronics development.

1.3.2 Epitaxial Graphene on SiC

Even earlier than the discovery of exfoliated graphene, scientists started to recognize that ultrathin graphite was able to grow out of silicon carbide crystal and patternable graphene nano-electronics could also be achieved [1, 18]. The graphitization of SiC was first shown by Van Bommel et al. in 1975 [17]. Low-energy electron diffraction (LEED) and Auger electron spectroscopy (AES) were used to characterize the surface state of the thin graphite layer on both the carbon terminated face (C-face) and the silicon terminated face (Si-face). At high temperatures, silicon sublimated from the surface, leaving excess carbon atoms that transformed into a graphene structure. This early study provided an initial idea about the crystallography of graphene grown on both faces of SiC. After continuous research was carried out on the epitaxial graphene, more and more scientists realized that epitaxial graphene on SiC could have more a promising future than exfoliated graphene because of its extremely flat surface [1]

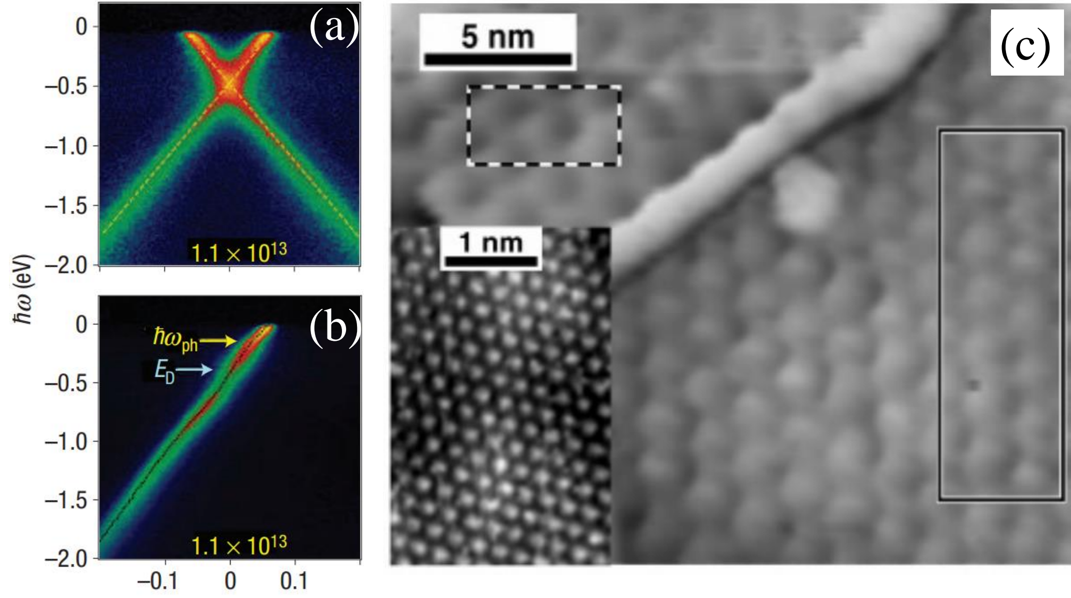

Figure 5: (a) Band structure of doped epitaxial graphene along a line through the K point and perpendicular to the ΓM direction. (b) Band structure of same doped graphene but along the ΓK direction. (c) Scanning tunneling microscopy (STM) image of the epitaxial graphene surface. Inset is an atomically resolved region. Images are taken from references [1, 20].

and its much more ordered electronic structure as shown in Figure 6 [20].

During the growth of epitaxial graphene, SiC pieces are usually heated in the ultra-high vacuum (UHV) environment. To produce even better epitaxial graphene films, a group led by W. A. de Heer developed a more sophisticated method called confinement-controlled sublimation (CCS) [116]. Epitaxial graphene grown by the CCS method has exceptional high mobility [29], the quantum Hall effect [30], the Landau level [55], the fractional Landau level [31], self-assembly ribbons [32], decouple layers in multi-layer C-face graphene [51], and ballistic transport [75]. Detailed information will be introduced in the next chapter. Despite the high cost of the SiC wafer (rapidly decreased since 2004), epitaxial graphene has been widely considered to be the best quality graphene.

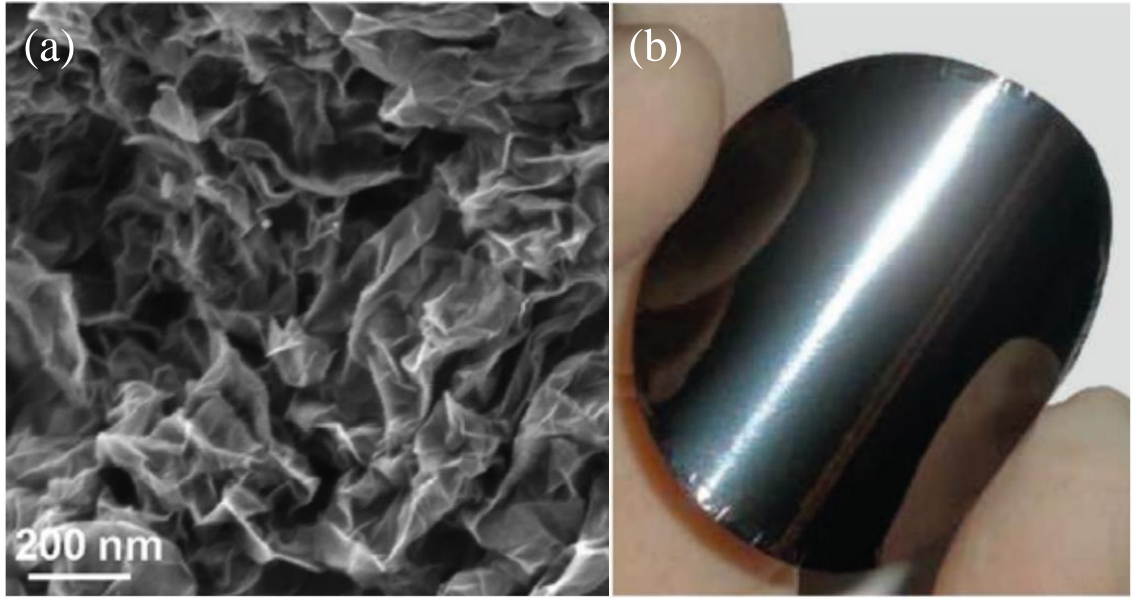

Figure 6: (a) Scanning electron microscopy (SEM) image of a reduced graphene oxide sheet. (b) Shiny and flexible graphene paper formed by controlled restacking of graphene sheets. Images are taken from references [21, 22].

1.3.3 Reduced Graphene Oxide

Another chemical way to produce the graphene sheet is the reduction of graphene oxide. The strength of this method is its ability to produce large amount of graphene powder and large graphene monolayers, which are highly processable and ready for fabrication [9].

Graphite oxide is first prepared by the Hummers method [23]. Original graphite is treated with a water-free mixture of concentrated sulfuric acid, sodium nitrate, and potassium permanganate. To isolate graphene oxide from graphite oxide, the most common method is mild sonication or stirring in water [9]. Then the left graphene oxide can be reduced in many ways, such as chemical reduction [21], thermal reduction [24], and multi-step reduction [25]. All these different reduction methods have the same purpose, which is to eliminate functional groups and heal the structural defects.

All in all, the reduction of the graphene oxide method proposes an alternative attractive way of producing large quantity of graphene. However, the quality of this

type of graphene remains questionable with a large number of defects. Extensive research is required for the further incorporation of reduced graphene oxide into applications.

1.3.4 Chemical Vapor Deposition Graphene

Because of both compatibility and scalability, chemical vapor deposition has emerged as another popular method to produce graphene since it was first reported on nickel in 2008 [26] and copper in 2009 [10] (see Figure 7). This method is low cost, and it can be applied to many commercial CVD systems. During the process, gas species such as methane or ethylene are injected into the reactor and pass through the substrate. Then the hydrocarbon decomposes on the surface of the metal substrate to carbon radicals, which can form graphene.

The quality of CVD graphene can be affected greatly by the substrate as well as the subsequent transfer method. For example, the Cu substrate turns out to be a better choice than Ni to grow monolayer graphene because of different growth mechanism. Graphene grows on Ni through carbon segregation and precipitation; however, on Cu, growth is through a surface reaction, as shown in Figures 7(c) and (d). The quality-limiting step is the transfer method. Resulting from the discontinuities in the transferred graphene sheet, CVD graphene has low conductivity [28].

1.4 Thesis Outline

In this first chapter, the background information of graphene has been introduced briefly. In the second chapter, more details of the epitaxial graphene growth and characterization method including the confinement-controlled sublimation method and various surface characterization instruments will be discussed. The topic of Chapter III is my first project, which is composed of two parts. The first is the intercalation of Si into the graphene-SiC interface, and the second is surface SiC formation on top of graphene. The purpose of the project is to investigate and control

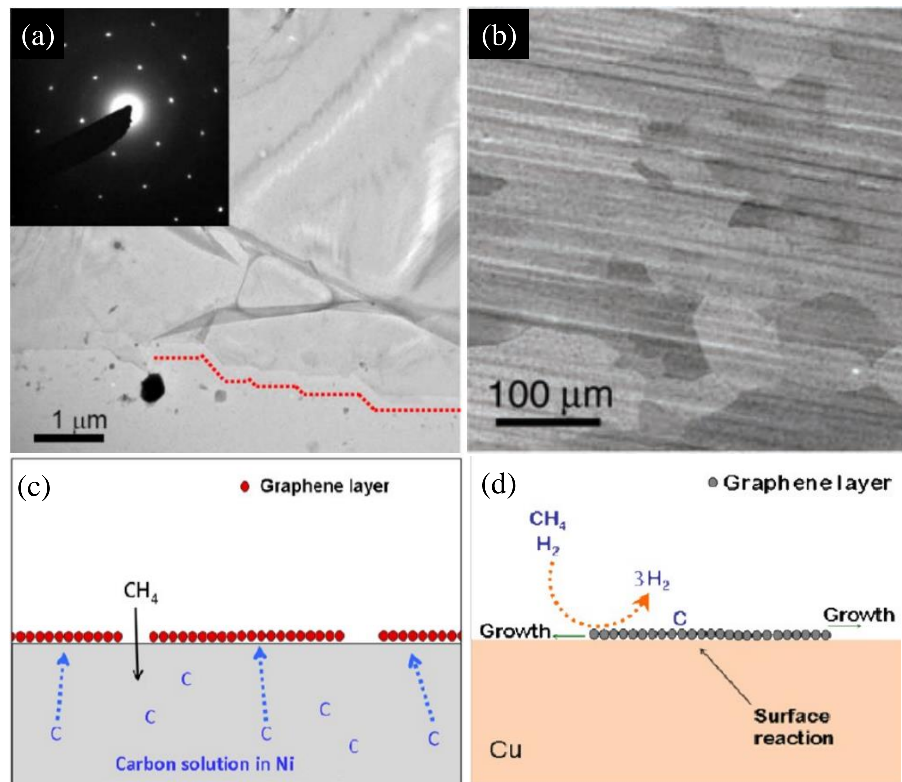

Figure 7: (a) Transmission electron microscopy (TEM) image of CVD graphene on Ni. Red dashed lines indicate the step-shaped edges. (b) SEM image of CVD graphene on Cu. (c) and (d) are the graphene growth mechanisms on Ni and Cu, respectively. Images are taken from references [26, 10, 27].

the interface and the surface of graphene by Si deposition and annealing. In Chapter IV, we focuse on the semiconducting form of graphene grown from nitrogen-seeded SiC and the improvement of this type of graphene by a pre-patterning method. The idea is to solve the inherent problem of graphene, which is the absence of a sizable band gap.

CHAPTER II

EPITAXIAL GRAPHENE GROWTH AND CHARACTERIZATION METHOD

2.1 Confinement-controlled Sublimation

2.1.1 Sample Preparation

As mentioned in the previous chapter, researchers anneal SiC in the UHV environment to grow graphene. However, the quality of such graphene is relatively low because of the high sublimation rate of Si at lower temperatures. This section reviews an improved annealing method called confinement-controlled sublimation (CCS), developed by the Georgia Tech team led by W. A. de Heer [116]. The basic idea is to trap Si vapor inside a semi-closed graphite crucible that contains the SiC piece, causing the high sublimation rate of Si to decrease. The reduced sublimation rate leads a higher growth temperature and thus better quality of graphene forming on both C-face and Si-face SiC.

All SiC wafers used in this thesis are single-crystal 4H or 6H N-type SiC wafers from Cree, Inc. The wafer is cut on-axis with a miscut angle of less than 0.25°. Both faces are polished while only Si-face is chemical-mechanical planarized and epi-ready. SiC wafers were cut by the dicing saw in the cleanroom. Then each piece was cleaned by sonication in acetone and isopropyl alcohol for 30 minutes separately. After that, C-face SiC samples were etched by hydrogen at 1400 °C for half an hour in order to grow graphene because C-face was not epi-ready. Hydrogen etching was used to make an atomic-flat surface of SiC [39].

Figure 8 shows a schematic and a photograph of the graphite crucible used to grow all the epitaxial graphene samples. The pressure in the tube was kept in the

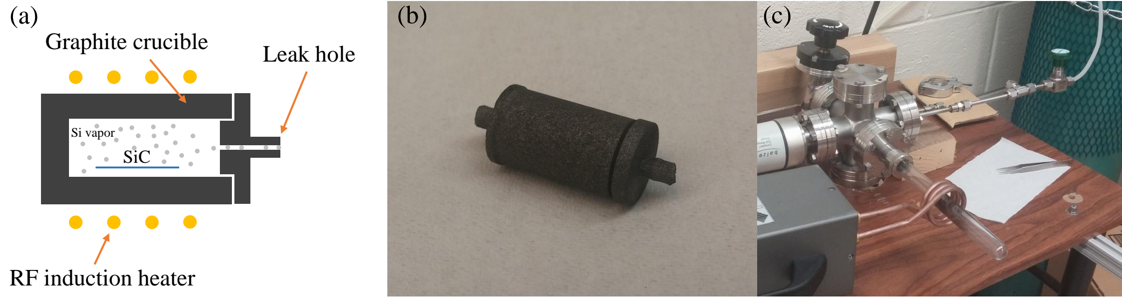

Figure 8: (a) Schematic of the graphite crucible used in the CCS method. (b) Photograph of our graphite crucible. (c) Photograph of the entire annealing system, including a quartz tube and an induction heater.

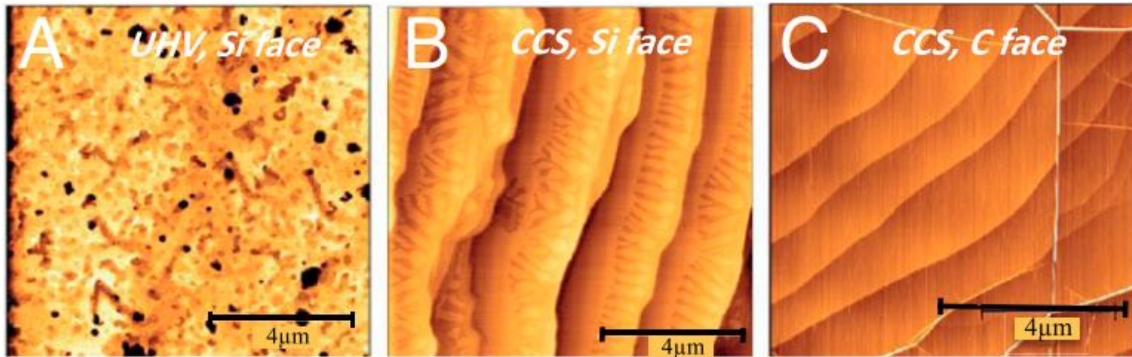

Figure 9: AFM images of epitaxial graphene grown on (a) Si-face SiC in UHV, (b) Si-face SiC by the CCS method, (c) C-face SiC by the CCS method. Images are taken from reference [116].

10^{-6} Torr range. Si vapor (gray dots) mostly remains inside the crucible, which has a $1mm$ diameter hole for the leak. However, in Chapter IV, a different cap with a $2mm$ diameter leak hole was used to grow N-graphene (N-Gr) at lower temperatures.

The first transport measurement on the epitaxial graphene was on the UHV-grown sample. However, this type of graphene is defective and has low mobility [1]. A comparison of UHV- and CCS-grown epitaxial graphene is shown in Figure 9. Graphene samples grown by the CCS method have a much more uniform and ordered surface structure. The graphite-enclosed crucible greatly limits the escape of Si vapor and thus maintains high Si vapor pressure around the sample. Thus, near thermodynamic equilibrium can be reached at higher temperatures.

Another property of epitaxial graphene is that the graphene grows on both polar

faces of hexagonal SiC. However, graphene on different faces has noticeably different structures both physically and electronically. The following two sections discusses these two types of graphene.

2.1.2 Si-face Epitaxial Graphene

Different from multi-layer graphene formed on the C-face of SiC, Si-face graphene is usually difficult to grow after the initial few layers formed. In another words,

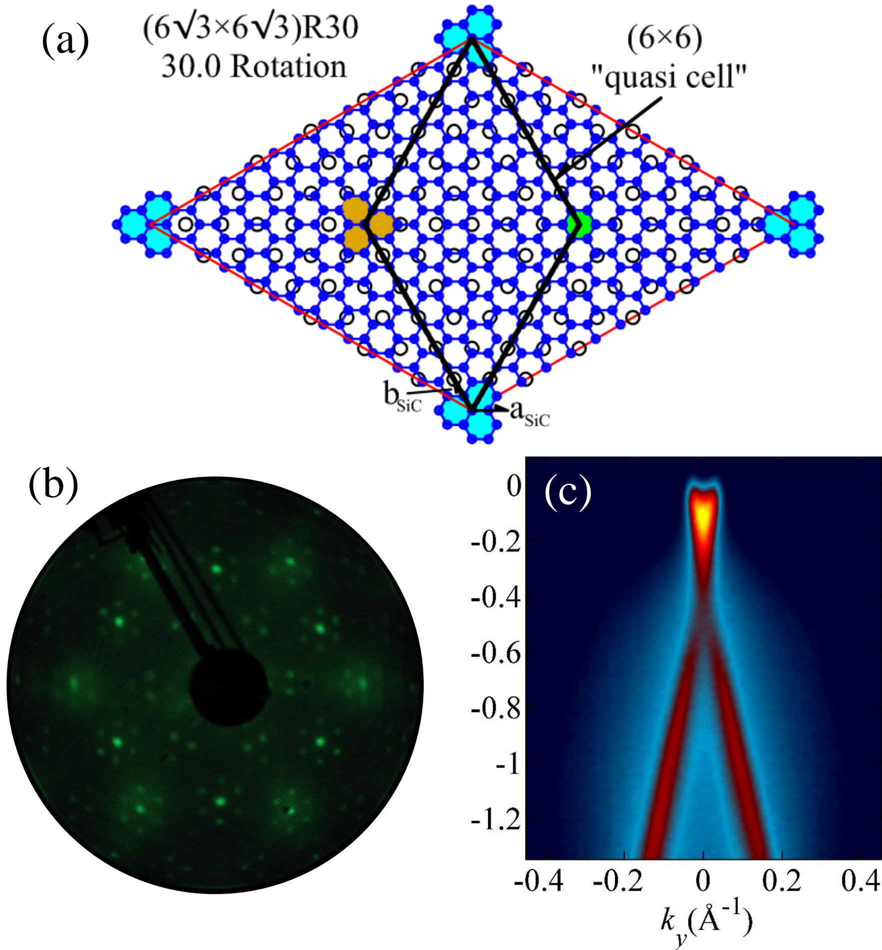

Figure 10: (a) Schematic of the graphene-SiC $(6\sqrt{3}\times 6\sqrt{3})R30°$ structure. The graphene lattice vector is rotated by 30° from SiC. Open circles are atoms in SiC and filled circles are carbon atoms of graphene. The shaded area shows high symmetry points between the graphene and SiC lattice. (b) LEED pattern of monolayer graphene grown on a 6H-SiC Si-face at 105 eV. (c) Band structure of monolayer Si-face graphene through the K-point and perpendicular to the ΓK direction. Images are taken from references [97, 74].

the thickness of graphene on the Si-face is easier to control. The surface of Si-face graphene exhibits the famous $(6\sqrt{3}\times6\sqrt{3})R30^{\circ}$ reconstruction pattern (see Figure 10(b)) first observed by Van Bommel [17]. This pattern is formed by surface reconstruction between the first graphene layer and the SiC surface, as shown in Figure 10(a). However, little is known about this reconstruction. It is presumed that part of the graphene layer is covalently bonded to the SiC surface [34]. Note that this bond is not stable, so it can be broken by hydrogen intercalation at low temperatures ($<600\,^{\circ}$C) [61].

As a result of the surface reconstruction, the first graphene layer on Si-face SiC is not electronically graphene even though it has a hexagonal graphene structure, that is a "buffer layer." As it does not have a Dirac cone, it could potentially be a semiconducting form of graphene [35]. The band structure shown in Figure 10(c) is taken from a monolayer Si-face epitaxial graphene. The monolayer is another graphene layer that has formed above the buffer layer. This layer of graphene, although still having a $6\sqrt{3}$ structure, exhibits the characteristic Dirac cone. It also shows 0.5 eV n-type doping of the band, which is a result of the depletion of the dopant carriers in the substrate [33]. When multi-layer graphene forms on Si-face SiC, the band structure dramatically changes. Because of the Bernal stacking of Si-face epitaxial graphene, the linear Dirac cone band structure changes to parabolic bands and eventually evolves to the graphite band structure as the number of layers increases [36].

2.1.3 C-face Epitaxial Graphene

For C-face epitaxial graphene, Van Bommel also pointed out its rotational disorder [17]. Thus, little attention was devoted to C-face graphene in the initial stage of graphene research. However, further investigation indicated that such a special rotational stacking order happened to be the key feature of C-face graphene that allowed

it to have a nearly ideal Dirac cone [51]. Unlike the Bernal stacking on the Si-face mentioned before, the rotation angle between two graphene sheets on C-face can be any commensurate angle [37]. Figure 11(a) shows a typical LEED pattern of the thin C-face epitaxial graphene using the CCS method. In addition to graphene and SiC spots, a diffused ring-shape intensity at the graphene radius, referred to as a “graphene ring,” is observed. This graphene ring is from the commensurately rotated graphene sheets. One possible rotated graphene atomic structure is shown later in Figure 18 in Chapter III. A scanning tunneling microscopy (STM) image of the supercell formed by two rotated graphene sheets is also shown in Figure 11(b). A detailed discussion of the μ-LEED image of such a supercell is given in the next chapter (Figure 17). Although the structural model of C-face graphene remains unclear, in the next chapter (Figure 25), we claim that the top layer of graphene is oriented in a single direction and that only layers below the top layer are polycrystalline and rotated differently.

Figure 11(c) is the ARPES measurement of multi-layer C-face graphene. The Dirac cones do not evolve as Si-face multi-layer graphene does. Instead, the linear shapes of Dirac cones persist in each layer because of the special stacking order of C-face graphene, which decouples adjacent graphene layers. Therefore, each Dirac dispersion at the K-point is preserved even for the multi-layer graphene [51]. Confirming this conclusion, Figure 11(d) shows a first-principle calculation of the band structure resulting from various stacking orders. In summary, because of the stacking order, multi-layer C-face epitaxial graphene grown by the CCS method still holds the single-layer graphene band structure. It is not thin graphite.

2.2 Graphene Characterization Methods

After graphene growth by the CCS method, the next step is to characterize the sample. Many surface characterization instruments can be used on graphene such as

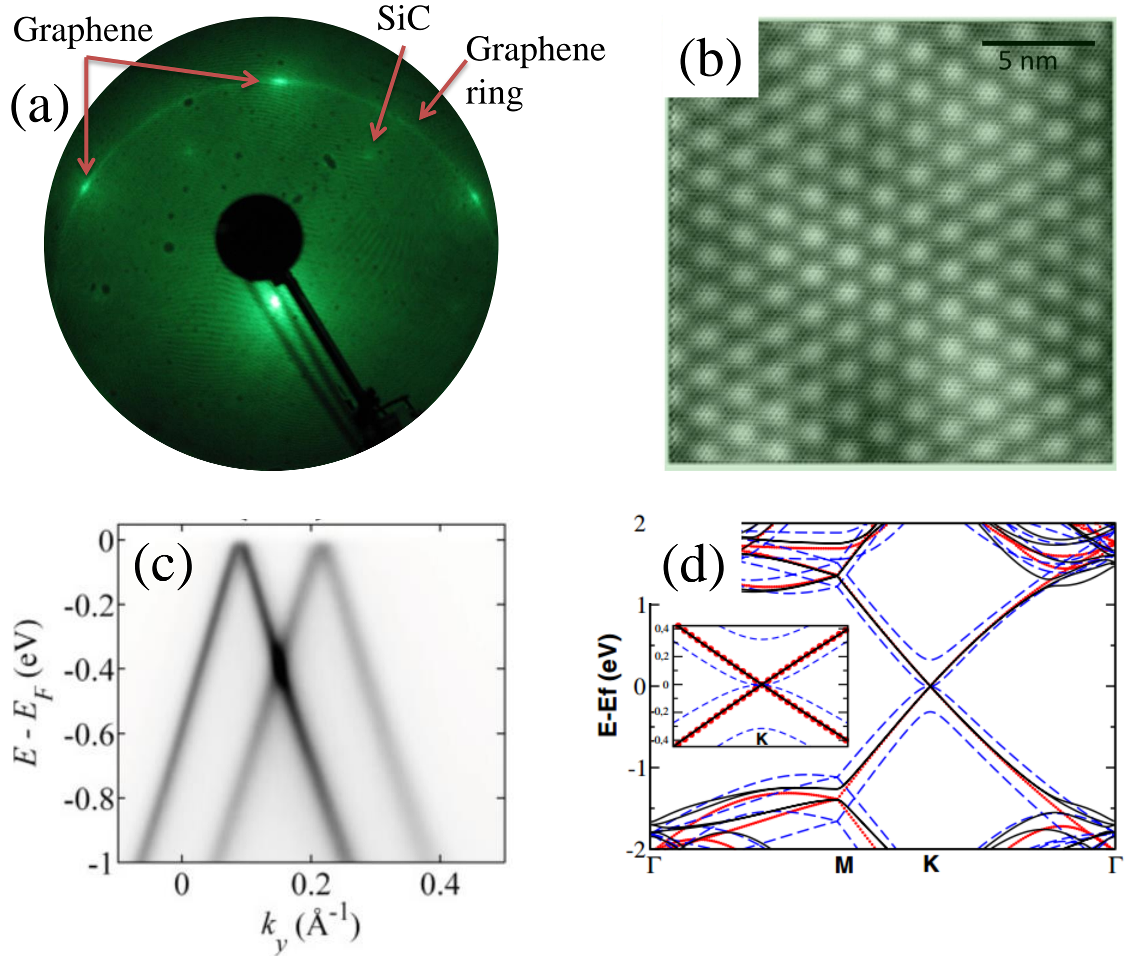

Figure 11: (a) LEED image of three- to four-layer C-face graphene. Graphene spots, SiC spots, and the graphene ring are marked by arrows. (b) 200Å× 200ÅSTM image of a (4,5) supercell for C-face graphene with a relative rotation of 7.34°. (c) Band structure through two K-points of two closely rotated graphene sheets and perpendicular to the ΓK direction. The rotation angle between two graphene sheets is 4.2°. (d) Calculated band structure for isolated graphene (dots), Bernal-stacked graphene (dashed line), and the $R30/R2^{+}$ fault pair (solid line). The inset is the zoom-in at the K-point. Images are taken from references [37, 51].

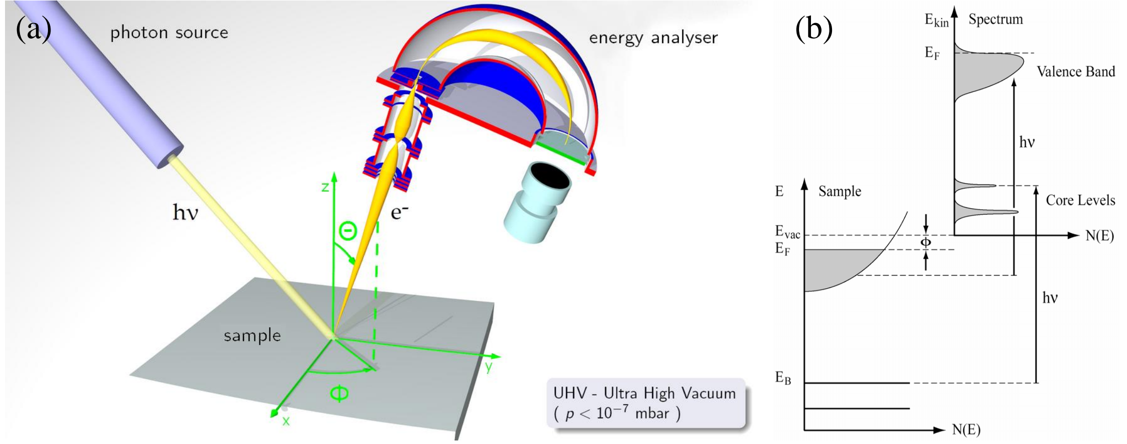

Figure 12: (a) Experimental setup of ARPES. Both polar angle θ and azimuth angle ϕ can be resolved. (b) Schematic of a photo-in electron-out process. Images are taken the ARPES entry in Wikipedia.

AFM, Raman, SEM, and STM. This section introduces several main characterization methods used in this thesis.

2.2.1 Angle-resolved Photoemission Spectroscopy

Since the Dirac cone is one of the most important features of graphene, scientists have used various tools to directly measure the band structure of graphene. Angle-resolved photoemission spectroscopy, "ARPES," is the best tool for imaging the Dirac cone, as shown in previous section. Because ARPES is a photoemission process, it belongs to photoelectron spectroscopy (PES). PES is a general term that describes all techniques based on the photoelectron effect. It was first observed by H. Hertz in 1886. The basic idea of PES is simple; Photons are incident on the sample and photoejected electrons are collected and analyzed by the detector, which provides the energy and intensity information. In the case of ARPES, the energy analyzer detector is also sensitive to the angular distribution of electrons. Thus, both energy and the angle can be resolved at the same time in ARPES. From this data, the angle-energy space images can be calculated into momentum-energy space to obtain the band structure.

Figure 12(a) shows a normal experimental setup for the ARPES measurement. A

general photoemission process diagram is shown in (b). As a result of the conservation of energy, we have

$$E_f - E_B = h\nu - E_{kin} - \Phi_d, \tag{7}$$

where E_f is the Fermi energy, E_B is the binding energy of the photoelectron, $h\nu$ is the photon energy, E_{kin} is the kinetic energy (KE) of the electron measured by the analyzer, and Φ_d is the work function of the detector instead of the sample. This equation is used to transform the measured electron kinetic energy to the binding energy inside the material. Since only the parallel momentum of the photoelectron is conserved, the following equation is applied to calculate the momentum;

$$k_{\parallel} = \frac{\sqrt{2mE_{kin}}}{\hbar}\sin\theta \approx 0.512\sqrt{E_{kin}}\sin\theta(\text{Å}^{-1}), \tag{8}$$

where $k_{\parallel}$ is the momentum of the electron parallel to the sample surface, m is the electron mass, $\hbar$ is the reduced Planck constant, and θ is the polar angle shown in Figure 12(a). Then it is straightforward to calculate the k_x and k_y separately as

$$k_x \approx 0.512\sqrt{E_{kin}}\sin\theta\cos\phi(\text{Å}^{-1}), \tag{9}$$

$$k_y \approx 0.512\sqrt{E_{kin}}\sin\theta\sin\phi(\text{Å}^{-1}), \tag{10}$$

where ϕ is the azimuth angle in Figure 12(a). Be aware that not all of the ARPES setups follow this angle convention. Different equations are required for different angle definitions.

All ARPES images used in this thesis were taken in the Cassiopée beamline at Synchrotron SOLEIL in Gif-sur-Yvette, France. The high resolution Cassiopée beamline has a total measured instrument resolution of $\Delta E < 12$meV using a Scienta R4000 detector with a $\pm 15°$ acceptance angle at $\hbar\omega = 36$ eV.

2.2.2 X-ray Photoelectron Spectroscopy

Other than ARPES, another PES instrument widely used in contemporary research is X-ray photoelectron spectroscopy (XPS), also known as electron spectroscopy for chemical analysis (ESCA). Similar to ARPES, Equation 7 also applies to XPS. The difference between XPS and ARPES is that XPS uses high energy photons to excite core-level electrons while ARPES uses low-energy photons to excite valence band electrons just below the Fermi level.

The most common X-ray source equipped in lab-type XPS is the aluminium K-alpha source, which has the fixed photon energy of 1486 eV. For synchrotron-type of XPS, photon energy can be tuned within a large range. Different photon energies result in different elastic mean free paths. The following two chapters will provide detailed information about how depth information of a particular chemical species can be derived from XPS spectra with varying photon energies. The XPS spectra in this thesis were taken either from Thermo K-alpha XPS in the cleanroom of Georgia Tech or from various synchrotron beamline stations.

2.2.3 Spectroscopic Low-energy Electron Microscopy

To fully understand the surface structure, we require not only spectroscopy methods but also microscopy tools. Spectroscopic low-energy electron microscopy (SPELEEM) is one of the most powerful instrument for imaging the graphene surface as well as other two-dimensional materials. SPELEEM, low-energy electron microscopy (LEEM) equipped with an energy analyzer, is able to acquire the real-time information of both the chemical and structural properties of the material.

LEEM was first invented by Ernst Bauer in 1962 and became operational in 1985 [129]. Figure 13(a) shows a schematic of the principle of a LEEM system. Initially, electrons emitted from an electron gun are accelerated by a high voltage (15-20 keV). Then the electron beam is focused by a set of objective lens and deflected by a

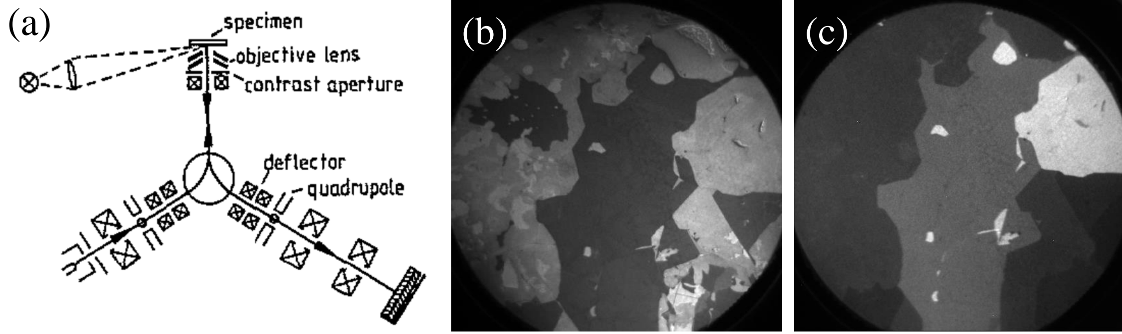

Figure 13: (a) Schematic of the experimental setup for LEEM [129]. (b) Typical LEEM image of a few-layer C-face epitaxial graphene. The starting voltage is 2.8 eV and the field of view (FOV) is 50 μm. (c) Typical XPEEM image of the same sample area. The photon energy is 133 eV and the starting voltage is 26 eV.

magnetic beam deflector (see Figure 13(a)). While approaching the sample surface, the electron beam is decelerated by the potential of the sample to a lower energy range (1-100 eV). The elastic mean free path of such low-energy electrons is usually below 1nm, so the measurement has very high surface sensitivity. After scattered from the surface, electrons accelerate again, pass the deflector and projector lens, and move into the detector. A typical LEEM image of C-face epitaxial graphene is given in Figure 13(b). Contrast in the LEEM image usually results from both diffraction and phase contrast. In the case of Si-face graphene, the contrast can be a good indicator for the thickness [119].

Another important function of the SPELEEM system is X-ray photoemission electron microscopy (XPEEM). The physics principle of XPEEM is the same as that of XPS, but it has a spatial imaging ability. Instead of illuminating the surface with electrons in LEEM, the sample is illuminated with soft X-rays in XPEEM. Photoelectrons are collected in the same way as in LEEM except that an energy filter is used to select electrons with a specific energy for imaging. Figure 13(c) is an XPEEM image of the same region as Figure 13(b) at Si 2p binding energy (~101 eV), where brighter regions represent higher Si 2p intensity. In this image, the Si 2p intensity is from bulk SiC. Therefore, brighter contrast also indicates fewer layers of

graphene.

In addition to LEEM and XPEEM, the SPELEEM system also holds other advanced techniques, including mirror electron microscopy (MEM), micro low-energy electron diffraction (μ-LEED), micro angle-resolved photoemission spectroscopy (μ-APRES) and dark field (DF) imaging. This thesis uses all of these techniques to characterize graphene and discusses them in the order that they are presented. Experiments were carried out at the I311-PEEM beamline at MAXlab synchrotron radiation laboratory in Sweden and the Nanospectroscopy beamline at Elettra Sincrotrone Trieste in Italy.

CHAPTER III

INTERACTION BETWEEN SILICON AND GRAPHENE

Carbon and silicon are the most important elements in our lives. While carbon is the basis of life, silicon is the basis of technology. What happens if these two basic elements interact? It turns out to be a very interesting scientific question. This chapter aims to study a small subsection of this question; What happens if silicon interacts with epitaxial graphene? In fact, silicon is extremely important for epitaxial graphene grown by the confinement-controlled sublimation method. Because graphene growth is determined by silicon vapor pressure. Silicon vapor pressure controls the graphene growth temperature, growth speed, and its physical structure (see Chapter IV). Therefore, it is critical that we understand the interaction between silicon and graphene.

In this chapter, excess silicon is deposited onto the graphene surface and then annealed at various temperatures. At low temperatures, silicon intercalates into the graphene-SiC interface. At high temperatures, silicon tends to bond with carbon atoms of graphene to form SiC.

3.1 Silicon Intercalation Into Graphene-SiC Interface

For epitaxial graphene grown on SiC, both the surface of graphene and the interface between graphene and bulk SiC play a significant role in graphene growth and transport properties [40, 41, 97]. It is well known that C-face graphene can be grown much faster than Si-face graphene. The reason is recognized as different silicon diffusion kinetics though those two different faces. The transport properties of two faces are also quite different. The mobility on C-face graphene is almost an order of magnitude higher than on Si-face, although Si-face usually has a more ordered graphene

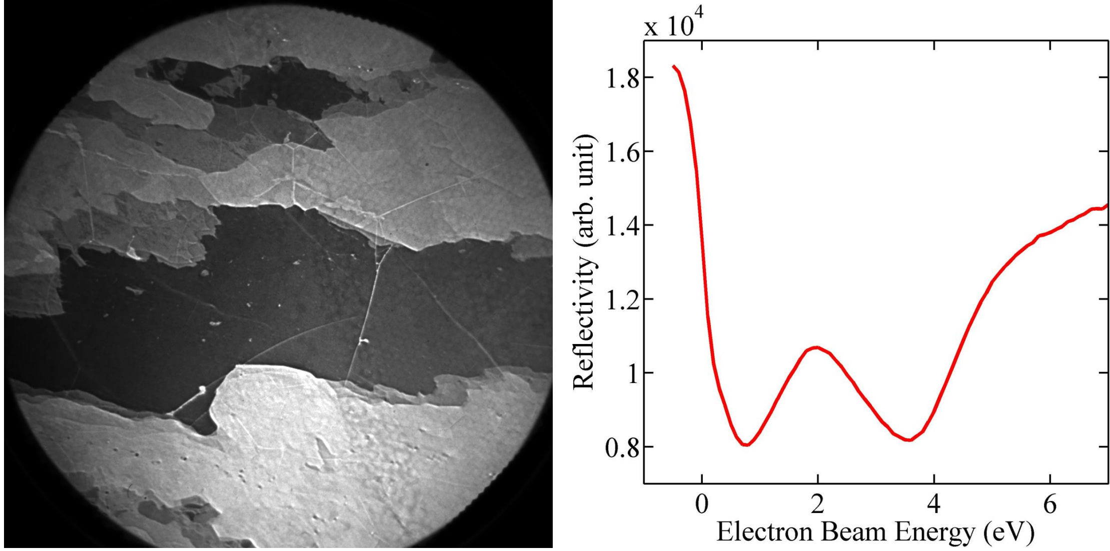

Figure 14: (a) 50μm×50μm LEEM bright field image of 6H C-face sample at -0.05 V. (b) LEEM reflectivity spectrum from the center dark region of (a).

structure.

It is very important to understand and control the interface structure between graphene and SiC. Work has already been done on characterizing the graphene-SiC interface using LEED, STM [98] and XRD [44, 45]. Along with work on modifying the interface by intercalating various atomic species including hydrogen [47], germanium [46], and lithium [48].

This section discusses how silicon is intercalated into the C-face graphene-SiC interface using a complete surface analysis of LEEM, XPEEM, XPS, and LEED data. A large amount of silicon is proved to intercalate into the interface through heterogeneous sites [115] starting from 970 °C , and the intercalation becomes very rapid at 1020 °C. Graphene used here was grown from n-doped 6H-SiC by the CCS method [116] at 1550 °C for 20min, and thermally annealed at 500 °C to clean the surface.

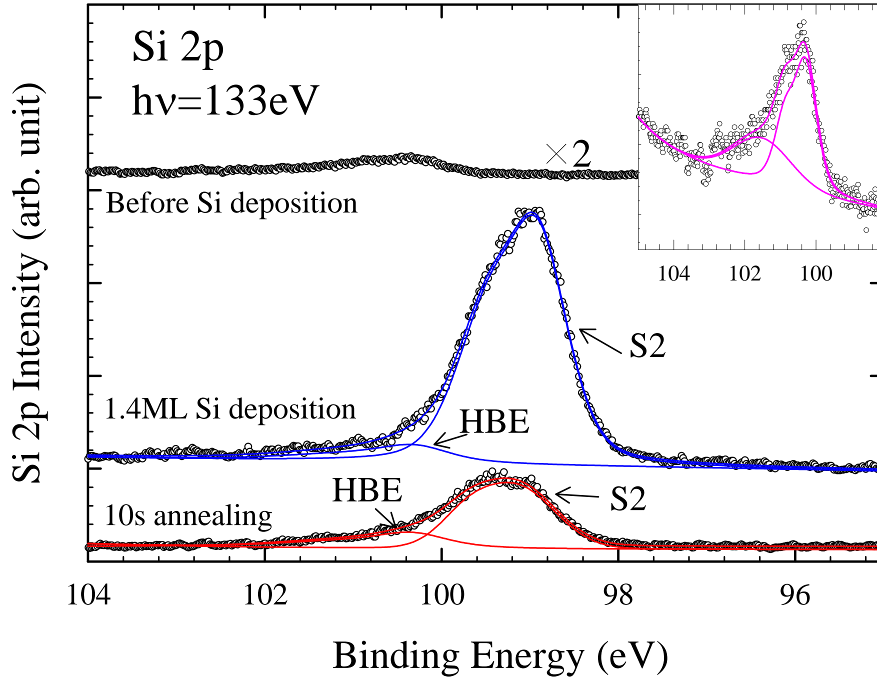

Figure 15: Si 2p core-level spectra and fits from the two monolayer (ML) graphene region. Spectra are shown for before Si was deposited, after 1.4 ML of Si was deposited, and after Si was annealed at 1020°C for 10 seconds. The insert shows an expanded view of the spectrum before Si deposition. The photon energy was $h\nu = 133$ eV. Solid lines are the fit peaks.

3.1.1 Surface Characterization

Figure 14(a) is a 50 μm FOV LEEM image showing the initial graphene structure. The black region in the center is a $\sim$50μm$\times$20μm uniform C-face graphene area, where the LEEM reflectivity curve is shown in Figure 14(b). Former research on quantized oscillation has indicated a direct relationship between number of graphene layers and number of dips in LEEM reflectivity spectrum [119]. Therefore, the center dark region is treated as bi-layer graphene. XPS and XPEEM results shown later also indicate this area as bi-layer graphene.

A series of Si deposition and annealing experiments were carried out on the sample while keeping the same LEEM FOV. Therefore, the whole area in Figure 14(a) can be tracked during and after measurements to make sure data were acquired at the

same sample region. Figure 15 shows the Si 2p XPS spectra from the bi-layer region before Si deposition, after 1.4-layer Si deposition, and after 10 seconds annealing at 1020 °C. The inset is an expanded view of spectrum before Si deposition to show the Si 2p signal from SiC underneath the graphene. Note that the SiC-Si intensity is much lower than that after Si deposition because of attenuation of the photoelectron by bi-layer graphene. The photon energy is $h\nu = 133$ eV, and the kinetic energy for photoelectron of Si 2p is about 30 eV, so the measurement highly surface sensitive. The spectra in Figure 15 are fitted with a combination of spin-orbit split Si $2p_{1/2}$ and Si $2p_{3/2}$ peaks with 0.6 eV separation and a small peak at higher binding energy (HBE), as shown in the solid line. The HBE peak is assumed to be from the interface [52].

After 1.4ML of Si was evaporated at room temperature onto this bi-layer graphene region, the Si 2p peak clearly shifts 1.4 eV to lower binding energy and becomes much larger than that of the spectrum before Si deposition. Annealing at 970 °C does not significantly affect the spectrum. However, after 10s annealing at 1020 °C, the Si 2p peak decreases in intensity and shifts 0.22 eV to the higher binding energy (see Figure 15).

The apparent loss of Si signal could be a result of four main effects: (1) evaporation of about a monolayer of silicon from the surface, (2) diffusion of a similar amount of Si to heterogeneous defect sites to form Si islands or other three-dimensional structures outside the photon beam, (3) intercalation of Si between graphene layers, and (4) diffusion into the graphene-SiC interface. In the first and second cases, the Si signal decreases would result from Si leaving of the probe area, while in the third and fourth cases, the Si 2p intensity decrease may have resulted from the photoelectron attenuation by graphene above Si. As we will show, further experiments and analysis will indicate that the intercalation of Si into the graphene-SiC interface accounts for most of the intensity drop.

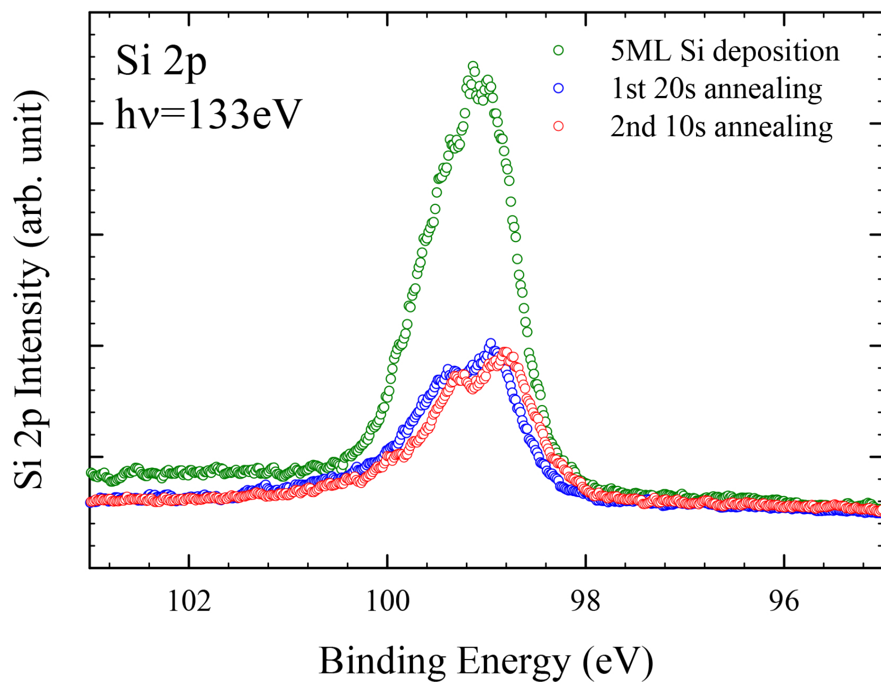

Figure 16: Si 2p intensity after 5 ML of Si has deposited (green open circles), after the film has been annealed for 20 sec at 1020°C (blue open circles), and after additional 10sec annealing at 1020°C (red open circles). The small shift of peak following the second annealing may results from surface work function change.

First, Si evaporation can be easily ruled out because the Si evaporation rate at 1020 °C is less than 0.3 ML [49, 50]. Furthermore, Figure 16 shows that additional annealing has no further effect on the Si 2p intensity after the first annealing, indicating that the silicon on the sample is stable to the high temperatures once initially annealed. This stability also rules out substantial diffusion to heterogeneous sites. In fact, some Si does initially diffuse to heterogeneous sites [115]; however, the stability to further annealing suggests that this type of material flow quickly becomes negligible. Three-dimensional Si islands can be also ruled out for two reasons. First, at least 8-layer Si islands are required for the loss of Si 2p intensity. If these thick islands formed, they would be seen by both LEEM and LEED, while we did not see the islands. In addition, islands that cause the decrease in the pure Si 2p intensity could also cause an increase in SiC-Si 2p intensity, since more area of SiC would be exposed after islands formed, which was also not observed.

We performed three similar Si deposition and annealing cycles on the same bi-layer graphene region. After each annealing, the Si 2p peak dropped from its initial deposition value and remained stable with additional annealing at 1020 °C. Moreover, the Si 2p intensity increased after each cycle. In other words, the post-annealed stable Si built up within the bi-layer graphene region, which was either intercalation between graphene sheets or into the graphene-SiC interface.

We point out that none of the Si is intercalated between graphene sheets. This can be demonstrated by using μ-LEED and taking advantage of the unique stacking of C-face graphene. C-face epitaxial graphene consists of sheets that are commensurately rotated at non-Bernal angles [51, 53]. This stacking results in a graphene supercell that can be seen in STM [51, 54, 55]. Because the size of each supercell is much smaller than the typical size of LEED beam and because the vertical displacements are small ($\sim 0.005nm$) [56], the typical LEED pattern for C-face graphene is an incoherent average of spatially separated supercells to form the diffuse ring shape at

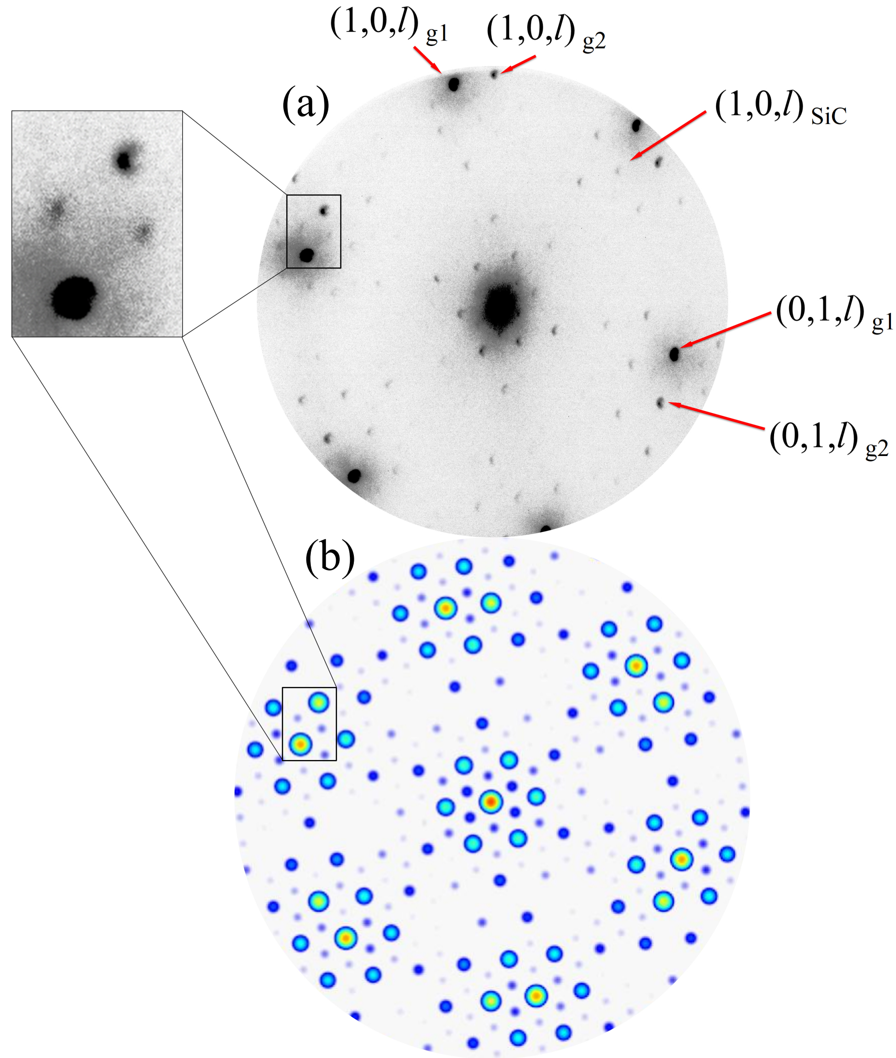

Figure 17: (a) $\mu-$LEED image at 96 eV from the bi-layer graphene region in Figure 14, where the Si 2p data is taken in Figure 15 and Figure 16. The principle diffraction rods from two rotated graphene sheets are marked. The inset shows a blowup of the reconstruction pattern. The reciprocal lattice corresponds to a $(\sqrt{57}\times\sqrt{57})_G\text{R}6.59^\circ$ reconstruction. (b) Simulated LEED pattern from the same $(\sqrt{57}\times\sqrt{57})_G\text{R}6.59^\circ$ structure commensurated with SiC

graphene radius [97].

Figure 17 is the μ−LEED image from the same bi-layer region before silicon deposition. The image shows a reconstruction pattern from two vertically stacked but rotated graphene layers, $g1$ and $g2$. Two graphene sheets are commensurately rotated by 13.17°. This commensurate angle gives rise to a supercell that can be used to index all spots in Figure 17. The supercell corresponds to a $(\sqrt{57}\times\sqrt{57})_G$R6.59° in graphene units. The superstructure is not a result of adsorbates since it can persist up to 1100 °C. In addition, this $\sqrt{57}$ structure is also commensurate with a $(6\times6)_{SiC}$ SiC cell with only $\sim 0.4\%$ strain, as shown in Figure 18. Therefore, the six SiC reciprocal spots coincide with some graphene reconstruction spots as marked in Figure 17. The intensity of these six spots has contributions from both the graphene corrugation induced by the commensurate bi-layer structure as well as the SiC layer underneath. However, the attenuation of elastic electrons reduces most of the intensity from the SiC. Thus, the intensity of observed spots is mainly from the graphene $\sqrt{57}$ structure. After 7-layer Si deposition and annealing, there is little effect on the LEED pattern. If Si is intercalated between graphene sheets, this large amount of Si would dramatically change the vertical distance between graphene sheets and would destroy the small reconstruction corrugation, causing most of LEED spots to disappear. This indicates that the Si must diffuse into the graphene-SiC interface.

Another direct evidence for Si intercalation into the graphene-SiC interface comes from comparing the C 1s spectra before and after Si intercalation. Figure 19 shows that the SiC-C 1s signal disappears after Si intercalation. This suggests that a large portion of Si has diffused to the graphene-SiC interface and blocked the SiC-C 1s signal without reducing the graphene-C 1s signal. Had Si intercalated between graphene sheets, the intensity of graphene-C 1s would also have decreased.

A similar attenuation effect caused by interfacial Si can also be seen in normal LEED. Figure 20 shows the LEED pattern from another region on the same sample

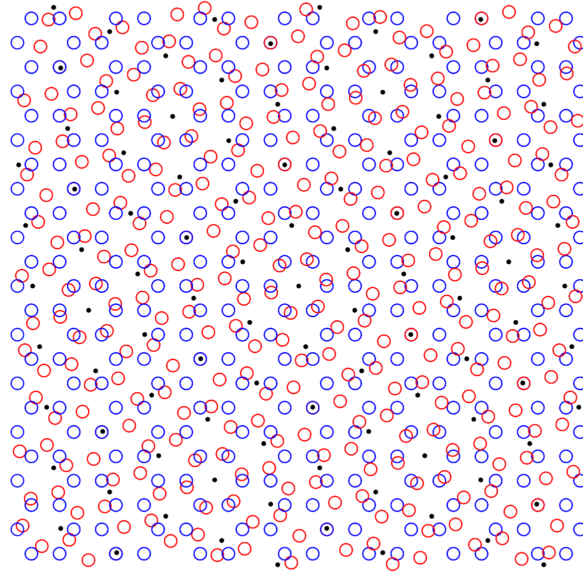

Figure 18: Reconstruction lattice diagram of two graphene sheets (red and blue circles) $(\sqrt{57}\times\sqrt{57})_G$R6.59° and top layer of SiC (black dots) $(6\times6)_{SiC}$. SiC and the red graphene sheet is rotated by 6.59° and 13.17° from the blue graphene sheet respectively

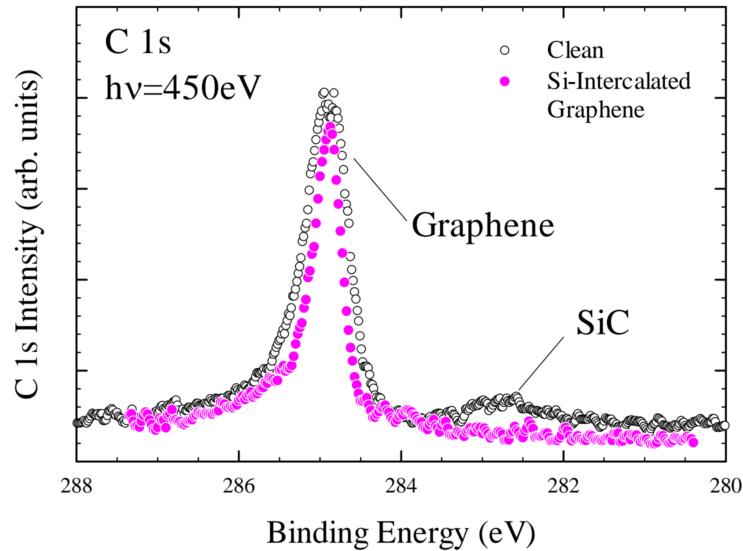

Figure 19: C 1s spectra before Si intercalation (open circles) and after intercalation (pink dots).

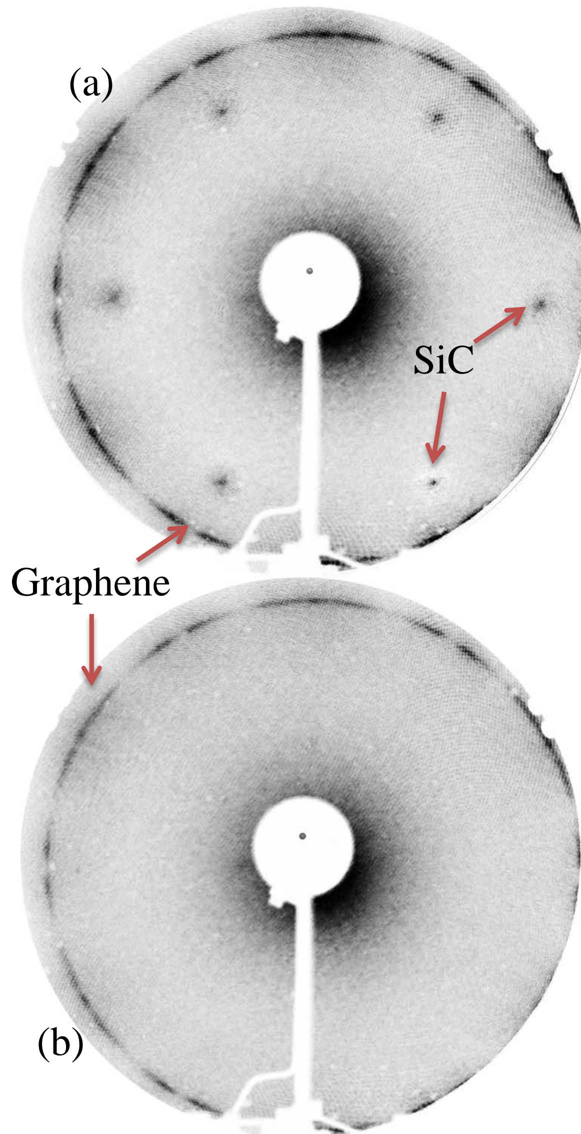

Figure 20: LEED patterns from; (a) covered graphene region where Si was not deposited, and (b) from center graphene region where 7 ML of Si was deposited and annealed. Note that the weak, but visible, SiC (1×1) pattern in (a) is not visible in (b). Both images were made at 72 eV.

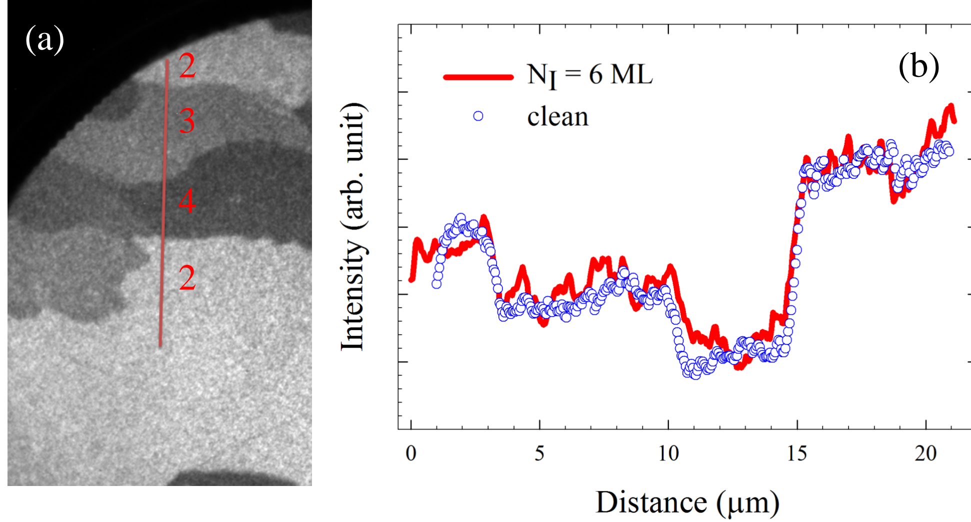

Figure 21: (a) Clean sample XPEEM image using the SiC-Si 2p peak at a kinetic energy of 25.8 eV with photon energy $h\nu = 133$ eV. The labels indicate the number of graphene layers determined by LEEM reflectivity and XPS spectra. (b) Intensity profile across the vertical bar in (a) from the clean sample (blue open circles) and after ∼7 ML of Si has been deposited and ∼6.3 ML intercalated into the interface (solid red line).

after 7-layer of Si was deposited and annealed at 1020 °C. Figure 20(a) is taken on the covered graphene region without any Si deposited. The pattern is a typical multi-layer C-face graphene pattern, which includes both the graphene ring and SiC (1×1) surface. Most of the intensity of SiC spots is from thin areas of the sample because of the low electron mean free path at 72 eV. Figure 20(b) reveals a pattern from the part of the sample exposed to Si after annealing. In this region, the LEED pattern shows only the graphene ring. If the Si evaporated or remained on the graphene surface, the diffraction pattern would be the same as in Figure 20(a) or uniformly attenuated. Instead, only the SiC spots have disappeared. Like the SiC-C 1s intensity, the diffracted intensity from SiC has been attenuated by the intercalated Si. Five images on different parts of the sample within the exposed area and five images outside the area showed similar results. Thus, it is unlikely that thickness variations within the sample are the cause of the lost SiC diffraction intensity.

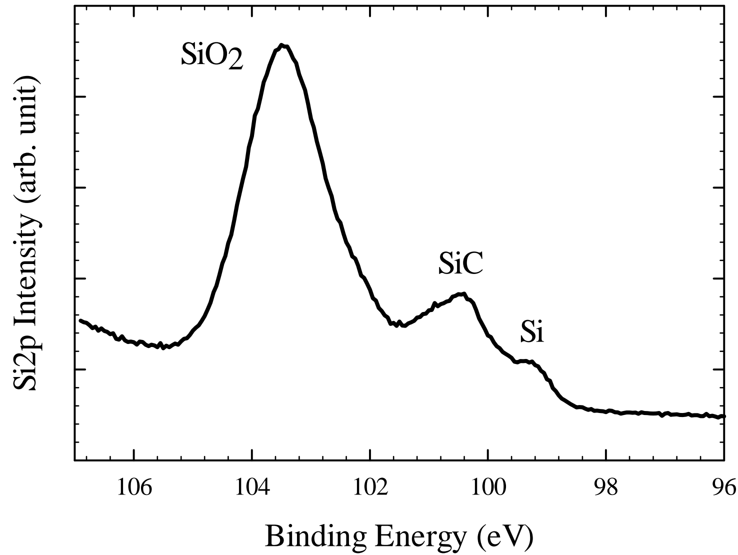

Figure 22: The Si 2p core-level spectrum after the 6.3 ML Si-intercalated sample was exposed to air at room temperature and subsequently heated to 1200°C in vacuum.

Neither LEED nor XPS measurements showed the evidence of Si bonding to carbon atoms and converting to SiC after annealing at 1020 °C. Figure 21(a) is the XPEEM image using SiC-Si 2p binding energy. Since varying thicknesses of graphene attenuate the SiC signal differently, the image contrast represents graphene thickness variances (brighter areas are thinner). Figure 21(b) shows cuts through a two-, three-, four-, and two-layer graphene region of the sample as marked in Figure 21(a). The cuts were before and after Si deposition and annealing. The plot shows that after Si intercalation, neither the graphene boundary nor graphene thickness changes.

3.1.2 Graphene Structure Model after Si Intercalation

So far, we have shown that Si intercalates into the graphene-SiC interface. A quantitative determination of how much Si has intercalated requires a detailed analysis of the XPS, XPEEM, and LEEM data from each deposition and annealing cycle. From LEEM mirror mode images, which are very sensitive to surface height variations, no significant change is observed. Thus, Si can be assumed to be uniformly distributed both on the surface and in the interface in the model. Figure 22 shows the XPS

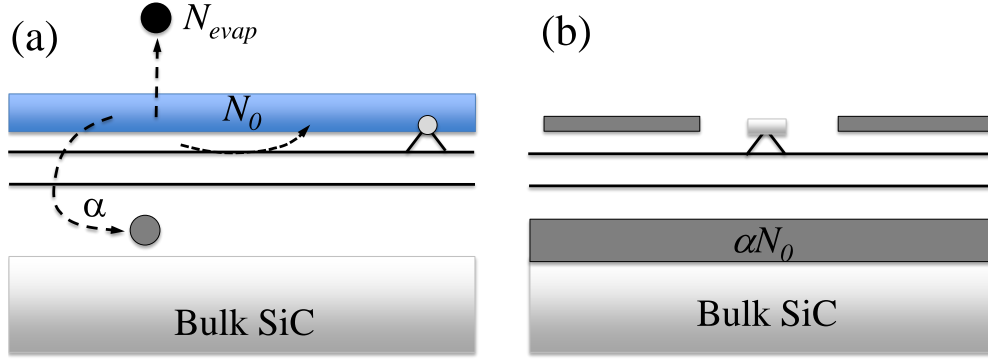

Figure 23: (a) Model of how an N_i monolayer Si film is redistributed after annealing. Some of the surface Si has formed a carbide bonded to the top graphene layer. (b) Schematic of the surface after 7 ML have been deposited and annealed. Note that the surface Si and surface carbide are treated as part of the total surface coverage.

spectrum of the same sample after exposed to the air and annealed to 1200 °C. The formation of silicon dioxide indicates a stable Si complex on the surface because it can oxidize in the air, but the interfacial Si cannot. Therefore, a small portion of Si is assumed to bind to the carbon atoms of the top layer of graphene.

The model used to analyze the experimental results is shown schematically in Figure 23. In each cycle N_i (i=1,2, and 3) layers of Si are deposited on the surface (N_1 = 0.7 ML, N_2 = 1.4 ML and N_3 = 5 ML). After each annealing at 1020 °C, N_{ei} layers evaporate, $N_{ia} = \alpha_i N_i$ layers move to the SiC interface, and the remaining $N_{ib} = (1 - \alpha)N_i - N_{ei}$ are bound at the graphene-vacuum interface. As discussed above, the model does not include intercalation of Si between graphene layers. The total Si intercalated into the SiC interface is $N_a = \sum_i N_{ia}$. The measured Si 2p photo-electron signal after annealing, $I'^{(i)}_{Si}$, has contributions from (1) the Si in the graphene-SiC interface that is attenuated by both the Si within the interface and the graphene above it and (2) the Si on the surface. The intensity before annealing, $I^{(i)}_{Si}$, depends essentially on the amount of Si deposited because the surface Si and the graphene are able to attenuate any Si signal effectively from the interface. This assumption is reasonable because the electron mean free paths in graphene and Si (λ_g and λ_{Si}, respectively) are small (see below) at the kinetic energies used in these

experiments.

Assuming that the cross sections of Si 2p are the same for all kinds of bonding, the relative intensity change $I'^{(i)}_{Si}/I^{(i)}_{Si}$ can be written as

$$\frac{I'^{(1)}_{Si}}{I^{(1)}_{Si}} = 1 - \alpha_1 + \alpha_1 e^{-2d_g/\lambda_g}[1 - (1-\alpha_1)N_1(1 - e^{-d_{Si}/\lambda_{Si}})] \tag{11a}$$

$$\frac{I'^{(2)}_{Si}}{I^{(2)}_{Si}} = \{N_2(1-\alpha_2) + N_{1b} - N_{2e} + (N_{1a} + N_2\alpha_2)e^{-2d_g/\lambda_g}$$
$$\times [1 - (N_2(1-\alpha_2) + N_{1b} - N_{2e})](1 - e^{-d_{Si}/\lambda_{Si}})\}/\{(1 + [N_2 + N_{1b} - 1]e^{-d_{Si}/\lambda_{Si}})\} \tag{11b}$$

$$\frac{I'^{(3)}_{Si}}{I^{(3)}_{Si}} = [N_{1b} + N_{2b} + (1-\alpha_3)N_3 - N_{3e} + e^{-2d_g/\lambda_g}/(1 - e^{-d_{Si}/\lambda_{Si}})] \times [(1 - e^{-d_{Si}/\lambda_{Si}})] \tag{11c}$$

where d_{Si} and d_g are the bulk Si and graphene interlayer spacing, respectively. In Equation 11a, the evaporated Si in the first step, N_{1e}, is assumed to be zero because of the formation of a partial monolayer stable carbide, as discussed above. Furthermore, in the third deposition (Equation 11c), where the Si interface layer has become very thick (i.e, $N_a d_{Si} \gg \lambda_{Si}$), the interface Si is treated as an infinite film.

The mean free path in Si at the kinetic energies in the experiments is 3.3Å[57] The mean free path in graphene at such low kinetic energy is less well known and estimated by comparing the Si 2p intensity from a 5-layer Si film on graphene to the Si 2p from SiC attenuated by two graphene layers, which is done by assuming that the Si film is uniform and that SiC is also bulk terminated. λ_g is therefore estimated to be 2.8 ± 0.1Å.

The bulk Si evaporation rate is used as the upper limit estimate for N_{ei} for both the second and third annealing cycles. This yields $N_{e1} = N_{e2} = 0.3$ ML, which is small compared to the total deposited Si. Therefore, it does not affect the calculation of the intercalated Si. However, it does affect how much Si remains on the surface.

Using the experimentally integrated Si 2p intensities, Equations 11a-11c can be

---

*Estimated from bulk evaporation rate.

Table 1: Fit parameters for each cycle. All coverages are in monolayers.

Cycle	Deposited Si	α_i(%)	Intercalated	$N_e{}^*$	Surface
1	0.7	69	0.5	0	0.2
2	1.4	71	1.0	0.3	0.1
3	5.0	96	4.8	0.3	-0.1
Total	7.1	89	6.3	0.6	0.2-0.5

solved for the three cycles. The results are summarized in Table 1. A total of 6.3-layer of Si were intercalated into the graphene-SiC interface. The 0.8 ML either evaporated, diffused to heterogeneous sites, or remained on the surface. If the evaporation rate is set to be 0.3 ML per cycle as discussed above, then an upper limit of 0.8-0.6=0.2 ML of Si remains unaccounted for (presumably by diffusion to heterogeneous sites). Another way of estimating the Si remaining on the surface is to compare graphene C 1s spectra before and after intercalation, which yields about half monolayer of Si above the graphene.

The reason why Si prefers to intercalate is not known. However, at 1020 °C, the SiC phase diagram predicts that any excessive Si will stay segregated. Since the excessive Si has the choice of wetting either the graphene on the surface or both the graphene and the SiC interface, the lower-energy choice is intercalation into the interface. From an equilibrium point of view, this excess Si should bond to excess carbon, which is graphene, to form a new stable SiC structure. The reason why the Si does not bond to carbon is probably because of the low temperatures used in these experiments. Therefore, in next section, higher temperatures are explored; The results show more direct and interesting interaction between graphene and silicon.

3.2 Graphene-SiC Transformation on C-face Graphene

The last section has shown that up to 6 layers of Si rapidly diffuse from the C-face graphene surface to the graphene-SiC interface at 1020 °C. The next goal is to reverse the process and remove the intercalated Si to control and modify the interface. The idea is to anneal at higher temperatures so that the interfacial Si can evaporate and diffuse out through the heterogeneous sites [115]. However, to prevent more graphene layers from forming, the higher temperatures have to be lower than the graphene growth temperature, which is around 1550 °C.

In this section, Si is deposited on C-face epitaxial graphene and then annealed at various higher temperatures. LEED and XPS are used to analyze the surface structure. The results show that Si on the graphene surface is able to bind to the carbon atoms of graphene to form SiC before significant evaporation.

3.2.1 LEED Measurements of SiC Formed on C-face Graphene

This experiment consists of two C-face graphene samples (A and B). Both were grown from an n-doped ($n = 2 \times 10^{18}\text{cm}^{-2}$) 4H-SiC using the CCS method. Since there is no LEEM measurement on these two samples, the thickness is determined by an ellipsometer. Sample A is 34Å and sample B is 24Å. Then sample A and B had 20Å and 100Å silicon deposited, respectively, by E-beam evaporation, and transferred into a UHV anneal/LEED chamber immediately to minimize oxidation. The oxidized Si is estimated to be a few angstroms [58]. The annealing chamber is connected to the LEED chamber in the same UHV conditions. Thus, no further oxidation took place between the annealing step and the LEED measurement.

Figure 24 shows the LEED images of sample A after 20Å Si deposition and annealing at three different temperatures for one minute. The first annealing temperature is 1000 °C, at which temperature Si intercalated into the interface as discussed in the previous section. Figure 24(a) confirms the intercalation by showing only C-face

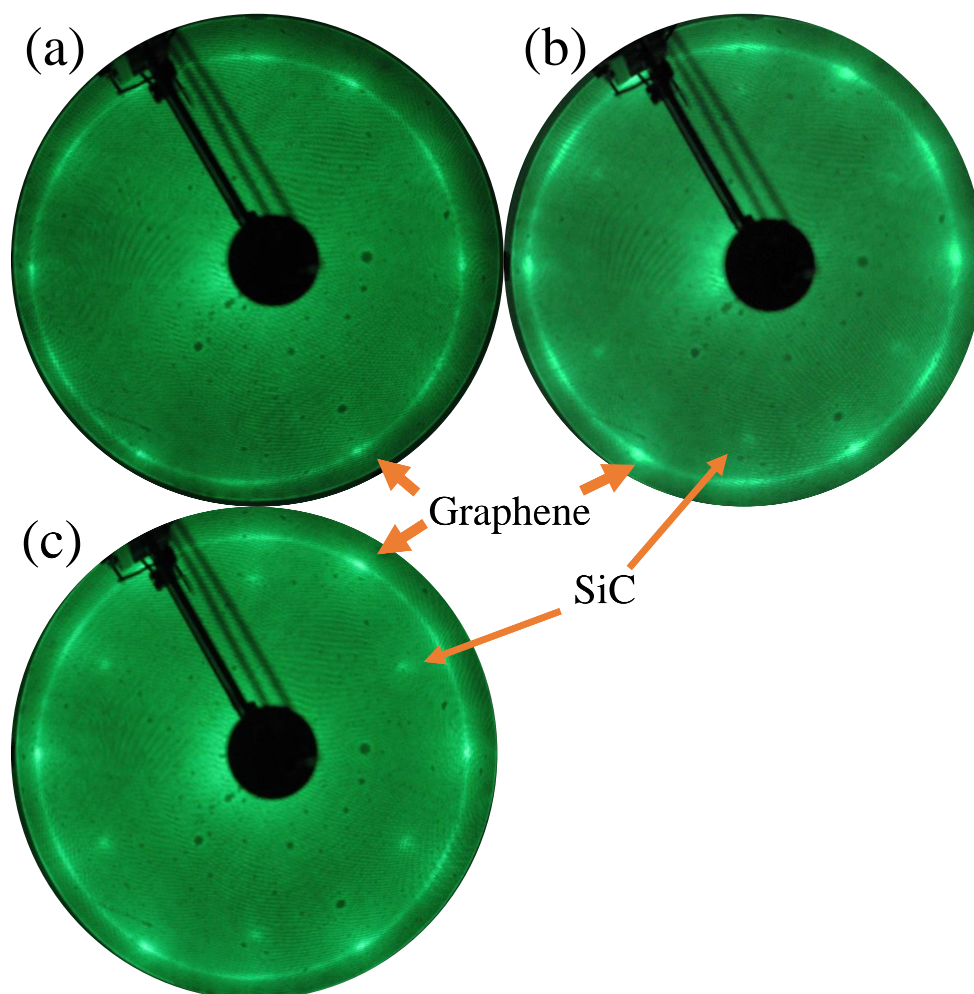

Figure 24: LEED images of sample *A* after Si deposition and annealing at; (a) 1000 °C, (b) 1100 °C, and (c) 1200 °C for 1 minute. All LEED images were taken at 60 eV.

graphene pattern (no SiC spots). Since one minute is too short for the entire Si to evaporate, and the LEED image exhibits no Si related pattern, the leftover Si must have remained at the interface. Note that no SiC (1×1) spots show up because of the attenuation by both thick graphene ($\sim$ 10 layers) and the interfacial Si.

Then the same sample was annealed again at 1100 °C and 1200 °C. LEED images after each annealing are shown in Figure 24(b) and (c). Ordered SiC (1×1) spots started to appear after 1100 °C annealing and became more apparent after the 1200 °C annealing. Both images look like thin C-face graphene (2 $\sim$ 3 layers) LEED patterns because of a smaller attenuation of the SiC signal. However, it is impossible for 7-8 layers of graphene to disappear at such low temperatures. Therefore, the only explanation for the LEED patterns is that, starting from 1100 °C, the interfacial Si evaporated and diffused out to the surface. Once at the surface, the Si bonded to carbon atoms of graphene to form SiC (1×1) structure. More interfacial Si diffused out at 1200 °C than that at 1100 °C and continued to form SiC. The formed surface SiC should be no more than a monolayer since the graphene signal is still strong without significant attenuation by the SiC that has formed above graphene.

It is important to note that, in Figure 24(b) and (c), the surface SiC (1×1) spots are rotated by 30 degrees from the graphene (1×1) spots, which indicates that the newly formed surface SiC has the same single orientation as the bulk SiC. Furthermore, since the surface SiC forms based on the orientation of the top graphene layer, these results also imply that the top graphene layer is single oriented with 30° from the bulk SiC. If the top layer is polycrystalline and has many other orientations, the surface SiC will follow these orientations, and its LEED pattern should be a diffused ring similar to the graphene ring. Thus, the C-face graphene commensurate rotation that we mentioned in Chapter II occurs only in graphene layers below the top layer.

So far, LEED measurements have shown that thin SiC structure started to form on top of graphene by depositing Si and annealing at 1100 °C. The reason why only

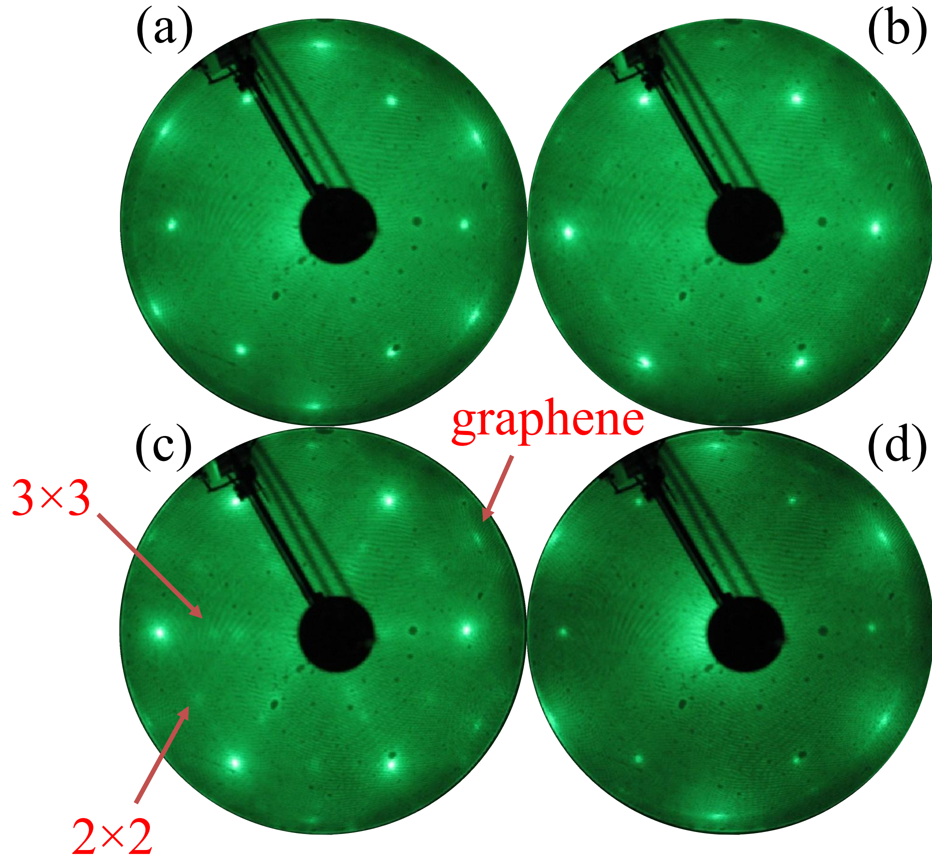

Figure 25: LEED images of sample B after Si deposition and annealing at; (a) 1100 °C, (b) 1200 °C, (c) 1300 °C, (d) 1400 °C for one minute. SiC $(2\times2)_{SiC}$ and $(3\times3)_{SiC}$ reconstruction patterns are marked in (b) and (c). All LEED images were taken at 60 eV.

a partial SiC layer formed presumably results from the small amount of initial Si deposition (20Å). Therefore, for sample B, we deposited 100Å Si following the same annealing steps to check whether more SiC could form.

Figure 25 shows the LEED images of sample B after 100Å of Si was deposited and annealed at four different temperatures. Note that sample B was also annealed at 1000 °C at first. The LEED pattern was exactly the same as that of sample A, shown in Figure 24(a). Figure 25(a) shows the pattern after the 1100 °C annealing (same temperature as in Figure24(b)). The SiC (1×1) spots are much stronger than those of sample A. This confirms that the surface SiC structure started to form after

1100 °C annealing. However, given that the graphene ring was also visible and not totally attenuated, the surface SiC has to be only a few layers ($\sim 1-2$ layers) based on the electron mean free path of ~1nm. Therefore, most of Si still remained at the graphene-SiC interface.

Then sample B was heated to the same 1200 °C annealing temperature and in the same way as sample A in Figure 24(c). However, the LEED pattern is very different. Figure 25(b) shows that SiC (1×1) became dominant and graphene ring had almost disappeared with only weak graphene (1×1) spots remaining. Moreover, $(2\times2)_{SiC}$ and $(3\times3)_{SiC}$ reconstruction patterns started to show up in the LEED and became more evident when annealed to 1300 °C (see Figure 25(c)).

The disappearance of the graphene ring indicates that, after annealing at the higher temperature, more interfacial Si had diffused back onto the surface and attenuated the graphene signal. The $(2\times2)_{SiC}$ and $(3\times3)_{SiC}$ reconstruction structures are two patterns often seen when the SiC surface is decorated with Si and annealed $\sim$ 1100 °C in UHV [61]. The reason why a higher temperature (1200 °C) was required in this experiment than it was in UHV is because of the closed crucible, which raised the Si vapor pressure to a much higher level than in the UHV environment.

Figure 25(d), the LEED image after annealing at 1400 °C, shows all reconstruction patterns disappeared, while the graphene ring returned and SiC (1×1) became weaker. This LEED pattern indicates that most of the surface Si evaporated out at 1400 °C and an ordered and thin SiC film was left on the surface.

3.2.2 XPS Analysis on SiC Formed on C-face Graphene

In the last section, LEED experiments were used to prove that the interfacial Si started to diffuse back onto graphene surface and form SiC by bonding to carbon atoms of graphene after annealing to 1100 °C. XPS measurements and analysis of these two samples were also performed after the final annealing; 1200 °C for sample

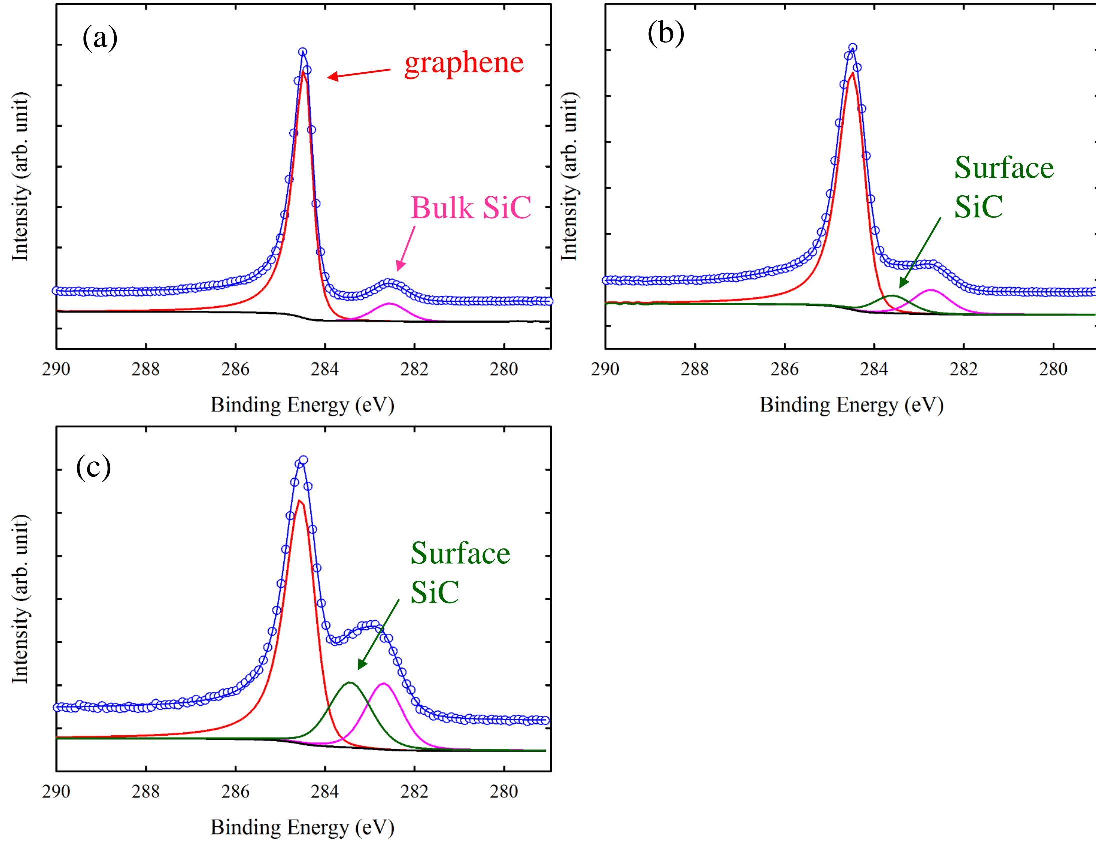

Figure 26: C 1s core-level spectra and fits from (a) sample A before Si deposition and annealing, (b) sample A after Si deposition and annealing at 1200 °C, (c) sample B after Si deposition and annealing at 1400 °C. Open circles are acquired data and solid lines are the fits. Fitted peaks and background have been offset down to make figures more clear. The photon energy is 1486 eV.

A and 1400 °C for sample B.

Figure 26(a) shows the C 1s core-level spectrum of sample A after graphene growth and before Si deposition. The graphene C 1s peak at 284.49 eV was fitted using a Lorentzian asymmetric lineshape in CasaXPS with an asymmetry index 0.34. The SiC-C 1s peak at 283.45 eV was fitted using a summed Gaussian-Lorentzian function with a 30% Lorentzian. As shown in Figure 26(a), the graphene and SiC peaks are well separated by 2 eV typical for the normal C-face graphene. Note that the data and the envelop of the fitted peaks were offset in intensity to make peaks clearer.

After the Si was deposited and annealed at 1200 °C, a new peak appeared, shown

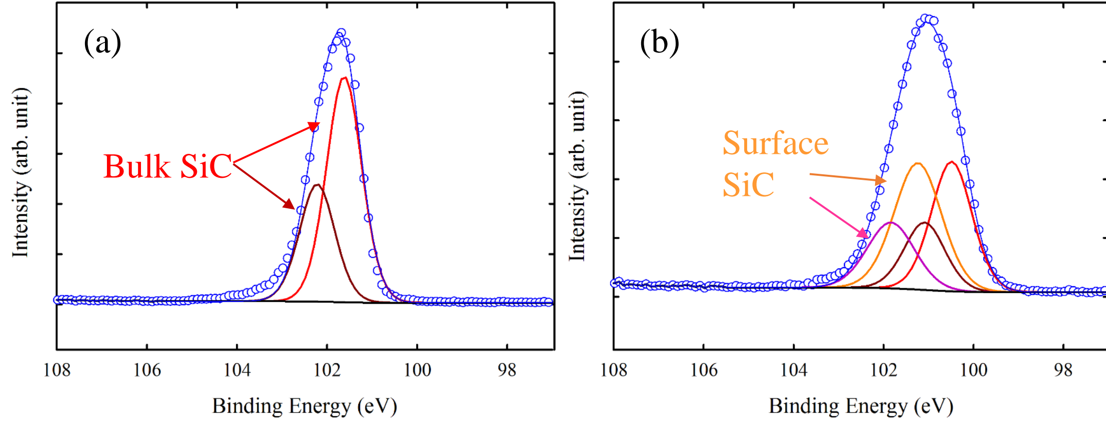

Figure 27: Si 2p core-level spectra and fits from sample B (a) before Si deposition and annealing. (b) sample A after Si deposition and annealing at 1400 °C. Open circles are acquired data and solid lines are the fits. The photon energy is 1486 eV.

in Figure 26(b). From the discussion in the previous section, the additional peak should be the surface SiC-C 1s peak. However, the binding energy of surface SiC is higher than that of bulk SiC. The reason for the increased binding energy is the band bending on graphitized C-face SiC [88, 87]. Therefore, the C 1s spectrum confirms the formation of surface SiC after depositing Si and annealing. It is worthwhile to point out that the graphene to bulk SiC peak ratio shows only a small change after annealing. This indicates that little or no Si remains at the graphene-SiC interface to attenuate bulk SiC after annealing at 1200 °C.

The C 1s spectrum of sample B after 1400 °C annealing is shown in Figure 26(c). The ratio between graphene and bulk SiC is smaller than that of sample A because of fewer graphene layers of sample B (24Å). Since the amount of deposited Si on sample B is much higher than that on sample A, the surface SiC-C 1s peak is also higher. This is also consistent with the LEED image in Figure 25(d), which shows that the SiC (1×1) spots are stronger and narrower (i.e., more ordered).

Si 2p spectra were also taken before and after Si deposition and annealing (see Figure 27(a) and (b)). In (a), since the Si 2p peak is only from SiC, the peak can be fitted with a single set of spin-orbit split Si $2p_{1/2}$ and Si $2p_{3/2}$ peaks (0.6 eV

separation), the same as in Figure 15. After depositing Si and annealing at 1400 °C, the width of the peak expanded (see Figure 27(b)), which implies the involvement of additional peaks. The new spectrum can be fitted by adding another set of Si $2p_{1/2}$ and Si $2p_{3/2}$ peaks from SiC on the surface. The binding energy separation between two sets of spin-orbit split peaks is 0.75 eV, which is also consistent with C 1s spectra splitting.

In summary, both LEED and XPS results prove that the interfacial Si intercalated into C-face graphene at 1000 °C is able to diffuse back onto the graphene surface after annealing at high temperatures (1100 °C-1400 °C). Once at the surface, it forms SiC by binding with carbon atoms of the top graphene layer.

CHAPTER IV

SEMICONDUCTING GRAPHENE GROWN FROM NITROGEN-SEEDED SIC

Last chapter presented detailed research that leads to a greater understanding of the interaction between two fundamental elements: silicon and carbon (graphene). With regard to the fundamental element, nitrogen, which is the most abundant pure element on earth, also plays a significant role in scientific research nowadays. This chapter will reveal how a small amount of nitrogen is able to transform epitaxial graphene.

4.1 Semiconducting Graphene with Wide Band-gap Grown from Nitrogen-seeded SiC

The goal of developing all-carbon electronics requires the ability to dope graphene and convert it between metallic and wide band-gap semiconducting forms. While doping graphene by adsorbates or more elaborate chemical means has made rapid progress [46, 64, 65, 66, 67, 68, 69], opening a band-gap in graphene has been problematic. Two routes to wide-band-gap semiconducting graphene have been pioneered: electron confinement and chemical functionalization. Electron confinement in lithographically patterned narrow graphene ribbons has been plagued by lithographic limits and edge disorder [70, 71, 72, 73], although recent results from sidewall grown graphene ribbon are showing new progress that could lead to band-gaps larger than 0.6 eV [74, 75]. Functionalized graphene band-gaps can be produced by imposing a periodic potential in the graphene lattice through ordered adsorbates [76, 77] or ordered impurities replacing carbon atoms [78].

This section demonstrates a novel approach to band-gap engineering in graphene

using a nitrogen seeded SiC surface. Rather than using chemical vapor deposition (CVD) or plasma techniques to dope graphene by post seeding the films with nitrogen [67, 68, 69, 79], we show that a submonolayer concentration of nitrogen adsorbed on SiC, prior to graphene growth, causes a large band-gap to open in the subsequently grown continuous graphene sheets. Using XPS, STM, and ARPES, we show that a 0.2ML concentrations (measured in a real density of the SiC $(000\bar{1})$ surface: $2.1\times 10^{14}\text{cm}^{-2}$) of nitrogen bonded to SiC at the graphene-SiC interface leads to a 0.7 eV semiconducting form of graphene.

The band-gap is not a result of chemical functionalization since the concentrations used in these studies are expected to have little effect on the band structure of graphene [80, 78]. Instead, STM topographs and dI/dV images showing that the graphene is buckled into folds with 1-2nm radii of curvature suggest two possible origins for the gap: either a quasi-periodic strain [114] or electron localization in the 1-2 nm wide buckled ribbons [83].

4.1.1 N-graphene Growth

The substrates used in this study were n-doped (nitrogen) 4H-SiC. To produce the initial nitrogen surface layers, SiC substrates were loaded into a 900 °C furnace under a 500 sccm Ar flow and heated to 1175 °C over a one hour ramp. The samples were then kept at 1175 °C for two hours with 500 sccm NO flow [125]. Nitrogen atoms attached to both the Si-face and the C-face (see Figure 28). After that, samples were cooled down to 900 °C under a 500 sccm Ar flow and unloaded from the furnace. The surface silicon dioxide grown through this annealing process was removed by diluted hydrofluoric acid (HF) or buffered oxide etch (BOE) before graphene growth.

During the graphene growth process, the stability of nitrogen at the SiC surface is very important, because we do not want the nitrogen to desorb before the graphene has grown. To investigate the desorbing of the nitrogen, we performed series of

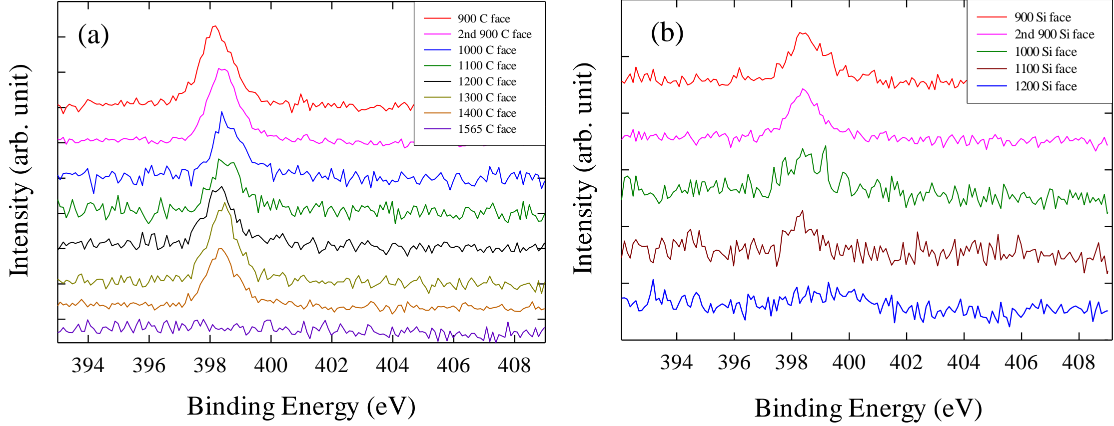

Figure 28: Nitrogen 1s core-level spectra after annealing at different temperatures on (a) C-face from 900 °C to 1565 °C and (b) Si-face from 900 °C to 1200 °C. The photon energy is 1486 eV.

annealing experiments on both faces of nitrogen-seeded SiC at various high temperatures (see Figure 28). On C-face SiC, the surface nitrogen coverage was stable up to 1400 °C. However, once the sample was heated to the usual graphene growth temperature of 1565 °C, no nitrogen signal was observed in the XPS spectrum. The nitrogen stability on the Si-face was even worse. The nitrogen peak almost disappeared by 1200 °C. In fact, graphene is able to grow at temperatures of as low as 1100 °C on C-face SiC [97]. The best graphene is grown at higher temperatures ($\sim$ 1550 °C) in a near equilibrium silicon flux that is sustained in the CCS furnace [116]. In order to maintain a significant nitrogen concentration during growth while maintaining as high a growth temperature as possible, the leak hole size of the crucible was adjusted from $1mm$ to $2mm$. A slightly larger size of the leak hole is able to lower the graphene growth temperature to 1450 °C because of lower silicon vapor pressure.

Nitrogen coverage as a function of temperature for C-face SiC is shown in Figure 29. The oxygen signal is a native oxide that formed each time the sample is annealed in the furnace and taken in air to the XPS. Once the sample is heated to graphene growth temperature, the oxide will evaporate so that no oxygen remains on the surface. This is also demonstrated in Figure 30 that compares C 1s spectra between normal C-face

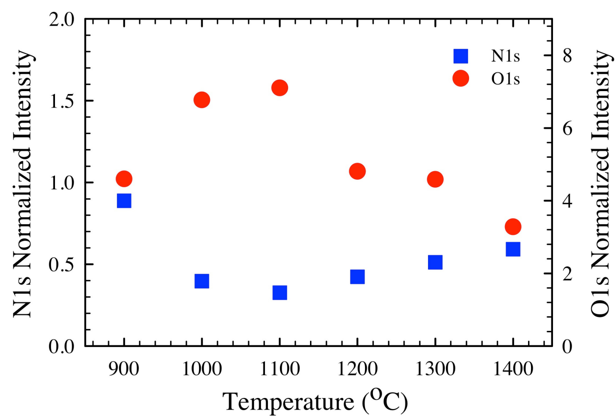

Figure 29: N 1s and O 1s XPS intensity vs temperature for a SiC C-face nitrogen-seeded surface.

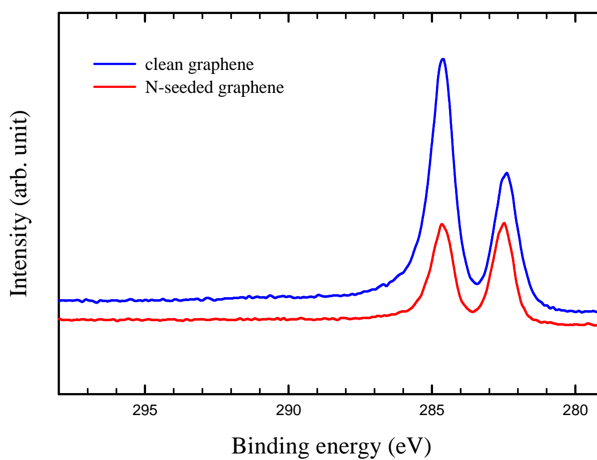

Figure 30: C 1s spectrum from clean multi-layer C-face graphene and 3-layer N-seeded graphene with $h\nu = 1486$ eV.

graphene and nitrogen-seeded graphene. Once the epitaxial graphene samples are removed from vacuum and transported in air, neither carbon nor silicon oxide forms. These graphene films are extremely stable to oxide formation.

Figure 30 also shows very little difference between the C 1s spectra of pristine graphene grown on C-face SiC and graphene grown from nitrogen-seeded SiC. There is less than 0.1 eV between the C 1s peak for the clean and nitrogen-seeded graphene, which indicates a negligible change of surface Schottky barrier height when nitrogen is added.

Figure 31 is a more detailed XPS analysis before and after graphene growth on nitrogen-seeded SiC. After nitrogen was seeded onto SiC, there is a strong N 1s peak at $398.9eV$ in Figure 31(a) with full width at half maximum (FWHM)$= 1.4eV$. The N 1s peak binding energy and broad width are consistent with a range of calculated sites that are likely resulting from two- and three-coordinated nitrogen in substitutional carbon sites in the graphene lattice as well as nitrogen bonded to interfacial silicon and carbon atoms [84]. The nitrogen coverage, N_N, is estimated from the ratio of the N 1s to Si 2p intensities

$$N_N = \frac{I_N}{I_{Si}} \frac{\sigma_{Si}}{\sigma_N} n_{Si} \lambda \tag{12}$$

where I_N and I_{Si} are the N 1s and Si 2p XPS intensities, σ_N and σ_{Si} are the photoionization cross sections of N and Si [126, 127]. $n_{Si} = 4.8 \times 10^{22}/\mathrm{cm}^3$ is atomic density of Si in SiC. For this work, we use a mean free path in SiC of $\lambda = 2.2$nm at $h\nu = 1486$ eV.

In these studies the integrated N 1s XPS intensity corresponds to a starting nitrogen concentration of $\sim$0.3ML ($\sim 3.9 \times 10^{14}\mathrm{cm}^{-2}$ of N on the 4H-SiC C-face. The XPS data of Figure 31 shows that a large fraction of this N remains at the SiC-graphene interface after graphene growth at 1450 °C. We suggest a model where a portion of the remaining nitrogen is not incorporated into the graphene but instead pins the

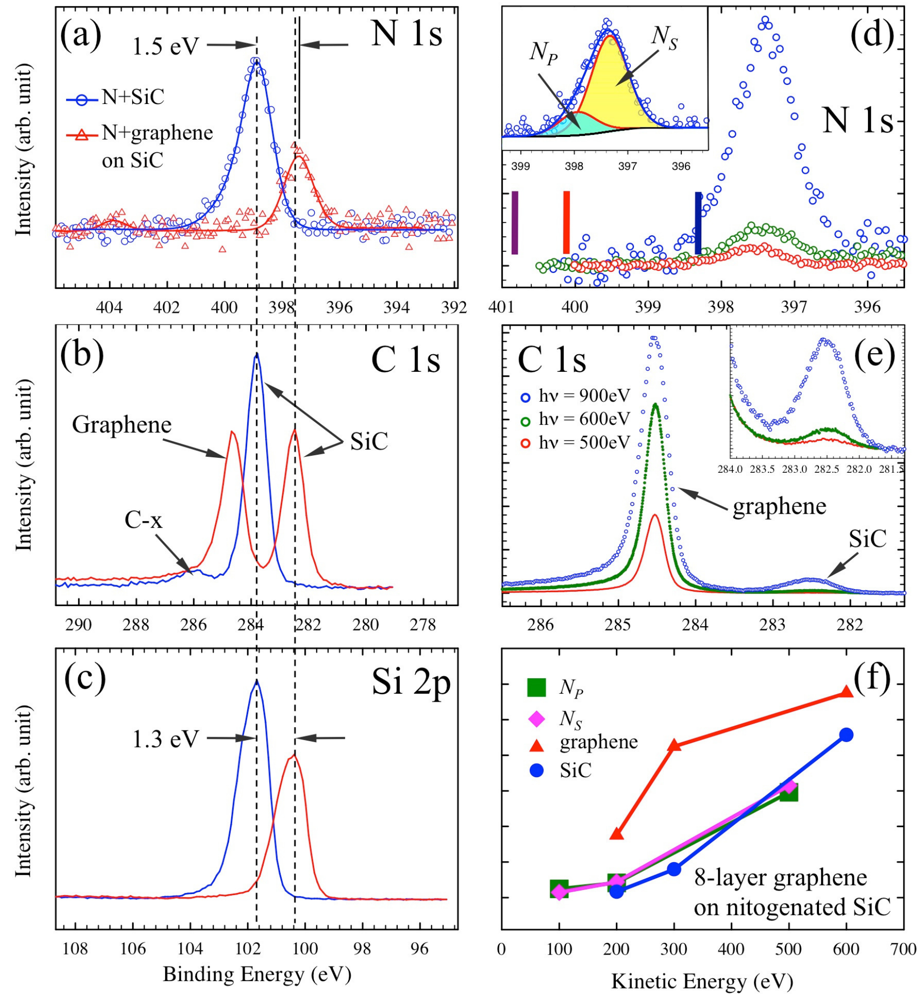

Figure 31: (a)-(c) XPS spectra from SiC C-face before and after growth of a 3-layer graphene film. (a) N 1s, (b) C 1s, and (c) Si 2p ($h\nu = 1486$ eV). A 1.3 eV shift after graphene forms is shown (dashed line). (d) and (e) XPS spectra for an 8-layer graphene film grown from the nitrogen-seeded C-face SiC using photon energies of 500, 600, and 900 eV. The intensities have been normalized to the graphene C 1s peak. (d) N 1s spectra at the same photon energies as (e). Insert shows the 2-component fit to the N 1s peak. The purple, red and blue bars in (d) mark the expected peak positions of pyrrolic, graphitic and pyridinic N-inclusions in graphene, respectively [69, 79]. (e) XPS of the C 1s spectrum for the same photon energies in (d). Insert in (e) shows the SiC portion of the C 1s XPS spectra. (f) The trend in photoelectron intensity versus photoelectron KE energy from an 8-layer graphene sample for the SiC-C 1s, graphene C 1s, and the two N 1s XPS peaks. Absolute intensities have been scaled by arbitrary factors to highlight the energy trend for each peak.

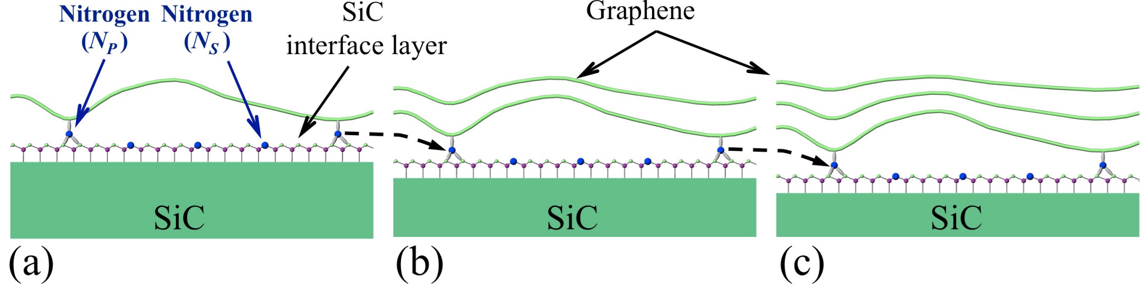

Figure 32: Schematics showing how graphene layers grow from nitrogen-seeded SiC. (a) Most of the nitrogen, N_S, is bonded to Si atoms (magenta) in carbons sites. The remaining interfacial nitrogen, N_P, is bonded to both the SiC carbon atoms (green) and the graphene, pinning it to the SiC. As the graphene grows and the SiC recedes, nitrogen remains at the SiC interface. (b) and (c) both show that the buckling amplitude in layers farther from the surface is reduced as strain is relieved.

graphene to the SiC to produce buckled semiconducting graphene.

After growth, the graphene C 1s peak develops at 284.5 eV (see Figure 31(b)). The C-x peak at 286 eV is from "adventitious carbon" contamination in the initial surface [85]. No oxides (C-O or Si-O) are measurable once the graphene has formed. We note that both the SiC-Si 2p and SiC-C 1s peaks shift 1.3 eV to lower BE once the graphene forms (see Figure 31(a) and (c)), consistent with the known band bending on graphitized C-face SiC [87, 88]. The C 1s peak is essentially identical to clean C-face graphene as discussed in Figure 30. After growth, the N 1s peak is shifted by 1.5 eV to lower BE (a net shift of -0.2 eV) and the total nitrogen concentration, as determined by XPS, reduces to $\sim 2 \times 10^{14}/\text{cm}^2$, ~ 0.2ML. The post growth N 1s peak can be fit with two narrow pseudo-Voight peaks at 398.0 eV and 397.4 eV (with FWHM of 0.8 and 0.9 eV respectively), labeled as N_P and N_S (see the insert in Figure 31(d)). It is important to note that there are no other HBE N 1s peaks in the spectrum that would normally be associated with common nitrogen incorporation sites in the graphene lattice [69]. In other words, little if any nitrogen is incorporated into the graphene lattice.

The dominant peak at 397.4 eV, labeled as Ns, is usually associated with N-SiC bonds. Specifically, nitrogen in carbon sites bonded to Si atoms at the SiC interface as

shown in Figure 32(a) (see Appendix A) [89]. The weak N_P peak at 398.0 eV ($\sim$25% of the total nitrogen coverage) is in the energy range associated with pyridinic nitrogen sites in graphene [90, 84, 68, 67], but can also be associated with other sp^3 and sp^2 C-N bonds in carbon nitride films [107]. Photon energy-dependent XPS measurements in Figure 31(d),(e), and (f) and STM images described below indicate that N_P is not pyridinic nitrogen but is instead a second C-N compound at the graphene-SiC interface that pins the graphene to the SiC (see Figure 32(a)).

Figures 31(d) and (e) show XPS spectra of N 1s and C 1s at various photon energies. A photon energy of $h\nu = 500$ eV produces photoelectrons with the shortest mean free path of the three photon energies used in these experiments and is therefore the most surface sensitive of the three. In Figure 31(e) the more surface sensitive spectra have the weakest SiC-C 1s, indicating that the SiC spectra is attenuated by the graphene layers above. The N 1s peak is similarly weakest at this energy indicating that most of the nitrogen is at the interface. We also note that the ratio of N_S and N_P peak intensities is independent of photon energy. This is demonstrated in Figure 31(f), where the intensity of two peaks have essentially the same kinetic energy dependence with SiC. These two findings confirm that the N_P peak is associated with a nitrogen site at the SiC-graphene interface and is *not* a pyridinic nitrogen inclusion in graphene.

The XPS results shown in Figure 31(a) make clear that while a significant portion of the nitrogen desorbs during the high temperature (1450 °C) growth, the remaining nitrogen is maintained in a stable concentration of sites at the graphene-SiC interface. This implies that any high energy substitutional nitrogen sites that develop in the growing graphene film are annealed out and remain bonded at more favorable sites at the SiC interface. Assuming a uniform distribution of N_S and N_P sites, the average distance between nitrogen atoms is $\sim$0.9nm for N_S sites and $\sim$1.5nm for N_P sites. A length scale comparable to the N_P average spacing will be seen again in STM results

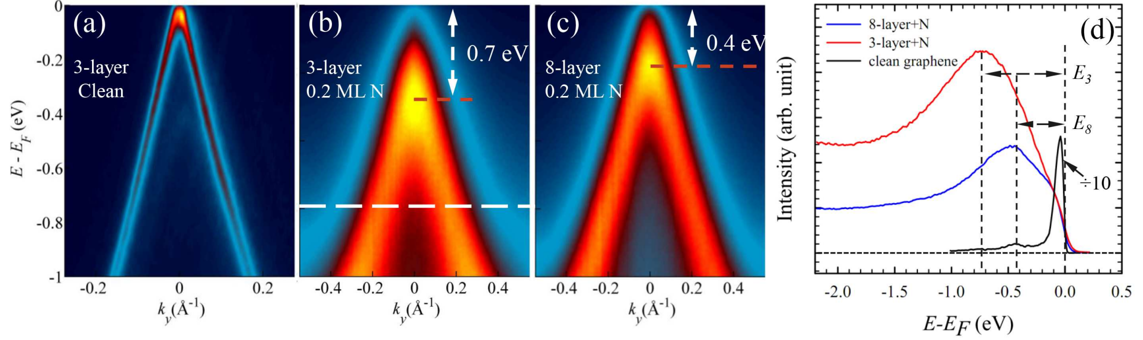

Figure 33: The ARPES band structure taken with $\hbar\omega = 36$ eV near the K-point of (a) clean 3-layer graphene (T=100K), (b) 3-layer graphene with a 0.2ML nitrogen SiC(000$\bar{1}$) surface (T=300K), and (c) 8-layer graphene from a 0.2ML nitrogen SiC(000$\bar{1}$) surface (T=300K). k_y is perpendicular to the ΓK direction. Note the different energy and momentum scales for (b) and (c) compared to (a). (d) Energy distribution curves through the Dirac point in (a), (b) and (c) show the 0.7 eV gap for 3-layer films that reduces to 0.45 eV for 8-layer films. Note that the apparent energy broadening observed near E_F in the nitrogen samples compared to the clean surface, is entirely resulting from the temperature difference between the two measurements that broadens the 300K Fermi-Dirac function.

from these same films and will be important in understanding the band structure of this material.

4.1.2 Band-gap Opening

The interfacial N-preparation method used here causes a band-gap to open in graphene's π bands. We demonstrate this using high resolution ARPES from graphene films taken at the graphene K-point (rotated 30° from the SiC $<10\bar{1}0>$ direction). Figure 33(a) shows the typical band dispersion perpendicular to the ΓK direction at the graphene K-point from a clean C-face 3-layer graphene film. As the ARPES shows, pristine 3-layer C-face graphene consists of linear π-bands (Dirac cones) with little or no doping [115]. The band structure of a graphene film with 0.2ML interface N-content is dramatically different as seen in Figure 33(b) and (c). When interfacial nitrogen is present, a band-gap has developed. Figure 33(d) shows energy distribution curves (EDC) through the K-point at $k_y = 0$ from (a), (b), and (c). Unlike

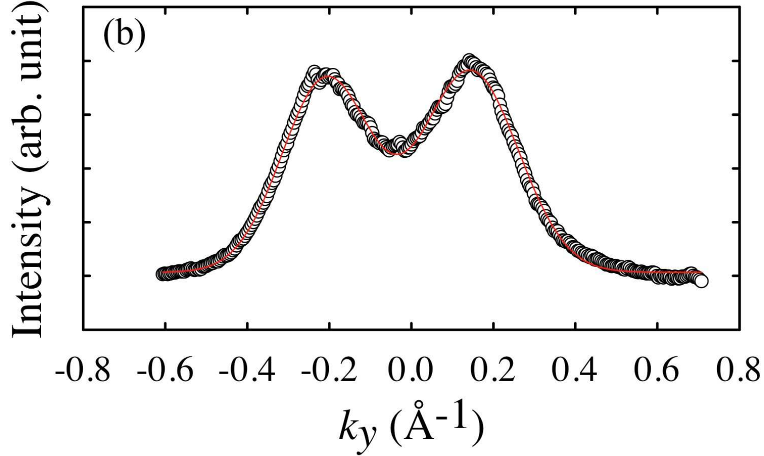

Figure 34: (MDC made at BE=-1.5 eV from the Dirac cone in Figure 33(a). A double Gaussian peak fit (red line) is shown.

pristine graphene, the peak in the EDCs from the nitrogen-seeded samples are shifted to HBEs indicating a valence band maximum corresponding to an energy gap. Figure 33(d) shows that the 3-layer N-seeded sample has a 0.7 eV gap (depending on the position of the conduction band minimum), while the 8-layer film has a smaller 0.45 eV gap (a 4-layer film, not shown, confirms this trend). The C 1s spectra from clean and N-seeded samples in Figure 30 show that the valence band spectra cannot be resulting from an energy shift caused by band bending changes in different samples. We also note that the effective velocity, $\tilde{v}$, derived from a linear approximation to $E(k)$, is reduced compared to v_F, consistent with the opening of a band gap. Within a small k_y-range around the Dirac point ($\Delta k_y = \pm 0.15\text{Å}^{-1}$), both the 3- and 8-layer samples have the same $\tilde{v}$ within the error imposed by the ARPES broadening ($\tilde{v} = 0.8 \pm 0.05 \times 10^6$m/sec).

Another point of the ARPES image in Figure 33(b) is that a small bump in the clean samples's EDC occurs at a binding energy of $\sim$0.5eV. This bump is a result of the Dirac cone of another rotated graphene sheet in the layer below (see for example in references [93] and [115]).

The π-bands are significantly broadened in k_y relative to the instrument limited

graphene grown on pristine graphene. The momentum broadening is seen more clearly in momentum distribution curves (MDC) taken at $E - E_F = -1.5$ eV in Figure 34. The MDC was fitted to two Gaussian peaks for the the π and π^* bands. The width was found to be $\Delta k \sim 0.25\text{Å}^{-1}$. A large part of the EDC energy broadening and the momentum broadening is because of the corrugation of the graphene surface (the corrugation is demonstrated in STM results presented below) [94, 95]. Small modulations in the local graphene height cause a local angular variation in the surface normal. Since the surface normal determines the orientation of the graphene Brillouin zone, the corrugated surface leads to local k_x and k_y shifts relative to a flat surface K-point. This leads to an ARPES image that is an area average of a distribution of parabolic cuts through Dirac cones from locally tilted graphene resulting in an E- and k-broadened spectra. While this explains part of the broad intensity distribution between the valence band maximum and E_F. A more detailed STM analysis suggests how the gap forms and an additional broadening of the EDCs.

STM images of the nitrogenated graphene show that the films are not flat like typical C-face graphene films [54]. Figure 35(a) shows the highly buckled topography. A close up view of a buckled regions in Figure 35(b) shows that the fold is made of intact graphene. Note that there are no indications of nitrogen inclusions like those seen in CVD and plasma created nitrogen [96, 79]. The folds are $\sim$ 1nm (no more than 2nm) high and 2-4nm wide giving a radius of curvature of 1-2nm. These folds meander and can extend up to 25nm but are typically 5nm long. Figure 35(c) shows an STM topographic image of a region with several folds. A dI/dV image in Figure 35(d) of a small region between folds confirms that the graphene sheet is continuous. We note that these foldings are not a property of epitaxial graphene. The root mean square (RMS) roughness is less than 0.005nm for graphene films without nitrogen [97].

It is important to point out that the 2-4nm width of these folds is consistent with

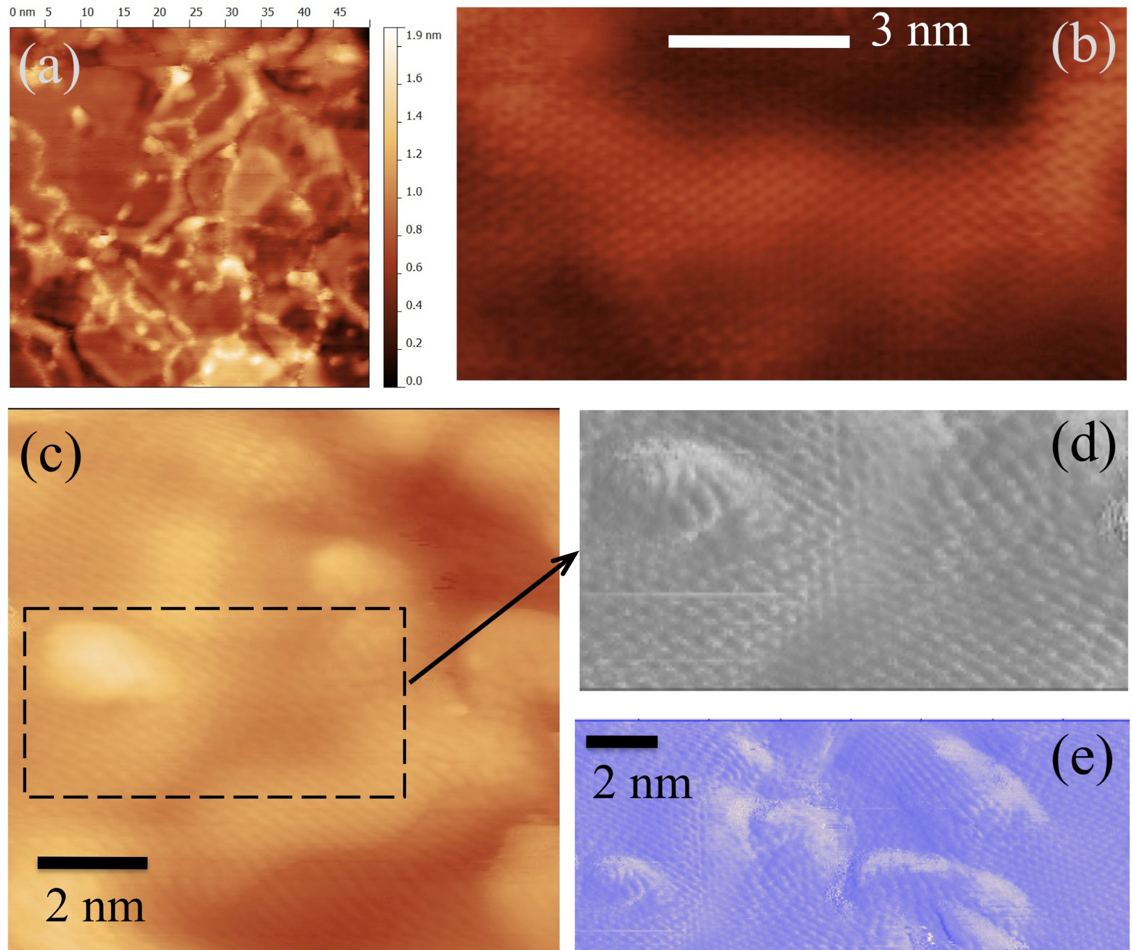

Figure 35: (a) $50 \times 50\text{nm}^2$ STM image of a 3-layer graphene film grown from a 0.2ML nitrogen-seeded C-face SiC (bias voltage, $V_B = 0.1$V). The image shows a pattern of folds. (b) A topographic image of a fold showing the graphene lattice ($V_B = 0.1$V). (c) A 10×10nm view of the graphene folds. (d) A magnified dI/dV images of folded graphene showing that the graphene is continuous over the folds and in the valleys. (e) A dI/dV image of a region in (c). The image shows that the tops of the folds are bright in the dI/dV image indicating a high density of states.

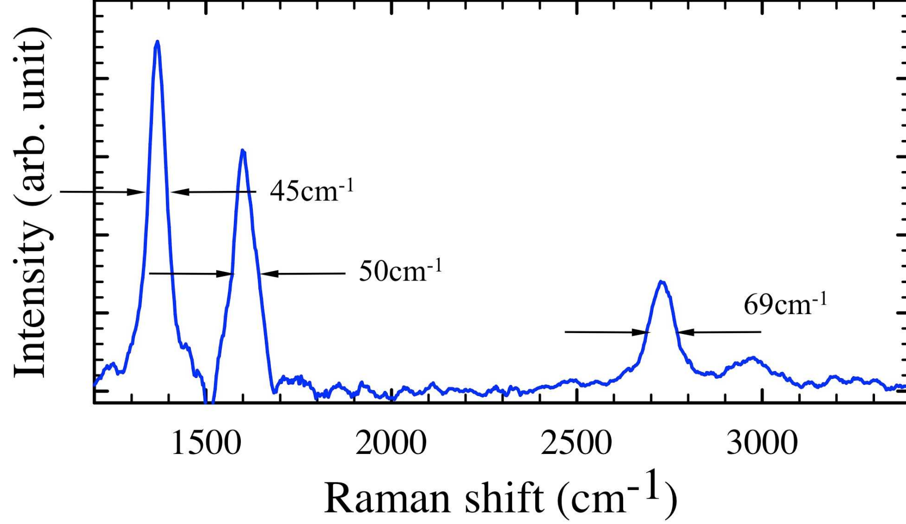

Figure 36: The Raman spectrum of a 3-layer graphene film with 7 at% nitrogen as determined by XPS and ellipsometry. The SiC background signal has been subtracted.

the 0.25Å^{-1} Δk broadening of the ARPES spectrum. In ARPES, $\Delta k \sim 2\pi/L$ where L is the average coherent domain size. This allows us to estimate $L \sim 2.5$nm from the ARPES broadening. In addition to the scale of the finite size domains measured by ARPES, the mean separation between N_P nitrogen atoms, determined by XPS, is 1.5nm; only slightly smaller than the width of the folds determined by STM.

That fact that three different techniques measure similar length scales is not a coincidence. A model consistent with these results is shown in Figure 32. During the high temperature growth, Si evaporates leaving a carbon rich surface with N-impurities. As the graphene layer crystalizes from this film at high temperature, N atoms in high energy interstitial graphene sites are expelled from the growing graphene. Some of these nitrogen desorb while the others re-bind to the SiC as either N_S or N_P nitrogen (see Figure 32(a)). The interfacial nitrogen atoms (N_P) act as pinning sites that lock the graphene to the SiC. This is supported by a large D-peak in Figure 36 Raman spectra consistent with a significant concentration of sp^3-like bonds that would be associated with graphene-N bonds. These sp^3 bonded C-N-SiC sites constrain the graphene to a length scale related to the starting nitrogen

concentration. Since the N-constrained graphene is no longer commensurate with the SiC, a strain develops in the film that forces the graphene to buckle. These folds are similar to the differential thermal expansion induced strain pleats normally observed in epitaxial graphene [97]. Although the folds in this study are much smaller in both length and width. Unlike the pleats, the length scale between folds is set by the strain field induced by the interfacial nitrogen concentration. As the next graphene layer forms, Si evaporation causes the SiC interface to recede along with the interfacial nitrogen as shown in Figure 32(b) and (c). As each new graphene layer forms the process is repeated leaving a stack of π-bonded graphene layers with only the last layer nitrogen bonded to the SiC. The buckling period remains determined by the nitrogen concentration and not the number of layers. As Figure 32 shows, the buckling amplitude is expected to reduce in layers further from the SiC as previously shown by STM [98].

It is these folds that are responsible for the energy gap and not nitrogen impurities in the graphene. Because of the short electron mean free path, the ARPES only measures the graphene band structure in the top 2-3 layers where the XPS shows no measurable nitrogen concentration, indicating that the measured band gap must be related to the graphene folds. The size of the ARPES gap and its dependence on the layer thickness point to a finite size effect gap caused by either strain confined domain boundaries or by a quasi periodic strain field.

The boundary between folds is a highly strained region of graphene that could confine the graphene wave functions between folds. The confinement band-gap expected for a graphene ribbon with width $w = 1\text{–}2$ nm is $E_g \sim 1\text{eV-nm}/w = 1.0\text{–}0.5$ eV [83, 99], close to the value measured. The fact that a distribution of confined folds are part of a continuous sheet of graphene would also explain the ARPES intensity seen within the gap. A model of bent graphene confined by flat graphene sheets predicts a significant density of states (DOS) in the gap because of boundary resonant states

[74]. The finite size model also explains the smaller gap in thicker films even though the domain size is the same. As the number of layer increases, the amplitude of the buckles reduces, thus reducing the strain at the bends. This makes the confinement boundary less well defined; effectively increasing the confined region and reducing the gap. Because of the fold width distribution, the area-averaged ARPES would have a distribution of band gaps resulting in an increased intensity between the top of the valance band and E_F as observed.

Periodic strain fields are also expected to open a band-gap [114]. Figure 35(e) shows a dI/dV image of several fold ridges that show the typical increased DOS predicted for strained graphene [100] and observed in STM on graphene nano-bubbles [101]. While the nitrogen induced folds are not strictly periodic, the folds have an average separation of about 2-4 nm. This is a very small period that has the potential to open a large gap. Whether strain or electron confinement (or both) are responsible for the observed gap remains to be determined.

4.1.3 Strain Analysis of N-graphene

In order to understand the strain effect on the nitrogen-seeded graphene, X-ray diffraction experiments were performed at the Surfaces and Interfaces X-ray Scattering (SIXS) beamline at SOLEIL synchrotron using an X-ray beam of energy of 15.54keV.

To analyze the strain in the N-Gr system, we used surface X-ray scattering (SXRD) method. The graphene diffraction rods can be either shifted or broadened by strain in a manner that depends on the type of strain in the system. Regions of uniaxial strain will give rise to new diffraction rods that are shifted by $\Delta q_{\|} n$ relative to the diffraction rods from the unstrained region. The amount of shift depends linearly on the diffraction order n defined by $n = q/a_G^*$, where a_G^* is the graphene reciprocal lattice constant. If different regions have different strains, there will be a broadening of the strain shifted peak where the broadening is also linearly proportional to n.

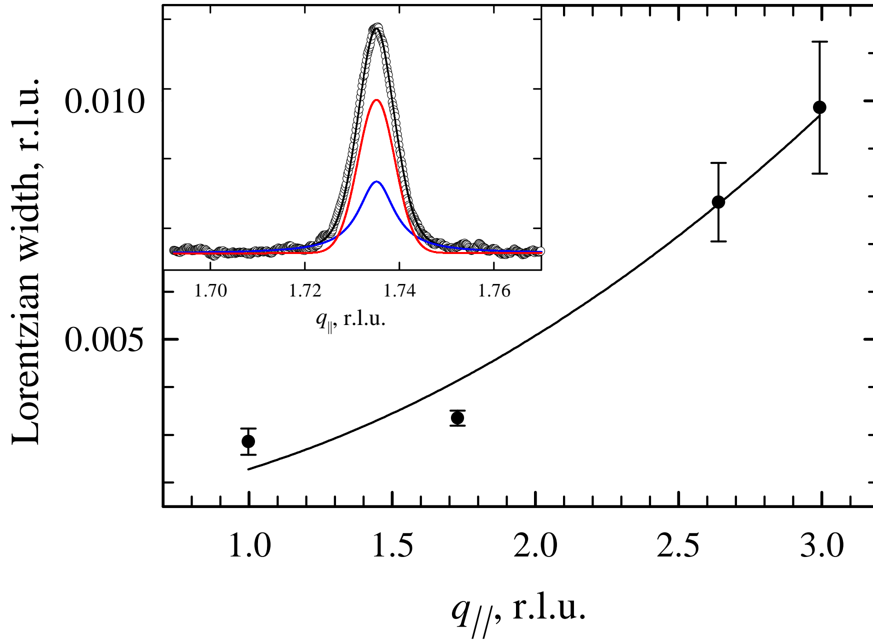

Figure 37: Insert shows a radial scan ($q_{\|} = (h+\Delta, k+\Delta, \ell)_{\mathrm{G}}$) through the graphene $(1, 1, \ell)_{\mathrm{G}}$ rod ($q_z = 2\pi\ell/c_{\mathrm{G}}$ for $\ell = 0.2$) for N-Gr graphene film. The pseudo-Voight fit (black) using a Lorentzian (blue) and Gaussian (red) is shown. The Lorentzian Half widths for the $(01)_{\mathrm{G}}$, $(11)_{\mathrm{G}}$, $(12)_{\mathrm{G}}$, and $(03)_{\mathrm{G}}$ rods are plotted as a function of their radial $q_{\|}$ values. Solid line shows a fit to the data using $\beta_s = \beta_o + Cn^2$ fit to the data where β_o and C are fit parameters.

However, the measure N-Gr diffraction rods do not behave according to the uniaxial strain model. To show this, we have fit the N-Gr diffraction rods to a pseudo-Voight line shape where the lorentzian width scales like n^2 instead of n (see Figure 37). The n^2 behavior is the q-dependent broadening from that a random strain field (see the Appendix B). For a random strain field, the FWHM of the pseudo-Voight Lorentzian (Γ_L) and Gaussian (Γ_G) are given by

$$\Gamma_L = (a_G^*)^2 n^2 \epsilon_s^2 L, \text{ and } \Gamma_G = 4\sqrt{\pi ln2}/L \tag{13}$$

where $L = Na_G$ is average graphene domain size and ϵ_s^2 is the mean squared strain $< \Delta L^2 > / L^2$.

$$\frac{\Gamma_L}{2\pi a_G^*} = n^2 \epsilon_0^2 \tag{14}$$

$$\epsilon_o = \frac{< \Delta a^2 >}{a} \tag{15}$$

From fits up to 4 diffraction orders, the average domain size is found to be $22nm \pm 5nm$, from the Gaussian component width, and the RMS strain $\epsilon_{rms} = \sqrt{\epsilon_o^2}$ is $1.7 \pm 0.1\%$. The value for L is consistent with the large flat plateaus observed in STM. While there is overall agreement of the SXRD line shapes with the simple random model there are an important difference. The ratio of the gaussian and lorentzian peak $(1 - \eta)/\eta$ is not an independent parameter. Within the model this ratio depends on the widths of the two line (see Equations 19a and 19b). However, when η is allowed to vary independent of Γ_L and Γ_D, better fits to the data are achieved. The value of η can be $\pm 40\%$ of the expected value based on the one-dimensional model.

It is worth noting that the measured graphene lattice constant for N-Gr is 2.457 ± 0.002Å. This is the mean value of theoretical graphene and graphite. In pristine C-face graphene, diffraction rods for both lattice constants are found because of variations

in the interlayer stacking [51]. We are not able to resolve these two rods in these experiments due to the finite size broadening from the smaller domain size of the N-Gr films.

To summarize this section, a partial nitrogen monolayer, pre-grown on the C-face SiC surface, is shown to be able to form an undulating graphene layer with a band-gap $\sim$0.7 eV. The nitrogen binds the growing graphene to the SiC interface forming 1-2nm high ridges in the graphene. There is no nitrogen intercalation between graphene sheets nor is there evidence of nitrogen inclusions that can reduce graphene's mobility [102, 103]. XRD measurement shows this nitrogen-seeded graphene has the random strain about 1.7%. Because the initial nitrogen-carbon bond is stable to very high temperatures, the pre-grown layer can be patterned to produce locally strained graphene, which will be shown in the next section. This semiconducting form of graphene would then be seamlessly connected to metallic graphene grown from the non nitrogen-seeded SiC. It offers a potential way to produce all graphene semiconductor-metal junctions.

4.2 Pattern Induced Ordering of Semiconducting Graphene Ribbons Grown from Nitrogen-seeded SiC

In the last section, we have discussed the wide band gap semiconducting form of graphene. This entirely new form of graphene can be produced by growing a buckled graphene sheet from a SiC $(000\bar{1})$ surface pre-seeded with nitrogen. However, it is still not ideal for electronics production because of several reasons. First, in Figure 33(b) and (c), there is still photoelectron intensities between the Fermi level and valence band maximum. Thus the band gap observed is not a sharp gap. It is the sum-up of many different graphene regions with different gap sizes, even non-gap graphene. STM images from Figure 35 also show that the surface is composed of both buckled graphene and flat graphene. Thus the next step is to localize those strained structures and make a controlled junction with sharp edge between flat graphene (no band gap) and buckled graphene (with a band gap).

Another problem of N-Gr is also the typical issue for C-face graphene: large thickness variance. As introduced in Chapter II, graphene grown from the C-face SiC has exceptional mobility because of its rotational stacking [40, 97]. It has recently been used in a hybrid SiC-graphene Schottky barrier transistor with exceptional on/off ratios (10^6) and relatively high channel mobility [110]. Furthermore, Field-effect transistors (FET) built from monolayer C-face graphene have shown the highest operating frequencies of any graphene-based devices [111]. Nevertheless, controlling C-face graphene's thickness has been a problem. The thickness of graphene can be measured by LEEM reflectivity as mentioned in the last chapter in Figure 14(a). For the sample in Figure 14(a), the thickness of the graphene film varies from 2 to 8 layers. A similar variance is also observed in the N-graphene and will be discussed below. Therefore, solving the large thickness variance problem will have effects on both N-Gr and normal C-face graphene performance.

In this section, a solution to both problems is presented; pre-patterning the

nitrogen-seeded SiC surface into trenches. While N-Gr and flat graphene are shown separated by patterning, results indicate that the graphene growth from pre-patterned ribbons leads to three key improvements in the graphene film: (i) layer thickness control, (ii) improved rotational ordering, and (iii) a spatially uniform band structure. While the ribbon widths used in this study are too large to effect strain gradients in this system (400 nm $\leq w \leq$ 500 nm), the distance between the step edges defining the ribbons is on the order of the distance between random vertical tubes that normally nucleate in C-face graphene films. We show that the ribbon structure inhibits the formation of the random vertical tubes (see Ref. [115]) with the result that graphene thickness uniformity is dramatically improved, presumably because of spatially controlled Si sublimation at the patterned step edges. Using a combination of LEEM, XPEEM and μ-ARPES, we characterize both the topographical structure and band structure of N-Gr ribbon arrays. We show that the graphene's structural properties are substantially improved within the confined ribbons when compared to 2D graphene. In fact, the thickness uniformity is improved to the point of single layer control. The results presented in this study are not only the first to use patterned ribbons to control growth, they are the only successful attempt to improve C-face graphene uniformity. The improved structural order is reflected in the electronic structure of the N-Gr ribbons, allowing more detailed measurements of the electronic properties of these films.

4.2.1 N-graphene Ribbon Structure

The nitrogen-seeded SiC sample was prepared in the same way as introduced in the previous section. Then the SiC surface was patterned using E-beam lithography (E-BL) and reactive ion etch (RIE) to remove nitrogen in stripes (referred to as trenches). We studied both 500 nm and 400 nm wide ribbons. The etch depth of a trench is $\sim$1 nm in these experiments. After patterning, the sample was heated to 1450 °C for 5

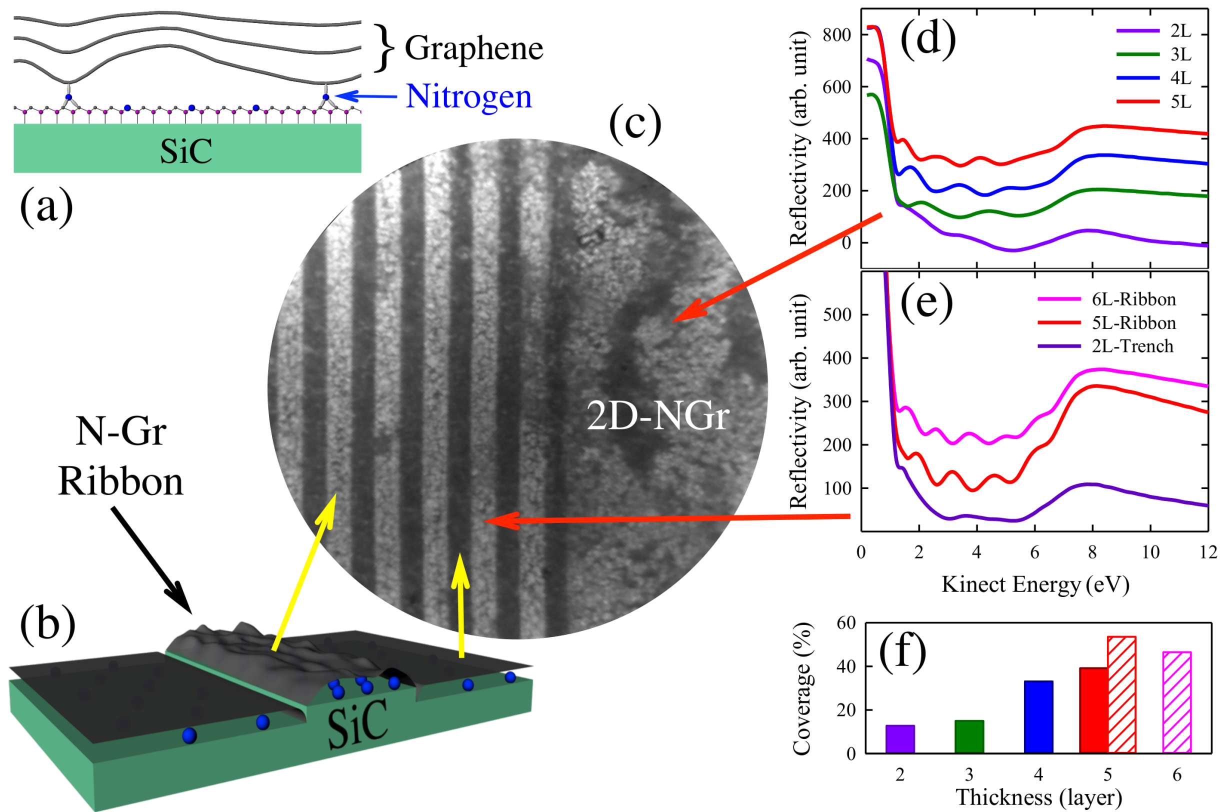

Figure 38: (a) Schematic model of the buckled N-Gr caused by nitrogen pinning of the first graphene layer to the SiC. (b) Schematic of the N-Gr ribbons showing highly strained graphene above a nitrogen interface layer on the SiC. Nitrogen is shown in blue. (c) 10 μm FOV LEEM image of a N-Gr ribbon array next to a 2D N-Gr area ($E = 8.6$ eV). The ribbon width is $w = 500$ nm and the pitch is $p = 1$ μm. (d) LEEM reflectivity spectrum from different regions in the 2D area of the sample with different numbers of graphene layers. The curves are shifted vertically for clarity. (e) LEEM reflectivity curves from the N-Gr ribbons and the trenches between ribbons. (f) A histogram of the relative coverage of different graphene thicknesses in the 2D area (solid bars) and in the ribbons (hatched bars).

minutes in a closed radio-frequency induction furnace using the CCS method to form graphene. It is known from previous studies that the nitrogen bonding between the first graphene layer and the SiC causes the graphene to buckle (see Figure 38(a)). We will also show later in this section that most of the nitrogen remains on top of the ribbons after graphene growth, as shown schematically in Figure 38(b).

Figure 38(c) shows a 10 μm FOV LEEM image of the N-Gr array grown from a patterned nitrogen-seeded SiC surface. The N-Gr ribbons are shown adjacent to a large un-patterned 2D graphene area. The trenches appear dark in this image. Figure 38(c) shows that the boundary of the shallow etched trenches remain sharp after graphene growth. It is important to note that the LEEM contrast is not because of the height differences of trenches and ribbons, but instead results from a graphene thickness change at the boundary (see below). While we cannot tell if the initial 1 nm steps remain after the SiC is consumed during graphene growth, Figure 38(b) clearly demonstrates that the ribbon pattern remains intact.

The first key observation about growth on patterned N-Gr substrates is that the graphene thickness is more uniform on the ribbon area than on the 2D graphene areas of the same C-face SiC surface. In fact, the uniformity becomes similar to that achievable for graphene grown on the Si-face SiC [117]. Figure 38(c) shows a LEEM image of both a ribbon patterned area and a standard 2D N-Gr film. While there are large contrast variations in the 2D N-Gr graphene regions, the contrast along the N-Gr ribbons is very uniform. The contrast variations on the 2D area are because of graphene thickness changes typical in C-face graphene growth [118]. The extent of the thickness variation can be measured using LEEM reflectivity as mentioned in previous chapter. The oscillations in LEEM reflectivity are because of the interference of the incoming electrons with the electrons that are reflected from the SiC-graphene interface (for details on LEEM reflectivity from graphene, see reference [119]).The number of graphene layers is simply determined by counting the

number of minima in a LEEM reflectivity spectrum between 0-10 eV [119]. In the 2D area (see Figure 38(d)), the number of minima in the LEEM reflectivity spectra show that the graphene thickness varies from 2 to 5 layers (a variance of ∼40% about the 3.5 layer average), typical for C-face graphene. In contrast, Figure 38(e) shows that the graphene on top of the nitrogen-seeded ribbons has a smaller thickness variation, varying by only one layer (∼9%) over the entire 10 μm FOV. Note that the graphene is thicker ($< N >\sim$5.5 layers) on the ribbons compared to the 2D area. A comparison of the distribution of layer thickness for the ribbons and the 2D area is summarized in the thickness histogram in Figure 38(f). The observed film uniformity on the ribbons represents a substantial advance in C-face graphene growth.

As determined from the LEEM reflectivity oscillations, the graphene thickness within the trenches is considerably less than that of the ribbons (∼ 2-layers). The thickness variation between trench and ribbon areas is also confirmed by the laterally-resolved C 1s photoemission spectra. Figure 39(a) shows the C 1s spectrum from both the N-Gr ribbons and the trenches. The C 1s spectrum in the trench region is typical of a thin C-face graphene film, showing a graphene peak and a relatively large SiC-C 1s peak [88]. On the ribbons, the SiC-C 1s peak is smaller because the SiC-C 1s photoelectrons are attenuated as they pass through the thicker graphene film on the ribbon area. The difference in the graphene thickness is more evident in the XPEEM contrast image using the graphene C 1s component (see Figure 39(b)). The N-Gr ribbons appear bright compared to the trench area because of the thicker N-Gr film. The reduced growth in the trenches most likely results from the RIE sputter damage induced in the SiC trenches during patterning. A similar effect is also observed on Si-face graphene growth [120].

Both the thicker growth and the better thickness uniformity on the ribbons are consistent with an earlier model proposed to explain the difference in graphene grown

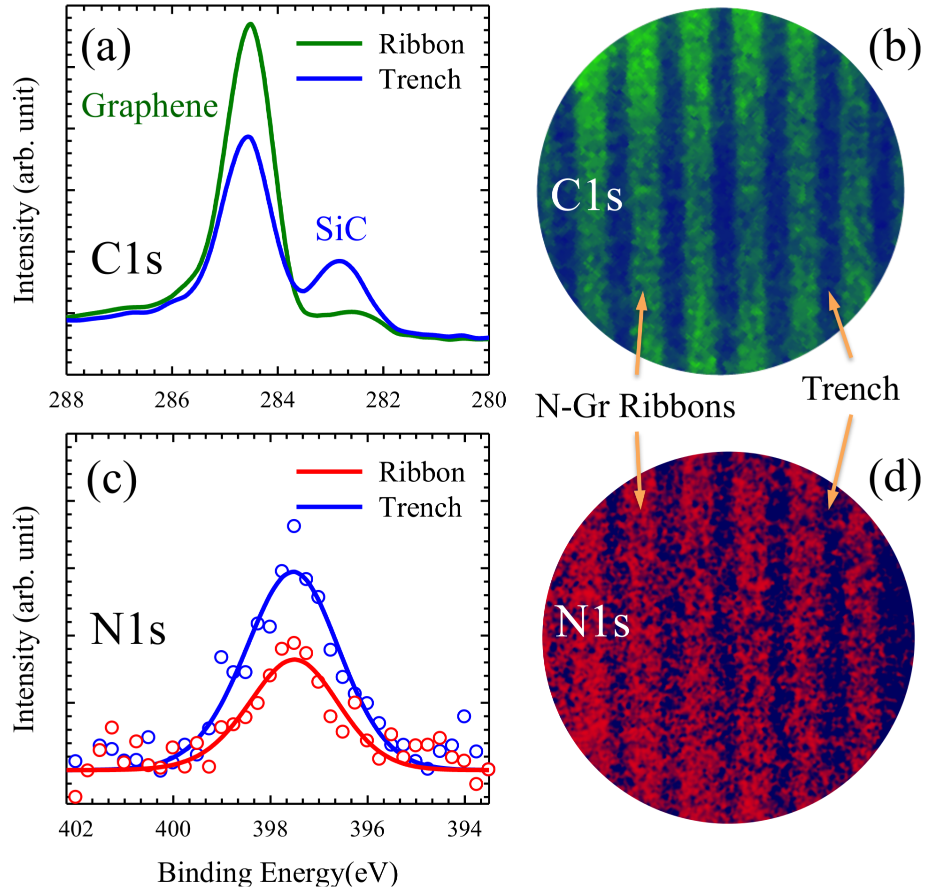

Figure 39: (a) C 1s XPS spectra from the N-Gr ribbons and the trenches ($h\nu = 600$ eV). The ribbon width is $w = 400$ nm and the pitch is $p = 1$ μm. (b) 6.5μm FOV XPEEM image using the graphene C 1s peak at a binding energy (BE) of BE=284.5 eV). Blue is from the trenches. (c) N 1s XPS spectra from N-Gr ribbons and etched trench bottoms ($h\nu = 600$ eV). Background has been subtracted for both N 1s spectra. (d) 6.5 μm Fov XPEEM image of the ribbons using the background subtracted N 1s peak for contrast (BE=397.5 eV). Blue is the N 1s intensity in the trenches.

on Si-face and C-face SiC surfaces [115]. In normal C-face growth the local Si evaporation rate is determined by vertical tubes in the graphene film that extend from the SiC to the surface. The tubes are randomly dispersed across the $(000\bar{1})$ surface. The tubes nucleate more readily on the C-face when the interfacial Si concentration becomes large after the first few graphene layers form. In fact, this property has been used to grow vertical carbon nanotubes from C-face SiC [121]. Si can be easily transported away from the graphene-SiC interface where the vertical tubes form, causing the graphene to grow faster (i.e., thicker) in these areas. The result is a wide range of thickness variations across the surface because of the spatially random formation of these tubes. On the Si-face, these tubes do not form easily and the graphene film thickness is stunted to only a few layers as Si is trapped at the graphene-SiC interface. We suggest that the patterned step edges provide a similar but spatially controlled site for Si evaporation. Based on XPEEM and LEEM images, a typical distance from a tube to a boundary between different graphene thickness regions on the C-face is a few microns [115]. The 500 nm width of the ribbons in these experiments indicates that Si diffusion to the edges will be sufficiently shorter than the known tube separation so that tube formation no longer determines the graphene thickness on the ribbon area. Therefore, unlike the 2D area, the interfacial Si concentration on the ribbons is both low and uniform leading to thicker graphene without the large thickness variations as in the unpatterned areas.

We have also used XPEEM to measure the post-growth nitrogen distribution in the patterned area. The nitrogen 1s photoemission spectra for the trenches and ribbons are shown in Figure 39(c). The distribution of the N 1s signal is displayed in the XPEEM image in Figure 39(d). Although the trenches appear brighter in the N 1s image (more blue), the actual nitrogen distribution can only be determined by accounting for the attenuation of the N 1s signal through the graphene layers above. This is done by comparing the attenuation of the SiC-Si 2p and the N 1s XPS

signals through the known graphene thickness, as claimed in the LEEM reflectivity measurements on both ribbon and trench areas (see Figure 38(e)). By this procedure, we find that the nitrogen in the trenches is half the nitrogen on the ribbons. Prior to these experiments, RIE test on macroscopic areas showed that a 1 nm etch was sufficient to remove the surface nitrogen below XPS detectable limits. Therefore, the presence of nitrogen in the trenches must be a result of diffusion from the ribbon areas during graphene growth.

The second key observation from graphene grown on patterned substrates is the improved rotational epitaxy of the graphene in the ribbon area. Figure 40(a) shows a μ-LEED image from the 2D graphene area. The LEED pattern shows the primary spots corresponding to graphene rotated 30° relative to the SiC $<10\bar{1}0>$ direction (brightest spots in the pattern) plus numerous diffraction patterns from rotationally (non-Bernal) stacked graphene layers typical of C-face growth [53]. The additional spots are primarily from layers below the surface although some are from small rotated domain because of pleats or steps in the film [97, 115]. A dark field (DF) LEEM image, using the graphene $(01)_G$ spot for contrast, shows that the graphene's rotational orientation in the ribbons has become more homogeneous compared to the 2D area (see Figure 40(b)). Also note that the trench area has very little of the normal 30° rotated graphene.

A more detailed look at the difference between graphene on the ribbon and trench areas can be made using dark field photoelectron microscopy (DF-PEEM). Figure 40(c) shows a μ-ARPES image of a constant energy cut through the graphene Brillouin zone (BZ) in the ribbon area. There are two rotated BZs: one from the primary 30° graphene (the six brightest cones), and another from a graphene sheet rotated $\sim 0°$ from the SiC $<10\bar{1}0>$. We note that at the photon energies used in these experiments, the μ-ARPES is sensitive to the top 3 layers because of inelastic electron attenuation. It is therefore difficult to determine if the 0° rotated graphene is in the top graphene

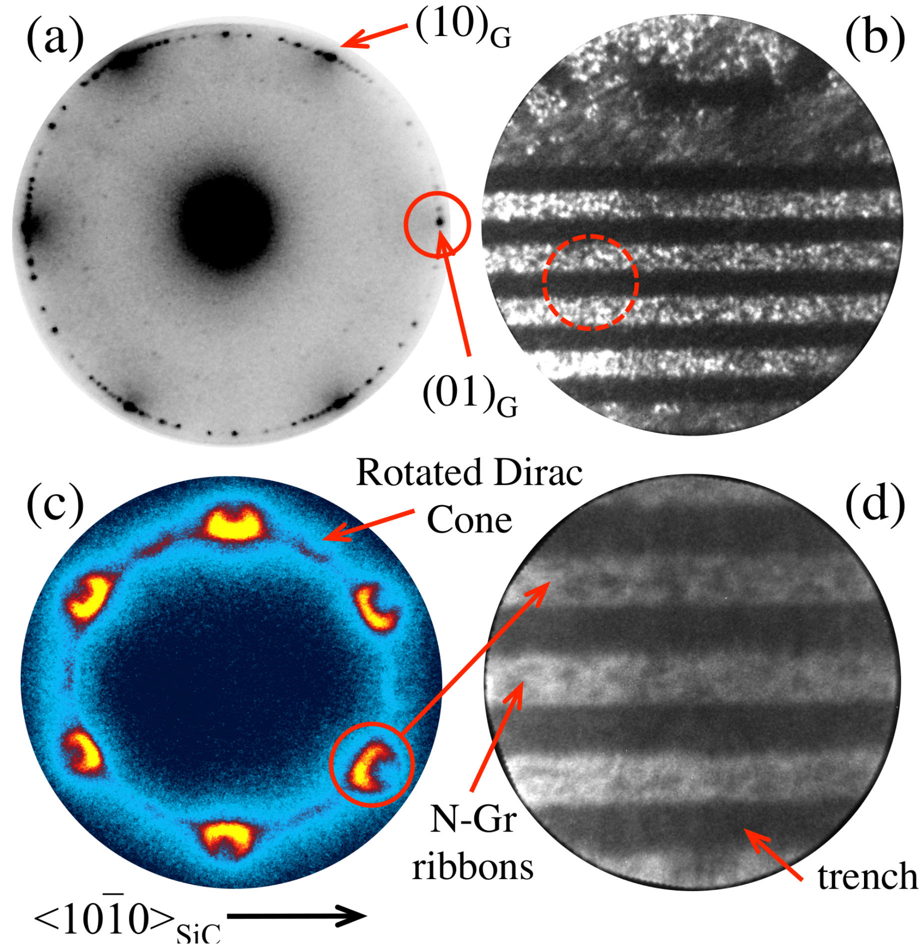

Figure 40: (a) μ-LEED image from the 2D area showing that the primary graphene spots rotated 30° from the SiC $<10\bar{1}0>$ direction. Other rotated domain spots are clearly visible. $E = 40$ eV. (b) DF-LEEM using the graphene $(01)_{\mathrm{G}}$ spot for contrast. $E = 60$ eV. $w = 500$ nm. (c) Constant BE=-1.3 eV cut through the graphene BZ measured by μ-ARPES of a 5-layer N-Gr ribbon area. $\hbar\omega = 36$ eV. The bright Dirac cones are the normal cones from the primary 30° rotated graphene marked in (a). The faint cones are from graphene rotated at other commensurate angles. (d) DF-PEEM (BE=-0.3 eV) of the N-Gr ribbons using the Dirac cone (red circle) in (c) and a 1.5 μm contrast aperture (dashed circle in (b)).

layer or in a rotated graphene sheet below the surface. A DF-PEEM image [122], using the 30° cone for contrast, is shown in Figure 40(d). The ribbons are bright in this image indicating that graphene in the ribbon area is predominately rotated 30°. In contrast, the trenches are dark indicating that most of the graphene in the trench area are rotated in other orientations. The observation that the ribbons and trenches have graphene both with different rotations (as determined by DF-PEEM and DF-LEEM) and different thicknesses (determined by LEEM reflectivity) confirm that the graphene is not continuous between the ribbons and trenches. As the schematic in Figure 38(b) suggests, the graphene in the ribbon area must be isolated from the graphene in the trench area.

4.2.2 Electronic Structure of N-graphene Ribbons

Figures 41(a) and (c) show $E(k)$ cuts through the Dirac cone from the N-Gr ribbons and the un-patterned 2D N-Gr area, respectively. What is clear from Figure 41(a) and (b) is that graphene in the 2D region has Dirac cones with much more intensity within the area bounded by the π-bands compared to the ribbons. This is seen more clearly in both energy distribution curves (EDC) and momentum distribution curves (MDC) through the cones. An EDC through the Dirac point of the ribbons area (see Figure 41(b)) shows a peak in the density of states (DOS) at 0.5 eV below E_F signifying a band gap observed in nitrogen seeded graphene [112]. The DOS peak at the valence band maximum in Figure 41(b) is well defined although broadened by the 0.3 eV instrument resolution. The 2D area DOS in Figure 41(d) shows no peak and a much larger background between the π-bands. It is important to note that a 2 μm field limiting aperture was used in the μ-ARPES. Therefore, in the ribbon area, the spectra are a composite of spectra from both ribbons and trenches. However, within the region selected by the field limiting aperture, the ribbon area was twice that of trenches as marked by the dashed circle in Figure 40(b). The intensity in the

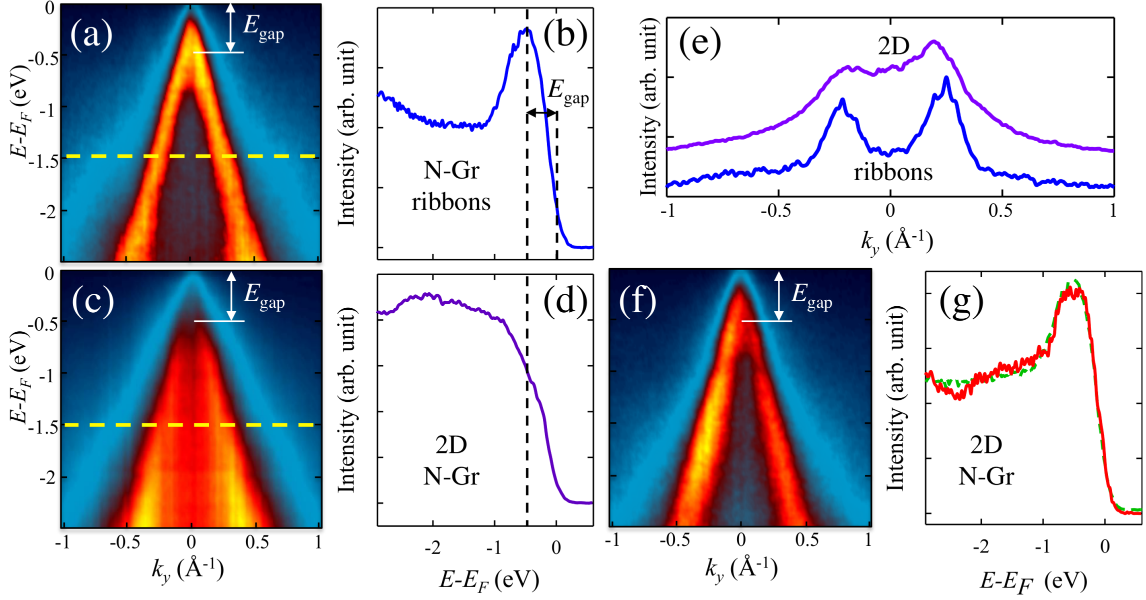

Figure 41: $E(k)$ slices through the Dirac cone (red circle in Figure 40(c)) on (a) N-Gr ribbons and (c) on a representative area of the 2D N-Gr section. k_y is perpendicular to the $\Gamma - K$ direction. (b) and (d) are corresponding EDCs through the Dirac point of the ribbon and 2D area, respectively. The valance band maximum in (b) is marked by the dashed vertical line. (e) MDC's through the Dirac cones in (a) and (c) at $E - E_F = -1.5$ eV (yellow dashed lines in (a) and (c)). (f) $E(k)$ slices through a Dirac cone from a more ordered area of the 2D N-Gr section. (g) An EDC (red) through the Dirac point in (f) at $E - E_F = -1.5$ eV. A composite EDC (green dashed) is shown that is made from the EDC of the ribbon (b) and the EDC from the disordered 2D region in (d).

center of the cone, bounded by the π-bands in Figure 41(a) and (c), is because of both the buckled graphene and the spatial disorder in the film. The N-Gr buckling contribution to the diffuse $E(k_y)$ spectrum is a result of the distribution of local surface normals [112] that cause electrons leaving different areas of the surface, with the same energy, to have different parallel momenta (k_x, k_y). The result is that the analyzer simultaneously measures a wide set of slices through the Dirac cone, i.e., a set of constant k_x conic sections through $E(k_y, k_x)$ for a broad range of different k_x values [123]. Long-range order also influences the measured $E(k_y, k_x)$. Domain size is determined by intrinsic steps in the SiC or by steps caused by thickness variations in the film (i.e., thicker graphene areas have consumed more SiC and are therefore lower in height compared to thinner areas). Rotational boundaries can also be formed as graphene flows over a curved step. These finite size effects lead to a momentum broadening $(\Delta k_x, \Delta k_y)$ of the π-bands. MDC cuts through the cones (see Figure 41(e)) show that the π-bands are narrower in the ribbons compared to the 2D area. The Δk_y width of the 2D area N-Gr is twice as broad as the ribbons (the FWHM of the 2D and ribbons are 0.37 Å^{-1} and 0.17 Å^{-1}, respectively). For comparison, the instrument resolution at this energy is $\Delta k_{\text{inst}} \sim 0.06$ Å^{-1}. The significant reduction in the π-band broadening observed in the ribbons demonstrates that the ribbons geometry improves the long range order of the C-face film.

In addition to the 2D N-Gr spectra represented by Figure 41(c) and (d), other parts of the 2D area have DOS curves similar to the ribbons but with a broader DOS peak (see Figure 41(f)), more intensity between π-bands, and a larger Δk_y broadening. A μ-ARPES spectrum and its corresponding EDC from these “intermediate” areas are shown in Figure 41(f) and (g). Spectra of this type suggest that, within the 2D area, locally ordered areas typical of graphene on the ribbons coexist with more disordered areas characterized by spectra like those shown in Figure 41(c) and (d). We demonstrate this by making a weighted sum of the two spectra in Figure 41(b)

and (d). The resultant composite spectra is shown in Figure 41(g). The best fit is obtained for a ratio of 1:4 between the spectra from the disordered and ordered regions, respectively. Patterning the nitrogen seeded SiC before graphene growth has reduced the disordered N-Gr regions that are prevalent throughout the 2D area. The increased order in these graphene ribbons will allow standard area-averaged ARPES (with better energy resolution) to be used in future studies design to investigate the role of strain in N-Gr's band structure.

In conclusion, we have shown in this section how nitrogen-seeded graphene (N-Gr) is grown from patterned stripes etched in the SiC $(000\bar{1})$ surface. The patterned growth produces a set of parallel nitrogen-seeded SiC stripes (400-500 nm wide). Graphene growth on these patterned surfaces leads to the formation of nitrogen-graphene ribbons with substantially improved structural and electronic properties. The thickness disorder normally observed in C-face graphene is improved by a factor of four so that only monolayer variations are observed across at least $100\mu\mathrm{m}^2$ area. Unfortunately, there is no theoretical guidance to understand the substantially improved thickness uniformity. Proposed growth models based on transmission electron microscopy studies of flat C-face graphene do not seem to apply to the ribbon geometry in this study [124]. We propose that the improved uniformity is a result of controlled heterogeneous edge sites in the patterned ribbons that allow Si to diffuse out of the graphene/SiC interface. The edge sites prevent Si buildup at the SiC-graphene interface that normally causes the formation of vertical tube defects in the C-face SiC films [115], which act as Si vents that locally stimulate rapid graphene growth. In addition to the thickness control, rotational stacking order is also improved with the majority of the ribbon area having N-Gr rotated 30° relative to the SiC $<10\bar{1}0>$ direction. The improved thickness control and long range order of the N-Gr ribbons result in a significant improvement in the uniformity of N-Gr's electronic band structure. The improved order will provide an experimental platform

to investigate details of the band structure of N-Gr films, including how its band gap depends on layer thickness, as well understanding how the large pseudo-magnetic fields, known to exist in these films, depend on strain confinement in sub-100nm ribbons. While this work shows how to control the growth uniformity in N-Gr ribbons, it also suggests that improvements in the film thickness of pristine graphene grown on C-face SiC surface can be made by patterning ribbons. This would offer a way to take advantage of the extremely high mobility in C-face graphene and the thickness uniformity normally only achievable for graphene grown on the SiC Si-face.

CHAPTER V

CONCLUSION

5.1 Summary

To summarize this thesis, our purpose was to modify and characterize both the interface and surface of graphene in order to control the physical and electronic properties of graphene. The graphene samples used in thesis are high-quality epitaxial graphene grown on the carbon face of SiC using the confinement-controlled sublimation method. In Chapter III, the focus was on the interaction between silicon and graphene. Silicon was deposited onto the C-face graphene surface and annealed at different high temperatures from 1000 °C to 1400 °C. The samples were measured by various surface sensitive characterization instruments to show that silicon was able to rapidly intercalate into the graphene-SiC interface at 1000 °C through heterogeneous sites. Interfacial Si started to diffuse back onto the graphene surface and form surface SiC structures at 1100 °C by bonding to carbon atoms of graphene. After annealed to 1300°C, more interfacial Si diffused to the surface to form new reconstruction patterns on surface SiC. Most of Si evaporated from the system by heating to 1400 °C and an ordered and thin SiC film was formed on the graphene surface.

In Chapter IV, we discussed a significant problem of graphene, which is that no significant band gap exists in graphene. We demonstrated a novel approach to opening a $\sim$ 0.7 eV band gap in graphene by growing it from a nitrogen-seeded SiC surface. Rather than forming defects in the graphene lattice, nitrogen atoms bound graphene to the SiC interface to form a 1-2nm high ripple structure in graphene films. The origin for the gap was speculated to be either quasi-periodic strain or electron localization in the 1-2nm buckled ribbons. In order to improve the structure of this new form of

graphene, nitrogen-seeded SiC samples were patterned prior to graphene growth. The pre-pattern method led to significant improvements in thickness uniformity, rotational ordering, and the gapped band structure. We claimed that the improved structure was a result of controlled heterogeneous edge sites that allowed Si to diffuse out. This method should also apply to normal C-face epitaxial graphene growth.

5.2 Future Outlook

One way in which this thesis work can be extended is by carrying out normal ARPES measurements on the patterned N-graphene using a narrower ribbon width. Some initial work has been done in this direction, but it was not shown in this thesis. Preliminary results show an even better gapped band structure. Complete surface characterization imaging methods such as LEEM and XPEEM would also be required on samples with narrower ribbons to fully understand the preliminary results. Another future direction is to directly measure the total band gap of N-Gr. Since ARPES is able to measure only the band structure below the Fermi level, the band gap from ARPES results are only the lower limit of the total band gap. Optical methods such as infrared spectroscopy can be applied to measure the total band gap. Finally, it will be also beneficial to measure transport properties of the N-Gr by patterning the Hall bar and test the on-off ratio by fabricating transistors based on the N-Gr. As a result of the high mobility and the band gap, N-graphene could be a promising candidate for future electronics.

APPENDIX A

NITROGEN SITE ASSIGNMENTS

After graphene growth the N 1s line resolves into two lines denoted as N_S and N_P as shown in the insert in Figure 31(d). Identification of the binding configuration and atomic site of these lines is based on a large number of studies of bulk N-doped SiC and, more recently, surface/interface assignments.

As early as 1961 Electron Spin Resonance studies [104] indicated that nitrogen occupies the carbon site in bulk SiC. That is, the N is bound to four Si nearest neighbors and is an n-type dopant. Numerous XPS studies of Si_3N_4 have reported N binding energy values in the 397-398.7 range. A typical example is the work of Chourasia and Chopra [105] who report a value of 397.8 eV for CVD grown Si_3N_4 films. In a very extensive study of the SiO_2/N/SiC (Si-face) interface, Tochihhara and Shirasawa report a N 1s line position of 398.7 eV (and a C 1s binding energy for C in SiC of 283.9 eV) [89]. This model includes N bound to Si atoms at a surface C site where the Si-N bond length with N at a carbon site was determined to be very close to the bond length in Si_3N_4. The model in Ref. [89] was supported by a large variety of data including quantitative low-energy electron diffraction, scanning tunneling microscopy, Auger electron spectroscopy, surface X-ray diffraction, and first principle calculations. Additional recent reports by Kosugi et al [106]. using the same NO process described in this current work report a N 1s binding energy of 398.2 eV and note that the N is resistant to HF etching. Similar results, particularly addressing the role of surface deposited N as a dopant are reported by Liu et al [125].

To calibrate these earlier studies with the work reported here, we use the binding energy difference between the N 1s and C 1s in SiC, $\Delta E_{\text{N-C}}$. This is found to be

$\Delta E_{\text{N-C}} = 115.0 \pm 0.2$ eV in all cases, exactly what is measured in the studies reported here for the N_S state of Fig. 1d of the main text. In short we assign the N_S state to N at a C site, bonded to 3 or 4 Si atoms at the SiC interface.

To identify the N_P site, we have look at previous work on N-C bonds. There are relatively few studies of C_3N_4 [107] but in the cases reported, the energy difference $\Delta E_{\text{N-C}} \sim 133.7 \pm 0.2$ eV (where the carbon reference is to C in C_3N_4). In this work the experimental $\Delta E_{\text{N-C}}$ for the N_P site is 133.3 eV. This strongly suggests that the N_P site is nitrogen bonded to 3 carbon atoms. We therefore suggest a model where $\sim 1.8 \times 10^{14}/\text{cm}^2$ N_S atoms are substituted in the C plane of the interface layer of SiC and $\sim 0.4 \times 10^{14}/\text{cm}^2$ N_P atoms are bonded to carbon providing the attachment between graphene and SiC.

There is no observable C-N bond peak in the C1 spectrum see either Figure 31(e) or Figure 30. There are two reason for this. First, N inclusions in the graphene would have two peaks shifted 1.1 and 2.2 eV to higher BE relative to the graphene C 1s peak. These peaks are not observed even in the more surface sensitive photon energy spectra supporting the major statement of the paper that N is not incorporated in the graphene. The 900 eV photon energy spectrum in Figure 31(e) does show a broadening with a tail at higher BE. This tail is because of the different charge state of layers deeper in the film [88]. The second reason that we do not expect to see a C-N bond is that these bonds occur at a very low density at the SiC interface. As discussed above, most of the nitrogen is bonded to Si atoms in SiC not to carbon atoms. The N-C interface bond estimate of $\sim 0.4 \times 10^{14}/\text{cm}^2$ corresponds to 0.05ML. The small fraction of N-C bonds at the interface would be essentially undetectable with XPS under normal circumstances. Because, as Figure 31(e) clearly shows, even the SiC-C 1s peak is severely attenuated and given the high energy tail in the C-C peak, the N-C peak cannot be detected.

APPENDIX B

Q-DEPENDENT BROADENING ANALYSIS

To analyze the strain causing the q-dependent broadening shown in Figure 37 we use a 1D model where the position of the nth atom is due to the accumulated distortion from the local stain, Δa_j, of all preceding atoms in the chain. The position of the nth atom is then $R_n = na + \sum_{j=0}^{n} \Delta a_j$ where the last term is the accumulated stain in the chain. If we assume that the Δa_j's are uncorrelated with the atom position a_n (a reasonable assumption considering the lattice mismatch of graphite and SiC), then the diffracted amplitude from a graphene becomes;

$$A(q_\parallel) \propto \sum_{n=0}^{N-1} e^{iq_\parallel na} \left\langle e^{iq_\parallel \sum_{j=0}^{n} \Delta a_j} \right\rangle . \tag{16}$$

Where N is the number of coherent cells ($L = Na$). The diffracted intensity from this model is derived in the Appendix assuming that the Δa_j's are independent. The result is a diffraction line shape that has a Gaussian peak related to the strain plus a Lorentzian peak related to the graphene domain size (see Equation (19a)).

Starting from Equation (16) for the 1D strain model and assuming that the local strain Δa_j's are independent (i.e, $< \Delta a_j > = < \Delta a_j \Delta a_k > = 0$ and $< \Delta a_j^2 > = < \Delta a^2 >$ is a constant), to a good approximation the average term in Equation (16) can be written as;

$$\left\langle e^{iq_\parallel \sum_{j=0}^{n} \Delta a_j} \right\rangle \simeq e^{-nq_\parallel^2 < \Delta a^2 > /2}. \tag{17}$$

Substituting Equation 17 into Equation 16 gives the diffracted intensity, $I = AA^*$ to be;

$$I(q_\parallel) \propto \frac{(1-f^N)^2 + 4f^N \sin^2(q_\parallel aN/2)}{(1-f)^2 + 4f\sin^2(q_\parallel a/2)}, \tag{18a}$$

$$f = e^{-2\beta_s/(N\beta_L)}, \tag{18b}$$

$$\beta_s = q_\parallel^2 \epsilon_s^2 \pi L/2 \text{ and } \beta_L = 2\pi/L. \tag{18c}$$

Where $\epsilon_s^2 =< \Delta L >^2 /L^2 = N < \Delta a^2 > /L^2$ is the mean square strain in the film. Note that the argument of f in Equation (18b) is $(q_\parallel a \epsilon_s \sqrt{N})^2$. For reasonable values of the strain, i.e., $\epsilon_s < 0.05\%$, $f \sim 1$ for momentum transfer vectors up to $q_\parallel \leq 4\pi/a$ and $N \sim 10^4$. This suggests that the intensity in Equation (18a) can to a good approximation be written as;

$$I(\Delta q) \simeq A\left[\frac{\eta}{1+\pi^2\Delta q^2/\beta_s^2} + (1-\eta)e^{-\Delta q^2\pi/\beta_L^2}\right] \tag{19a}$$

$$\eta(\beta_s/\beta_L) = \frac{(1-e^{-2\beta_s/\beta_L})^2}{(1-e^{-2\beta_s/\beta_L})^2 + 4\frac{\beta_s^2}{\beta_L^2}e^{-2\beta_s/\beta_L}} \tag{19b}$$

$$\beta_s = Q_n^2 \epsilon_s^2 \pi L/2 \tag{19c}$$

Where $\Delta q = Q_n - q_\parallel$ is the momentum transfer relative to the graphite rod $Q_n = 2\pi n/a$, n=integer. Note we have used the approximation, $\frac{\sin^2 Nx}{\sin^2 x} \sim \exp[-N^2x^2/\pi]$ [131]. Similar to other methods used to determine strain in powder diffraction [132], we can define the integral breadth of the peak;

$$\beta(q) \equiv \frac{\int I dq}{I_{max}} = \eta\beta_s + (1-\eta)\beta_L \tag{20}$$

Since β_s is a function of Q_n while β_L is not, measurements of $\beta(q)$ for two different values of Q_n allows us to separate out the finite size broadening L from the strain broadening ϵ_s.

Surface/Interface Modification and Characterization of C-face Epitaxial Graphene

Feng Wang

96 Pages

Directed by Professor Edward H. Conrad

Graphene has been one of the most interesting and widely investigated materials in the past decade. Because of its high mobility, high current density, inherent strength, high temperature stability and other properties, scientists consider it a promising material candidate for the future all-carbon electronics. However, graphene still exhibits a number of problems such as an unknown interface structure and no sizable band gap. Therefore, the purpose of this thesis is to probe and solve these problems to make graphene suitable for electronics. The work focuses on high-quality C-face epitaxial graphene, which is grown on the $(000\bar{1})$ face (C-face) of hexagonal silicon carbide (SiC) using the confinement-controlled sublimation (CCS) method. C-face epitaxial graphene has much higher mobility compared to Si-face graphene, resulting from its special stacking order and interface structure, the latter of which is not fully understood. Thus, the first part of the work consists of a project, which is to investigate and modify the interface and the surface of C-face graphene by silicon deposition and annealing. Results of this project show that silicon can intercalate into the graphene-SiC interface and form SiC by bonding carbon atoms on the graphene surface. Another crucial problem of graphene is the absence of a band gap, which prevents graphene from becoming an ideal candidate for traditional digital logic devices. Therefore, the second project of this work is devoted to introducing a wide band gap into the graphene electronic structure by growing from a nitrogen-seeded SiC. After successful opening of a band gap, a pre-patterning method is applied to improve graphene thickness variations, orientational epitaxy, and the gapped electronic structure.

REFERENCES

[1] C. Berger, Z. Song, T. Li, X. Li, A.Y. Ogbazghi, R. Feng, Z. Dai, A.N. Marchenkov, E.H. Conrad, P.N. First, W.A. de Heer, *J. Phys. Chem B* **108** 19912 (2004)

[2] K.S. Novoselov, A.K. Geim, S.V. Morozov, D. Jiang, Y. Zhang, S.V. Dubonos, I.V. Grigorieva, A.A. Firsov, *Science* **306** 666 (2004)

[3] K.S. Novoselov, D. Jiang, F. Schedin, T.J. Booth, V.V. Khotkevich, S.V. Morozov, A.K. Geim, *Proc. Nat. Acad. Sci.* **102**, 10451 (2005).

[4] C. Berger, Z. Song, X. Li, X. Wu, N. Brown, C. Naud, D. Mayou, T. Li, J. Hass, A.N. Marchenkov, E.H. Conrad, P.N. First, W.A. de Heer, *Science* **312** 1191 (2006)

[5] A.K. Geim, K.S. Novoselov, *Nature Mat.* **6**, 183 (2007)

[6] A.K. Geim, *Science* **324** 1530 (2009)

[7] P.R. Wallace, *Phys. Rev.* **71** 622 (1947)

[8] T. Ando, T. Nakanishi, R. Saito, *J. Phys. Soc. Jpn* **67** 2857 (1998)

[9] S. Stankovich, D.A. Dikin, G.H.B. Dommett, K.M. Kohlhaas, E.J. Zimney, E.A. Stach, R.D. Piner, S.T. Nguyen, R.S. Ruoff, *Nature* **442**, 282 (2006)

[10] X. Li, W. Cai, J. An, S. Kim, J. Nah, D. Yang, R. Piner, A. Velamankanni, I. Jung, E. Tutuc, S. K. Banerjee, L. Colombo, R. S. Ruoff, *Science* **5**, 1312 (2009)

[11] A. Reina, X. Jia, J. Ho, D. Nezich, H. Son, V. Bulovic, M. S. Dresselhaus, J. Kong, *Nano Lett.* **9**, 30 (2009)

[12] P.W. Sutter, J.-I. Flege, E.A. Sutter, *Nature Mat.* **7**, 406 (2008)

[13] N. Alem, R. Erni, C. Kisielowski, M.D. Rossell, W. Gannett, A. Zettl. *Phys. Rev.* **B 80**, 155425 (2009).

[14] B. Radisavljevic, A. Radenovic, J. Brivio, V. Giacometti, A. Kis, *Nature Nanotech.* 6, 147 (2011)

[15] K.R. Knox, S. Wang, A. Morgante, D. Cvetko, A. Locatelli, T.O. Mentes, M.A. Nino, P. Kim, R.M. Osgood, arXiv:0806.0355 (2008)

[16] V. Geringer, M. Liebmann, T. Echtermeyer, S. Runte, M. Schmidt, R. Ruckamp, M.C. Lemme, M. Morgenstern, *Phys. Rev. Lett.* **102**, 076102 (2009).

[17] A. van Bommel, J. Crombeen, A. van Tooren, *Surf. Sci.* **48**, 463 (1975).

[18] W.A. de Heer, http://hdl.handle.net/1853/31270 (2009)

[19] S.Y. Zhou, G.-H. Gweon, J.Graf, A.V. Fedorov, C.D. Spataru, R.D. Diehl, Y. Kopelevich, D.-H. Lee, S.G. Louie, A. Lanzara, *Nature Phys.* **2**, 595 (2006).

[20] A. Bostwick, T. Ohta, T. Seyller, K. Horn, E. Rotenberg, *Nature Phys.* **3**, 36 (2007).

[21] S. Stankovich, D.A. Dikin, R.D. Piner, K.A. Kohlhaas, A. Kleinhammes, Y. Jia, Y. Wu, S.T. Nguyen, R.S. Ruoff, *Carbon* **45**, 1558 (2007).

[22] D. Li, R.B. Kaner, *Science* **320**, 1170 (2008)

[23] W.S. Hummers, R.E. Offeman, *J. Am. Chem. Soc.* **80**, 1339 (1958)

[24] H.C. Schniepp, J.-L. Li, M.J. McAllister, H. Sai, M. Herrera-Alonso, D.H. Adamson, R.K. Prud'homme, R. Car, D.A. Saville, I.A. Aksay, *J. Phys. Chem. B* **110**, 8535 (2006)

[25] W. Gao, L.B. Alemany, L. Ci, P.M. Ajayan. *Nature Chem.* **1**, 403 (2009)

[26] Q. Yu, J. Lian, S. Siriponglert, H. Li, Y.P. Chen, S. Pei, *Appl. Phys. Lett.* **93**, 113103 (2008)

[27] Y. Zhang, L. Zhang, C. Zhou, *Acc. Chem. Res.* **46**, 2329 (2013)

[28] P.Y. Huang, C.S. Ruiz-Vargas, A.M. van der Zande, W.S. Whitney, M.P. Levendorf, J.W. Kevek, S. Garg, J.S. Alden, C.J. Hustedt, Y. Zhu, J. Park, P.L. McEuen, D.A. Muller, *Nature* **469**, 389 (2011)

[29] M. Orlita, C. Faugeras, P. Plochocka, P. Neugebauer, G. Martinez, D. K. Maude, A.-L. Barra, M. Sprinkle, C. Berger, W. A. de Heer, M. Potemski, *Phys. Rev. Lett.* **101**, 267601 (2008)

[30] X. Wu, Y. Hu, M. Ruan, N.K. Madiomanana, J. Hankinson, M. Sprinkle, C. Berger, W.A. de Heer, *Appl. Phys. Lett.* **95**, 223108 (2009)

[31] Y.J. Song, A.F. Otte, Y. Kuk, Y. Hu, D.B. Torrance, P.N. First, W.A. de Heer, H. Min, S. Adam, M.D. Stiles, A.H. MacDonald, J.A. Stroscio, *Nature* **467**, 185 (2010)

[32] M. Sprinkle, M. Ruan, Y. Hu, J. Hankinson, M. Rubio-Roy, B. Zhang, X. Wu, C. Berger, W. A. de Heer, *Nature Nanotech.* **5**, 727 (2010)

[33] T. Ohta, A. Bostwick, T. Seyller, K. Horn, E. Rotenberg, *Science* **18**, 951 (2006)

[34] A. Mattausch, O. Pankratov,*Phys. Rev. Lett.***99**, 076802 (2007)

[35] M.S. Nevius, M. Conrad, F. Wang, A. Celis, M.N. Nair, A. Taleb-Ibrahimi, A. Tejeda, E.H. Conrad, paper in preparation

[36] T. Ohta, A. Bostwick, J.L. McChesney, T. Seyller, K. Horn, E. Rotenberg, *Phys. Rev. Lett.* **98**, 206802 (2007)

[37] J. Hicks, M. Sprinkle, K. Shepperd, F. Wang, A. Tejeda, A. Taleb-Ibrahimi, F. Bertran, P. Le Fevre, W.A. de Heer, C. Berger, E.H. Conrad, *Phys. Rev.* **B 83**, 205403 (2011)

[38] C. Mathieu, E.H. Conrad, F. Wang, J.E. Rault, V. Feyer, C.M. Schneider, O. Renault, N. Barrett, *Surf. Interface Anal.* **46**, 1268 (2014)

[39] V. Ramachandran, M.F. Brady, A.R. Smith, R.M. Feenstra, D.W. Greve, *J. of Electronic Mat.* **27**, 308 (1998)

[40] W.A. de Heer, C. Berger, X. Wu, P.N. First, E.H. Conrad, X. Li, T. Li, M. Sprinkle, J. Hass, M.L. Sadowski, M. Potemski, G. Martinez, *Sol. State Comm.* **143**, 92 (2007).

[41] F. Speck, M. Ostler, J. Röhrl, J. Jobst, D. Waldmann, M. Hundhausen, L. Ley, H.B. Weber, T. Seyller, *Mat. Sci. Forum*, **645-648**, 629 (2010).

[42] J. Hass, W.A. de Heer and E.H. Conrad, *J. Phys.: Condens. Matt.* **20**, 323202 (2008).

[43] Riedl, C., Starke, U., Bernhardt, J., Franke, M., Heinz, K., *Phys. Rev.* **B 76**, 245406 (2007).

[44] J. Hass, R. Feng, J. E. Milln-Otoya, X. Li, M. Sprinkle, P. N. First, W. A. de Heer, E. H. Conrad, C. Berger, *Phys. Rev.* **B 75**, 214109 (2007).

[45] J. Hass, J. E. Milln-Otoya, P. N. First, E. H. Conrad, *Phys. Rev.* **B 78**, 205424 (2008).

[46] Konstantin V. Emtsev, Alexei A. Zakharov, Camilla Coletti, Stiven Forti, Ulrich Starke, *Phys. Rev.* **B 84**, 125423 (2011).

[47] C. Riedl, C. Coletti, T. Iwasaki, A. A. Zakharov, U. Starke, *Phys. Rev. Lett.* **103**, 246804 (2009).

[48] C. Virojanadara, S. Watcharinyanon, A. A. Zakharov, L. I. Johansson, *Phys. Rev.* **B 82**, 205402 (2010).

[49] R. E. Honig, *RCA Rev.* **23**, 567 (1962)

[50] R. E. Honig, D. A. Kramer, *RCA Rev.* **30**, 28 (1969).

[51] J. Hass, F. Varchon, J.E. Millan-Otoya, M. Sprinkle, N. Sharma, W. A. de Heer, C. Berger, P. N. First, L. Magaud and E.H. Conrad, *Phys. Rev. Lett.* **100**, 125504 (2008).

[52] N. Sieber, Th. Seyller, L. Ley, D. James, J.D. Riley, R.C.G. Leckey, and M. Polcik, *Phys. Rev.* **B 67**, 205304 (2003).

[53] M. Sprinkle, J. Hicks, A. Tejeda, A. Taleb-Ibrahimi, P. Le Fèvre, F. Bertran, H. Tinkey, M.C. Clark, P. Soukiassian, D. Martinotti, Hass and E.H. Conrad, *J. of Phys D* **43**, 374006 (2010).

[54] D.L. Miller, K.D. Kubista, G.M. Rutter, M. Ruan, W.A. de Heer, M. Kindermann, P.N. First and J.A. Stroscio, *Nature Phys.* **6**, 811 (2010).

[55] D.L. Miller, K.D. Kubista, G.M. Rutter, M. Ruan, W.A. de Heer, P.N. First and J.A. Stroscio., *Science*, **324** 924 (2009).

[56] G.M. Rutter, N.P. Guisinger, J.N. Crain, E.A.A. Jarvis, M.D. Stiles, T. Li, P.N. First, and J.A. Stroscio2, *Phys. Rev.* **B 76**, 235416-1(2007).

[57] F.J. Himpsel, F.R. McFeely, A. Taleb-Ibrahimi, J.A. Yarmoff, and G. Hollinger, *Phys. Rev.* **B 38**, 6084 (1979).

[58] G. Mende, J. Finster, D. Flamm, D. Schulze, *Surface Science* **128** 169 (1983).

[59] F. Varchon, P. Mallet, L. Magaud, J. Veuillen, *Phys. Rev.* **B 77**, 165415 (2007).

[60] M. Naitoh,M. Kitada, S. Nishigaki, N. Toyama, F. Shoji, *Surface Review and Letter* **10** 473-477 (2003)

[61] U. Starke, C. Reidl, *J. of Phys.: Condens. Matter* **21** 134016 (2009)

[62] K.V. Emtsev, F. Speck, T. Seyller, L. Ley, and J. D. Riley, *Phys. Rev.* **B 77**, 155303 (2008).

[63] T. Seyller, K. Emtsev, F. Speck, K.-Y. Gao, L. Ley, *Mater. Sci. Forum* **556-557** 701 (2007).

[64] L. Kubler, K. Aït-Mansour, M. Diani, D. Dentel, J.-L. Bischoff, and M. Derivaz, *Phys. Rev.* **B 72**, 115319 (2005).

[65] I. Gierz, C. Riedl, U. Starke, C.R. Ast, and Klaus Kern, *Nano Lett.* **8**, 4603 (2008).

[66] C. Coletti, C. Riedl, D-S. Lee, B. Krauss, K. von Klitzing, J. Smet and U. Starke, *Phys. Rev.* **B 81**, 235401 (2010).

[67] E. Velez-Fort, C. Mathieu, E. Pallecchi, M. Pigneur, M. G. Silly, R. Belkhou, M. Marangolo, A. Shukla, F. Sirotti, and A. Ouerghi, *ACS Nano* **6**, 10893 (2012).

[68] D. Usachov, O. Vilkov, A. Gr´uneis, D. Haberer, A. Fedorov, V. K. Adamchuk, A. B. Preobrajenski, P. Dudin, A. Barinov, M. Oehzelt, C. Laubschat, and D. V. Vyalikh, *Nano Lett.* **11**, 5401 (2011).

[69] H. Wang, T. Maiyalagan, and X. Wang, *ACS Catal.* **2**, 781 (2012).

[70] M.Y. Han, J.C. Brant, and P. Kim, *Phys. Rev. Lett.* **104**, 056801 1-4 (2010).

[71] L. Jiao, L. Zhang, X. Wang, G. Diankov, and H. Dai, *Nature* **458**, 877-880 (2009).

[72] L. Jiao, X. Wang, G. Diankov, H. Wang, and H. Dai, *Nature Nanotech.* **5**, 321-325 (2010).

[73] J. B. Oostinga, B. Sacépè, M. F. Craciun, and A. F. Morpurgo, *Phys. Rev.* **B 81**, 193408 1-4 (2010).

[74] J. Hicks, A. Tejeda, A. Taleb-Ibrahimi, M.S. Nevius, F. Wang, K. Shepperd, J. Palmer, F. Bertran, P. Le Fèvre, J. Kunc, W.A. de Heer, C. Berger, and E.H. Conrad, it Nature Phys. **9**, 49 (2013).

[75] J. Baringhaus, C. Tegenkamp, F. Edler, M. Ruan, E. Conrad, C. Berger, W.A. de Heer, *Nature* **506**, 349 (2014)

[76] S. Niyogi, E. Bekyarova, M.E. Itkis, H. Zhang, K. Shepperd, J. Hicks, M. Sprinkle, C. Berger, C. N. Lau, W.A. deHeer, E.H. Conrad, and R.C. Haddon, *Nano Lett.* **10**, 4061 (2010).

[77] R. Balog, B. Jørgensen, L. Nilsson, M. Andersen, E. Rienks, M. Bianchi, M. Fanetti, E. Lægsgaard, A. Baraldi, S. Lizzit, Z. Sljivancanin, F. Besenbacher, B. Hammer, T.G. Pedersen, P. Hofmann and L. Hornekær, N̂ature Mat. **9**, 315 (2010).

[78] M. Deifallah, P.F. McMillan, F. Cora, *J. Phys. Chem. C* **112**, 5447 (2008).

[79] F. Joucken, Y. Tison, J. Lagoute, J. Dumont, D. Cabosart, B. Zheng, V. Repain, C. Chacon, Y. Girard, A. R. Botello-Méndez, S. Rousset, R. Sporken, J-C. Charlier, and L. Henrard, *Phys. Rev.* **B 85**, 161408(R) (2012).

[80] A. Lherbier, X. Blase, Y.M. Niquet, F. Triozon, S. Roche, *Phys. Rev. Lett.* **101**, 036808 (2008).

[81] G. Liu, A.C. Ahyi, Y. Xu, T. Isaacs-Smith, Y.K. Sharma, J.R. Williams, L.C. Felman, and S. Dhar, *IEEE Elec. Device Lett.* **34**, 181 (2013).

[82] T. Low, F. Guinea, and M. I. Katsnelson, *Phys. Rev.* **B 83**, 195436 (2011).

[83] K. Wakabayashi, K.-ichi Sasaki, T. Nakanishi, and T. Enoki, *Sci. Technol. Adv. Mater.* **11**, 054504-054521 (2010).

[84] A. Snis and S.F.Matar, *Phys.Rev.* **B 60**,10855 (1999).

[85] A. Avila, I. Montero, L. Galán, J. M. Ripalda, and R. Levy, *J. Appl. Phys.* **89** , 212 (2001).

[86] W.A. de Heer, C. Berger, M. Ruan, M. Sprinkle, X. Li, Y. Hu, B. Zhang, J. Hankinson, and E.H. Conrad, *Proc. Nat. Acad. Sci.* **108**, 16900 (2011).

[87] T. Seyller, K. Emtsev, F. Speck, K.-Y. Gao, and L. Ley, *Mater. Sci. Forum* **556-557**, 701 (2007).

[88] K.V. Emtsev, F. Speck, Th. Seyller, L. Ley, and J. D. Riley, *Phys. Rev.* **B 77**, 155303 (2008).

[89] H. Tochihara and T. Shirasawa, *Prog. in Surf. Sci.* bf 86, 295 (2011).

[90] I. Shimoyama, G. Wu, T. Sekiguchi, and Y. Baba, *Phys. Rev.* **B 62**, R6053 (2000).

[91] C. Ronning, H. Feldermann, R. Merk, H. Hofsass, P. Reinke, and J.U. Thiele, *Phys. Rev.* **B 58**, 2207 (1998).

[92] J. Hicks, K. Shepperd, F. Wang and E. H. Conrad, *J. Phys. D: Appl. Phys.* **45**, 154002 (2012).

[93] M. Sprinkle, D. Siegel, Y. Hu, J. Hicks, A. Tejeda, A. Taleb-Ibrahimi, P. Le Fèvre, F. Bertran, S. Vizzini, H. Enriquez, S. Chiang, P. Soukiassian, C. Berger, W.A. de Heer, A. Lanzara, E.H. Conrad, *Phys. Rev. Lett.* **103**, 226803 (2009).

[94] C. Park, F. Giustino, C. Spataru, M. Cohen, and S. Louie, *Nano Lett.* **9**, 4234 (2009).

[95] K. R. Knox, A. Locatelli, M. B. Yilmaz, D. Cvetko, T. Onur Mentes, M. À. Niño, P. Kim, A. Morgante, and R. M. Osgood Jr., *Phys. Rev.* **B 84**, 115401 (2011).

[96] L. Zhao, R. He, K.T. Rim, T. Schiros, K.S. Kim, H. Zhou, C. Gutièrez, S.P. Chockalingam, C.J. Arguello, L. Páová D. Nordlund, M.S. Hybertsen, D.R. Reichman, T.F. Heinz, P. Kim, A. Pinczuk, G.W. Flynn, and A.N. Pasupathy, *Science* **333**, 999 (2011).

[97] J. Hass, W.A. de Heer and E.H. Conrad, *J. Phys.: Condens. Matt.* **20**, 323202 (2008).

[98] C. Riedl, U. Starke, J. Bernhardt, M. Franke, and K. Heinz, *Phys. Rev.* **B 76**, 245406 (2007).

[99] Y.-W. Son, M.L. Cohen, and S.G. Louie, *Phys. Rev. Lett.* **97**, 216803 1-5 (2006).

[100] V.M. Pereira, A. H. Castro Neto, H.Y. Liang, and L. Mahadevan, *Phys. Rev. Lett.* **105**, 156603 (2010).

[101] N. Levy, S. A. Burke, K. L. Meaker, M. Panlasigui, A. Zettl, F. Guinea, A. H. Castro Neto, and M. F. Crommie, *Science* **329**, 544 (2010).

[102] D. Wei, Y. Liu, Y. Wang, H. Zhang, L. Huang, and G. Yu, *Nano Lett.* **9**, 1752 (2009).

[103] Z. Jin, J. Yao, C. Kittrell, and J.M. Tour, *ACS Nano* **5**, 4112 (2011).

[104] H.H. Woodbury and G W Ludwig, *Phys. Rev.* **124**, 1083 (1961).

[105] A R Chourasia and D R Chopra, *Surf. Sci. Spectra* **2**, 117 (1994)

[106] R.Kosugi, T. Umeda and Y. Sakuma, *Appl. Phys. Lett.* **99**, 182111, (2011)

[107] C. Ronning, H. Feldermann, R. Merk, and H. Hofsass, *Phys. Rev.* **B 58**, 2207 (1998).

[108] F. Tuinstra, J.L. Koenig, *J. Chem. Phys.* **53**, 1126 (1970).

[109] L.G. Cançado, K. Takai, T. Enoki, M. Endo, Y.A Kim, H. Mizusaki, A. Jorio, L.N. Coelho, R. Magalhães-Paniago, M.A. Pimenta, *Appl. Phys. Lett.* **88**, 163106 (2006).

[110] Y. Hu, PhD Thesis, Georgia Institute of Technology (2013). http://hdl.handle.net/1853/48705

[111] Z. Guo, R. Dong, P.S. Chakraborty, N. Lourenco, J. Palmer, Y. Hu, M. Ruan, J. Hankinson, J. Kunc, J.D. Cressler, C. Berger, W.A. de Heer, *Nano Lett.* **13**, 942 (2013).

[112] F. Wang, G. Liu, S. Rothwell, M. Nevius, A. Tejeda, A. Taleb-Ibrahimi, L.C. Feldman, P.I. Cohen, and E. H. Conrad, *Nano Lett.* **13**, 4827 (2013).

[113] T. Low and F. Guinea, *Nano Lett.* **10**, 3551 (2010).

[114] T. Low, F. Guinea, and M. I. Katsnelson, *Phys. Rev.* **B 83**, 195436 (2011).

[115] J. Hicks, K. Shepperd, F. Wang and E. H. Conrad, *J. Phys. D: Appl. Phys.* **45**, 154002 (2012).

[116] W.A. de Heer, C. Berger, M. Ruan, M. Sprinkle, X. Li, Y. Hu, B. Zhang, J. Hankinson, and E.H. Conrad, *Proc. Nat. Acad. Sci.* **108**, 16900 (2011).

[117] J.-S. Moon, D. Curtis, M. Hu, D. Wong, P.M. Campbell, G. Jernigan, J. Tedesco, B. VanMil, R. Myers-Ward, C. Eddy, D.K. Gaskill, J. Robinson, M. Fanton, and P. Asbeck, *Topical Meeting on Silicon Monolithic Integrated Circuits in RF Systems (SiRF)* **1**, 11-13 (2010).

[118] F. Wang, K. Shepperd, J. Hicks, M.S. Nevius, H. Tinkey, A. Tejeda, and E.H. Conrad, *Phys. Rev.* **B 85**, 165449(6) (2012).

[119] H. Hibino, H. Kageshima, F. Maeda, M. Nagase, Y. Kobayashi, and H. Yamaguchi, *Phys. Rev.* **B 77**, 075413(7) (2008).

[120] M.S. Nevius, F. Wang, C. Mathieu, N. Barrett, A. Sala, T. O. Menteş, A. Locatelli, and E.H. Conrad, *Nano Lett.* **14**, 6080 (2014).

[121] M. Kusunoki, T. Suzuki, K. Kaneko, and M. Ito, *Phil. Mag.Lett.* **79**, 153 (1999).

[122] T. O. Menteş, and A. Locatelli, it J. Electron Spectrosc. Relat. Phenom. **185**, 32317329 (2012).

[123] K.R. Knox, S. Wang, A. Morgante, D. Cvetko, A. Locatelli, T.O. Menteş, M.A. Niño, P. Kim, and R.M. Osgood, Jr, *Phys. Rev.* **B 78**, 201408(R) (2008).

[124] W. Norimatsu and M. Kusunoki, *Semicond. Sci. Technol.* **29**, 064009 (2014).

[125] G. Liu, A.C. Ahyi, Y. Xu, T. Isaacs-Smith, Y.K. Sharma, J.R. Williams, L.C. Felman, and S. Dhar, *IEEE Elec. Device Lett.* **34**, 181 (2013).

[126] J.-J. Yeh and I. Lindau, *Atomic Data Nucl. Data Tables* **32**, 1 (1985).

[127] J.-J. Yeh, Atomic Calculations of Photoionization Cross Sections and Asymmetry Parameters, (Gordon and Breach, Langhorne, PA, 1993).

[128] A. Locatelli, L. Aballe, T.O. Menteş, M. Kiskinova, E. Bauer, *Surf. Interface Anal.* **38**, 1554171557 (2006).

[129] E. Bauer, *Rep. Prog. Phys.* **57**, 895 (1994).

[130] T. Schmidt, S. Heun, J. Slezak, J. Diaz, K.C. Prince, G. Lilienkamp, E. Bauer, *Surf. Rev. Lett.* **5**, 1287171296 (1998).

[131] B.E. Warren, *X-ray Diffraction*, (Addison-Wesley Publishing Co. 1969).

[132] D. Balzar, in *Defect and Microstructure Analysis from Diffraction*, ed. R.L. Snyder, H.J. Bunge, and J. Fiala, International Union of Crystallography Monographs on Crystallography No. 10 (Oxford University Press, New York, 1999) pp. 94-126.